Effect of localization error on the performance of location-aided beam-management in 5G and beyond

Enrico Tosi

Master Thesis

October 12, 2023

Examiners

Prof.Federico Chiariotti
Prof. Marco Giordani

Supervisors

Prof.Federico Chiariotti
Dr Ljiljana Simić, Aron Schott M.Sc.

ICT for internet and multimedia
Universitá degli Studi di Padova

The present work was submitted to the Institute for Universitá degli Studi di Padova

Effect of localization error on the performance of location-aided beam-management in 5G and beyond

Master Thesis

presented by
Enrico Tosi

Prof.Federico Chiariotti
Prof. Marco Giordani

Aachen, October 12, 2023

(Enrico Tosi)

ACKNOWLEDGEMENTS

I would like to thank Dr. Ljiljana Simić and Aron Schott M.Sc. for the thesis supervision and full support and availability throughout the process. Additional thanks are due to the same people for giving me the opportunity to work on my thesis at iNets during my Erasmus experience.

I would also like to thank prof. Federico Chiariotti who gave me extreme helpfulness and support by remote to solve complicated bureaucratic issues and provide me with additional insights.

A special thanks then goes to my family, I am realizing day by day how lucky I am to have grown up with you. You are the best I could possibly get. You have made my life simple, free and wonderful.

I also want to thank my friends from Italy who never made me feel lonely by constantly texting and calling me. Almost as if they knew the exact moment I needed them.

Finally, I want to thank my fellow Erasmus adventurers, you made this time special because you are special.

CONTENTS

ACKNOWLEDGEMENTS III

CONTENTS IV

ABSTRACT VI

1 INTRODUCTION 1

2 BACKGROUND 3

2.1 MM-WAVE IN CELLULAR NETWORKS 3

2.2 BEAMFORMING AND INITIAL ACCESS IN 5G CELLULAR NETWORKS . . . 4
2.2.1 THE CONVENTIONAL EXHAUSTIVE SEARCH BASED BT SCHEME . 4
2.2.2 THE HIERARCHICAL SEARCH BASED BEAM TRAINING SCHEME . 5
2.2.3 COMPRESSIVE SENSING FOR BEAMFORMING 6
2.2.4 OTHER STATE-OF-THE-ART BEAMSTEERING ALGORITHMS 7

2.3 POSITIONING INFORMATION TO ASSIST BEAM-MANAGEMENT PROCEDURE 8
2.3.1 POSITIONING INFORMATION DIRECTLY USED TO MINIMIZE THE SEARCH SPACE 9
2.3.2 MACHINE LEARNING BASED BEAM TRAINING SCHEMES 11

2.4 ENVIRONMENTAL AWARENESS VIA RADIO ENVIRONMENT MAPS 13
2.4.1 RADIO ENVIRONMENT MAP DEFINITION AND EXAMPLES 13
2.4.2 DATA ACQUISITION AND REM LEARNING 14

2.5 THE IMPORTANCE OF CONSIDERING LOCATION ERROR IN BEAM-MANAGEMENT ALGORITHMS 15

3 SYSTEM MODEL, SIMULATION SETUP AND METHODOLOGY 18

3.1 NETWORK MODEL AND SCENARIOS 18
3.1.1 NETWORK MODEL 18
3.1.2 CHANNEL MODEL 20
3.1.3 EVALUATION SCENARIOS 22

3.2 GPS ERROR MODEL 25
3.2.1 STATIC ERROR MODEL 25
3.2.2 DYNAMIC ERROR MODEL 27
3.2.3 GPS ERROR DATASET AND MODEL FITTING 28

3.3 SIMULATION WORKFLOW AND PERFORMANCE METRICS 31

3.3.1 SIMULATION WORKFLOW . . . 31
3.3.2 PERFORMANCE METRICS . . . 33

4 SIMULATION RESULTS AND ANALYSIS 36

4.1 SIMULATION RESULTS . . . 36
4.1.1 STATIC SCENARIO . . . 36
4.1.2 DYNAMIC SCENARIO . . . 55

5 CONCLUSIONS AND FURTHER WORK 96

A ABBREVIATIONS 98

BIBLIOGRAPHY 99

DECLARATION 102

ABSTRACT

Millimeter waves (mm-wave) are considered to be the next frontier for data transmission in modern 5G and beyond cellular networks. However, these waves attenuate more easily during propagation and are quickly blocked by obstacles. Therefore, a beamforming operation is necessary, using an array of antennas for transmission instead of a single antenna. Beamforming also requires a search procedure between the transmitter (TX) and receiver (RX), which is inefficient in current networks and causes delays in transmission. However, external information can be leveraged to speed up the alignment process. user equipment (UE) can provide position-related information to the serving base station (BS), enabling the latter to know where to direct the next data transmission. Nevertheless, the auxiliary information is inevitably subject to error, which, depending on its impact, can even impede communication.

In this thesis work, Global Positioning System (GPS) error models are applied in realistic networks scenarios and simulations are conducted to understand the impact of auxiliary information errors on beamfroming-related procedures. Moreover, a ray-tracing channel model has been selected to provide authentic propagation characteristics in the simulation environment.

Keywords: 5G, mm-wave, location-aided beam management, GPS error,

1

INTRODUCTION

Mobile communication is deliberated as one of the fastest developing segment of the communications industry. The evolution of wireless data applications and increasing popularity of smart devices have led to a massive proliferation in mobile data traffic, creating radical challenges for mobile service providers [1]. The evolution of mobile communication systems has witnessed remarkable advancements, culminating in the 5th generation (5G) of wireless technology. One prominent trend within the 5G paradigm and forthcoming cellular networks is the integration of mm-wave frequencies [2]. mm-wave cellular systems, that operate in the 30-300 GHz band, seems to be an auspicious candidate for satisfying the tremendous growth in mobile traffic that will be required in next-generation cellular networks, which is expected to support data rates of multiple Gbps. However, employing mm-wave requires dealing with the propagation attributes and the channel impairments of the high frequency bands. Major impediments of mm-wave propagation are higher path loss due to higher carrier frequency, reduced scattering which in turns reduces the available diversity, and increased effect of blockage as a result of weaker non-line-of-sight paths. To tackle these challenges, directional communication techniques are necessary. These approaches leverage antenna arrays to implement beamforming, and provide a relevant beamforming gain by focusing the power in a narrow beam. However, these directional links, i.e., TX and RX beams, need to be aligned and the best beam-pair-link (BPL) between the two communication sides needs to be found to provide the maximum gain and received power. Thus, beam-management operations are required. Non-standalone beam-management schemes employ available context information of UEs to reduce the complexity of the whole process. One type of such information is UE positioning, which can be used to reduce the searching space in beam-management related tasks. One very relevant aspect in this approach lies on the accuracy of the position information, which is affected by unavoidable errors. Hence, it is imperative to explore and understand the impact of these errors on beam-management algorithms to ensure effectiveness and reliability.

In this thesis, a simulation framework for location-aided beam-management in mm-wave networks is proposed. Specifically, the context information leveraged in beam-management procedures is the UE positioning provided by the UE prior to data transmission. Furthermore, the degrading effect of UE error in positioning is included in the simulation through realistic GPS error models. For the channel model, an open-source mm-wave ray-tracing tool is used to generate site-specific propagation data based on realistic 3D building footprints.

The remainder of this thesis is organized as follows: Chapter 2 addresses the theoretical and conceptual background information to provide a baseline. Furthermore, it motivates the entire thesis highlighting the lack in the literature considering some related work. Chapter 3 provides a complete presentation of the models and evaluation scenarios used in the simulation. It also describes all the approaches pursued in the course of the work. In Chapter 4, the results obtained from the previous described simulations are investigated and discussed. A conclusions along with suggestions for future work is given in Chapter 5.

2

BACKGROUND

In this chapter, state-of-the-art technologies regarding beam management in mm-wave cellular network are introduced. Sec. 2.1 motivates the trend of utilizing mm-wave in modern cellular networks. Sec. 2.2 presents how beamforming and initial access is carried out in 5G networks, and in Sec. 2.2.1, 2.2.2, 2.2.3, 2.2.4 explanation of popular beam training algorithms is provided. Sec. 2.3 introduces the concept positioning information to assist beam management. Sec. 2.3.1, 2.3.2 presents two different approaches to deal with the information collected, respectively using the information for minimizing the beam searching space and machine learning for beam prediction. Sec. 2.4 justifies the importance of environmental awareness in modern cellular networks, and Sec. 2.4.1, 2.4.2 introduce radio environment maps (REMs) and present approaches to build them. Finally Sec. 2.5 stresses the importance of considering positioning errors in beam-management algorithms and motivates the thesis work.

2.1 MM-WAVE IN CELLULAR NETWORKS

Each generation of mobile technology has been characterized by a higher performance demand respect to the previous one, in order to address the challenges not overcome by its predecessor. The 5G is oriented to enable a fully mobile and connected society. For this reason, it has to a tremendous growth in mobile traffic that will be required in the near future. The main requirements are: (i) very high throughput (1 Gbps or more); (ii) ultra-low latency (even less than 1 ms in some cases); (iii) ultra-high reliability; (iv) low energy consumption; (v) ultra-high connectivity resilience and robustness [3]. In order to meet the diverse needs of various applications, numerous solutions have been proposed, such as utilizing higher frequency bands like mm-wave [4]. In particular mm-wave is recognized as the crucial technology for facilitating 5G networks due to its wide unlicensed spectrum and broad bandwidth spanning approximately 2 GHz. Further benefits are: 1) The decrease in the carrier wavelengths allows to pack a larger number of antenna elements in compact forms; 2) Larger bandwidths centred around the main carrier frequencies (35, 94, 140 and 220 GHz) provide very high data rates (up to 10 Gbps), ultra low latency around 1 ms [5]. The ambitious demands in terms of throughput and latency would be then satisfied exploiting mm-wave technologies.

However producing small mm-wave components requires more accuracy and hence, increased costs. Moreover, it encounters low sensitivity in the receiving systems resulting from the reduced energy managed by the small antenna size [5]. Apart form that, the main complication in exploiting mm-wave lies in its physical propagation characteristics. In fact, it exhibits significant propagation and penetration losses caused by its higher frequencies [4]. Signals in the 60 GHz, 120 GHz, 180 GHz bands suffer from an attenuation up to 15 dB/km [5]. Furthermore, mm-wave signals are highly vulnerable to blockage by both static and dynamic obstacles due to their limited ability to penetrate through such barriers. To tackle these challenges, mm-wave networks employ directional communication techniques, leveraging antenna arrays to realize multiple-input multiple-output (MIMO) systems. This approach enables the implementation of beamforming, which enhances the link between TX and RX by compensating for the loss in signal power and providing a relevant beamforming gain by focusing the power in a narrow beam. By adopting directional communication and beamforming, the limitations associated with mm-wave technology can be effectively addressed.

2.2 BEAMFORMING AND INITIAL ACCESS IN 5G CELLULAR NETWORKS

Since directional communication is implemented in 5G, a beam training stage is required to find out the best BPL between the two communication sides. Beam training is an essential procedure in mm-wave initial access (IA), which involves all the steps needed for a new UE to get access to the network. Beam training inevitably carries high delay and power consumption that affect the overall performance of the network. In particular, the performance metrics that are indicators of IA efficiency are [3]:

- *Reactiveness*: how quickly a mobile UE gets access to the network and how quickly is able to detect an updated channel condition;
- *Overhead*: how many time and frequency resources should be allocated for measurement operations.

In the existing body of literature, various methods have been suggested to accomplish mm-wave beamforming. These techniques can be divided into two groups based on their reliance on other frequency bands. The without side information approach consists of standalone beam training schemes, wherein mm-wave transmitters and receivers autonomously identify the optimal BPL to establish a connection. On the other hand, non-standalone beam training schemes utilize contextual information of network UEs to simplify the beam training process. Non-standalone schemes leverage UE positioning details such as location shared on non-data frequency bands to reduce the searching space during the process. In the following, some of the most implemented schemes belonging to the first category are briefly described so that they can be used as a reference to to compare the performances with the more advanced schemes investigated in Sec. 2.3, such as positioning based beam training schemes.

2.2.1 The conventional exhaustive search based BT scheme

Exhaustive search involves systematically evaluating all possible TX-RX beam combinations or solutions to find the one that ensures the best connection. This method is guaranteed to find the best solution since it checks all the combinations, but it may perform poorly in terms of reactiveness and overhead metrics, especially when dealing with a large search space.

In IEE802.11ad protocol, exhaustive search is divided into three distinct sub phases [4]. First, there is the sector level sweep phase, following that is the multiple sector

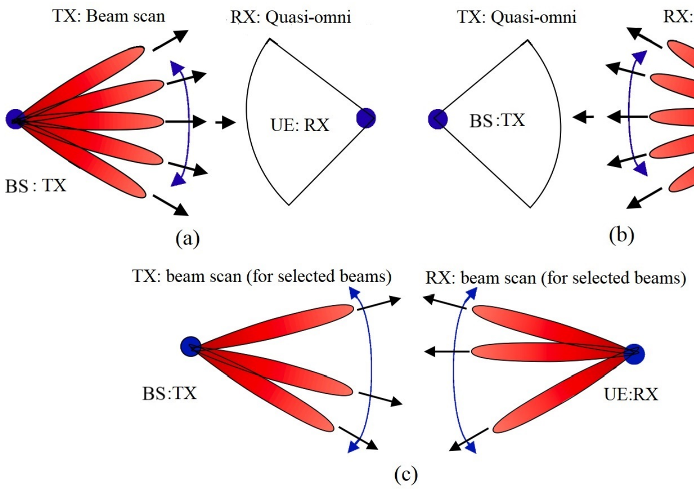

FIGURE 2.1: Exhaustive search based mm-wave beam training process in IEEE802.11ad: (a) sector level sweep sub phase, (b) multiple sector identifier sub phase and (c) beam combining sub phase. Adapted form [4].

identifier sub phase, and finally, the beam combining sub phase. As depicted in Fig.2.1a, the mm-wave BS steers its beam in all directions, while the UE maintains its antenna in quasi-omnidirectional mode. This arrangement allows for the identification of suitable TX beams. In the subsequent multiple sector identifier sub phase, as illustrated in Fig.2.1b, the mm-wave UE steers its beam in all directions, while the BS keeps its antenna in quasi-omindirectional mode. This setup facilitates the selection of appropriate RX beams. These identified TX and RX beams are then utilized for the beam combining sub phase as shown in Fig.2.1c, to determine the optimal TX/RX beam required to establish a high-speed link between BS and UE. In IEE802.11ad example, sector level sweep and multiple sector identifier sub phases need a relevant setup time and a non-negligible power consumption, especially when very narrow beams are preferred.

2.2.2 *The hierarchical search based beam training scheme*

The hierarchical search for beam training optimizes the process of finding the optimal beamforming direction by iteratively narrowing down the search space, in other words, by progressively scanning tighter and tighter angles to focus the beam in the correct direction. With this approach is possible to improve the metrics of reactiveness and overhead respect to the exhaustive search scheme [6]. In the following, IEEE802.11ad protocol for hierarchical search for beam training is explained in details as a possible implementation example [4]. The protocol foresees a codebook/sub-codebook approach where a lower-layer codebooks consist of broader beams compared to the correspondent sub-codebooks (i.e., higher layer codebooks). The spatial resolution improves as the number of layer increases. To carry out the beam training process using the hierarchical exploration approach, multiple stages are perfromed. In each stage, the corresponding codebooks/sub-codebooks of the layer are utilized

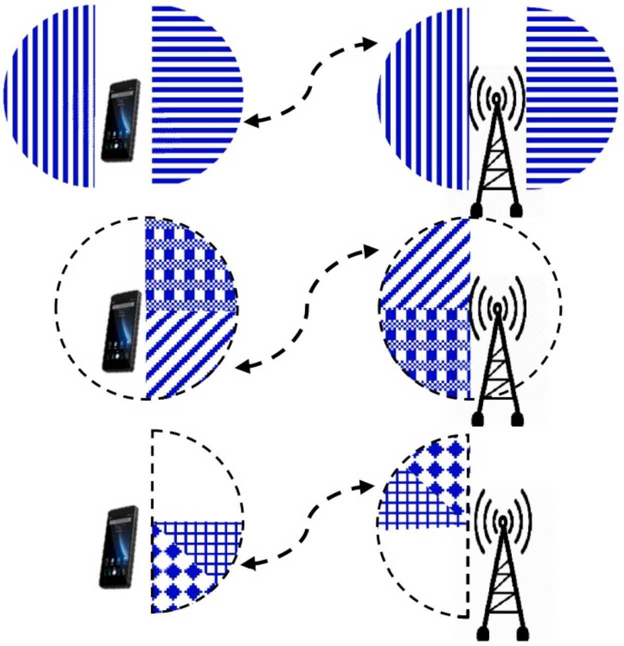

FIGURE 2.2: A 3-layer hierarchical search with $3 \times 2 \times 2 = 12$ beam tuples for mm-wave dawnlink systems. Adapted from [4].

for spatial scanning. The scanning procedure resembles that of the exhaustive search approach, with the difference that we only need to search within the range identified in the previous stage. The UE in the network cell then evaluates the received signal power to determine the optimal beam combination. This information is then provided to the BS to dynamically select the higher-resolution sub-codebooks for the subsequent stage's scanning. This process continued until the desired spatial resolution is achieved. Fig.2.2 illustrates an example of a 3-layer hierarchical exploration for mm-wave downlink systems. In this case, differently from exhaustive search, not all the possible TX-RX BPLs are explored, but there is still a significant burden to the network since the UE needs to transmit feedback information to the BS at each stage, providing scanning results. Furthermore, hierarchical search consumes power at each searching stage. Although this power consumption may be considered low in comparison to the BSs resources, it holds significance for the UEs, which has limited power resources, especially when considering internet of things (IoT) and industrial IoT devices.

2.2.3 *Compressive Sensing for beamforming*

Channel state information (CSI) estimation at transmitter side for MIMO systems requires high complexity due to overhead cost of its feedback. For this reason, beam weight calculation from explicit CSI is very often prohibitive [7]. Because of the unique propagation characteristics of mm-wave signals, it is common for the receiver to detect only a limited number of paths. The transmission channel appears to be sparse in the spatial domain (i.e., it has only a few values significantly larger than the rest [8]), and the communication link relies on a single path, which may be either the line of sight (LoS) or one of the primary reflected paths. For this reason, it is possible to exploit the spatial sparsity of mm-wave signals by applying compressive sensing theory to estimate the angle of departure of those few paths. This way, the power-angle-profile of the propagation channel can be reconstructed in order to assist beamforming. The theoretical background for the application of CS on sparse time and spatial signals can be found in [9].

2.2.4 Other state-of-the-art beamsteering algorithms

In this paragraph, other popular standalone beamsteering algorithms are briefly presented.

Agile-Link: Rather than generating a restricted beam and extracting the power along a single spatial direction sequentially, Agile-Link controls the phase shifters to produce beams with multiple arms, enabling simultaneous sampling of several spatial directions. Because a multi-armed beam merges power from various directions, the receiver cannot promptly determine the specific direction responsible for the resulting power. Nonetheless, Agile-Link employs a mix of randomized multi-armed beams that collectively furnish adequate data for discerning the signal power across all spatial directions [10].

FastND is a greedy algorithm that concludes the beam training immediately upon detecting a decodable link, meaning that it does not attempt to choose the optimal beam pair. The BS periodically sends out beacons. In order to decode the beacon, UEs must strategically adjust the beam from an initial random direction to an angle where it can successfully decode the beacon. If the beacon is not detected, the UE employs a beam prediction method based on accumulate spatial channel information from previous undecodeable beacons to determine the next angle. Upon successfully decoding a beacon, the UE transmits its feedback. The BS acknowledges the link and ends the beam training process [11].

BeamSpy is an algorithm able to predict the quality of alternative beams only inspecting the channel response of the current beam used by the receiver. This way it is able to determine backup beams for link recovery. Beam prediction mechanism relies on specific properties of mm-wave link that are the channel sparsity and channel spatial correlation. [12] provides further documentation on how to exploit those properties in the algorithm.

The authors in [13] demonstrated that the mm-wave beamsteering algorithms presented in this section exhibit sub-optimal performance when evaluated in real outdoor environments. In particular, they overall present sub-optimal performances in terms of reactiveness and overhead evaluation metrics. Consequently, in order to facilitate smooth and high-rate connectivity within forthcoming mm-wave networks, it is imperative to develop more advanced beamsteering algorithms that intelligently adjust to the site-specific mm-wave channel conditions while taking into account the realistic antenna beams of commercially-viable phased antenna arrays. That justifies the need to exploit site-specific information, such as localization and sensing information, to optimize beam-management procedures.

2.3 POSITIONING INFORMATION TO ASSIST BEAM-MANAGEMENT PROCEDURE

In the present times, the concept of positioning has gained more attention from the academic and industrial sectors as it proves beneficial in numerous applications of modern networks like 5G and 6G cellular networks. The knowledge of the UE location holds significant value for the system, offering valuable data for various services such as mapping, advertising, initial access, and tracking. Furthermore, the orientation details of the UE, determined by its internal sensors, play a crucial role in the positioning process. Even a slight rotation of the UE can potentially disrupt the accuracy of the positioning system since that can lead to beam misalignment.

This work focuses on mobile-based methods where the UE location computation is performed at the UE side. Regarding the utilized services for localization, the GPS holds a prominent position as the primary technology for delivering accurate end extensive localization information. However, the efficiency of GPS service diminishes significantly in urban and indoor areas due to the signal blockage, resulting in a non-negligible localization uncertainty. Additionally, the 5G network operates in diverse environments such indoor, urban, and outdoor areas, necessitating highly precise positioning across all these settings. Consequently, alternative technologies like Long Term Evolution (LTE), Wi-Fi, and visible light communication have gained relevant popularity in location-based services for 5G networks, including location based beam training. Various techniques are employed to determine device locations, these are schematized in Fig.2.3 and summarized in the following [14]:

- *Trilateration/Multilateration*: The location outcome is achieved by calculating the point where geometric shapes, like circles or hyperbolas, formed by measuring the distances between the UE and the reference transmitters or receivers, intersect. Multiple kinds of measurements, such as time-of-arrival, difference in time-of-arrival, or received signal strength (RSS), can be employed to estimate the radius of the geometric shape.
- *Triangulation*: The direction or angle of arrival of the received signals is used to estimate the position by using the intersection of at least two known directions of the incoming signal.
- *Proximity*: The UE position is simply designated to be the same as the known serving BS.
- *Fingerprint*: The approach involves two different phases: an offline phase and an online phase. During the offline phase, a database consisting of fingerprints linked to specific locations is generated. Subsequently, in the online phase, the localization coordinator compares the incoming signal, such as RSS, from the device undergoing localization, with the pre-established database in order to estimate the UE location.

Multiple authors presented mm-wave beam training and beam tracking techniques that rely on positioning methods. These approaches mainly leverage UE's location information (provided by one of the aforementioned positioning services) to narrow

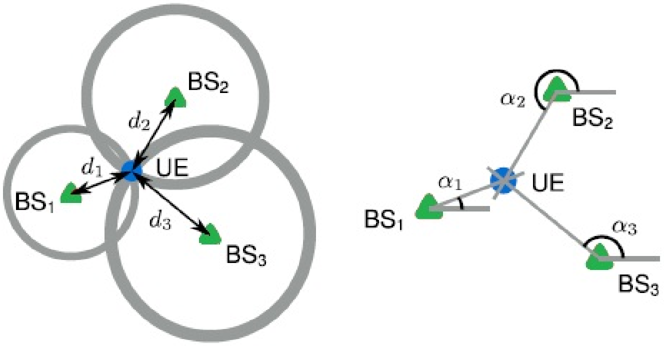

(a) Trilateration/multilateration (b) Triangluation

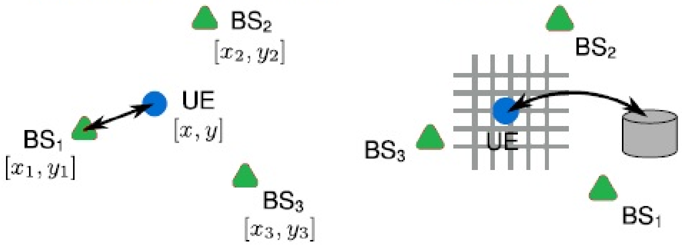

(c) Proximity (d) Fingerprinting

FIGURE 2.3: Fundamental positioning techniques. Adapted from [14].

down the search space for identifying the optimal TX/RX BPL for mm-wave communication links. In general, we can categorize these methods in two main groups: positioning information to directly enhance the training criterion, and machine learning based beam training schemes.

2.3.1 *Positioning information directly used to minimize the search space*

Beam training operation without accurate UE positioning data is completed by using one of the algorithms presented in Sec. 2.2. In all those cases, the network needs to explore a broad range of potential beam direction because of the random nature of UE positioning in the cell. In general, this wide exploration of beam angles causes large network reactiveness and overhead. However, when UE's position is known with a certain precision, the network can significantly narrow down the potential beam directions that need to be tested, leading to a quicker beam alignment. In fact, the beam training process can focus on a smaller subset of beam angles that are more likely to yield to successful connection. This targeted approach results in a reduced overhead since it cuts down the number of training iteration required. For the same reason, reactiveness metric decreases as the overall time UE takes for IA.

Positioning information and, more in general, helpful context information (RSS, angle-of-arrival, etc.) can be shared employing a distinct control plane (C plane), as it is proposed in [15]. In the work, context information are used to minimize the searching space in a predefined beamforming codebook. A beamforming codebook is a set of predefined beamforming vectors, each vector correspond to a particular direction or angle in space. Knowing the context information, the network can then

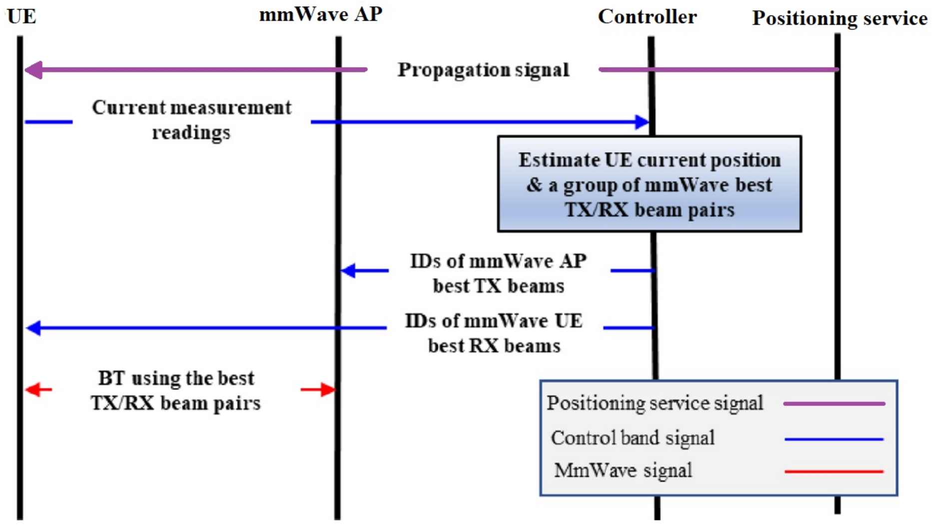

FIGURE 2.4: Workflow in BT schemes using positioning information to directly minimize the searching space. Adapted from [4].

focus on a reduced number of codebook entries. In Fig.2.4 a detailed scheme of the procedure is presented. Specifically, four entities are involved: UE, mm-wave access point, a controller collecting and utilizing the context information, and the positioning service (GPS in this case). First the positioning service provides UE's position information, that is then delivered to the controller via the control band. The controller estimates UE's position and computes a group of mm-wave best TX/RX BPLs. IDs of best TX beams and RX beams are then communicated respectively to the mm-wave access point and UE again via control band. Once the two communication sides are informed about the best beams, the data transmission can take place in the designed mm-wave band.

Another possible approach is presented in [15] where context information are used to select two important beamforming parameters: beam-width θ_{-3dB} and pointing direction d. In the same work the following cell discovery algorithm is proposed: when a new UE enters the cell, the serving BS computes the appropriate beamwidth θ^{*}_{-3dB} and the pointing direction according d^{*} based on the estimated position context information. If the position estimate is not precise, there is a possibility that the UE is not detected. In such cases, the BS scans the surrounding environments using circular sectors. The BS initiates exploration beam directions adjacent to d^{*} within the first scanned sector, employing a fixed beamwidth θ_{-3dB} to cover the sector. The exploration proceeds by alternating between clockwise and counter-clockwise directions. If no UEs are reached, the BS reduces the beamwidth, reorient the beam towards the estimated UE position, and continues exploring adjacent beam directions within the sector. Once the scan of the sector is completed without locating the UE, the same per-sector beam scanning procedure is repeated for the remaining $n-1$ adjacent sectors, again alternating between clockwise and counter-clockwise sectors. The process ends when the UE has been detected or when all n sector have been probed, resulting in an unreachable UE. This algorithm is a rather simple and intuitive example of how context information could be exploited to ease the UE discovery. In the literature different approaches are proposed for different aims (See [16] where context information is used to derive and analyze the capacity of a beamformed radio link, and [17] where a location-based cell selection scheme that takes into account the effects of inaccuracy of the location estimation is introduced).

Beamforming using compressive sensing can also leverage context information to simplify channel estimation. The basic idea consists in using UE and BS estimated locations to reduce the number of beamforming vectors to build the sensing matrix used for channel estimation. This leads to a reduced complexity and setup time of the beamforming process. A similar procedure is followed in [18], where compressive sensing is used for accurate estimation of channel parameters. However, the overall complexity and setup time of location based compressive sensing is still larger than location based codebook approach, as outlined in [4]. For this reason, compressive sensing using position information is only viable where accurate channel estimation parameters are required.

In all the cases presented, the context information utilized in the algorithm can be affected by errors. The aspect of uncertainty in the information provided by the service must be taken into account in the analysis and is further discussed in Sec. 2.5.

2.3.2 *Machine learning based beam training schemes*

This second category of schemes exploits various learning techniques such as statistical, probabilistic, and pure machine learning approaches. Specifically, machine learning algorithms such as support vector machines, neural networks, deep neural network can be exploited to make beam predictions for new UEs after a training procedure. The general workflow can be distinguished into two separate sub-phases: an offline sub-phase and an online sub-phase, as it is schematized in Fig.2.5. In the offline sub-phase the mm-wave access point makes use of the positioning service to collect data from new UEs through the control band, carry out the beam training processes, and communicate the corresponding beam IDs to the controller entity. Thanks to these measurements, the controller constructs the database for the training procedure. Explicitly, UE positioning information is the training instance and the corresponding TX beam ID is its training the label. As learning theory states, the larger is the database, the more reliable is the resulting output mapping function between the position and the best beam. In the online sub-phase, the controller reads the information provided in the control band by new incoming UEs and, according to the predictor's output, determines a group of best mm-wave BPLs. After that, the best TX and RX beam IDs are communicated respectively to the mm-wave access point and UE via control band. Once the two communication sides are informed about the best beams, the data transmission can take place in the designed mm-wave band. A similar approach is followed in [19], where statistical learning is used for best beam prediction after a fingerprint database construction during the offline phase.

A drawback of the beam training schemes using database lies in the storage overhead [4]. Creating a large enough database and storing of positioning information within it necessitates a significant amount of memory space. Whether it involves fin-

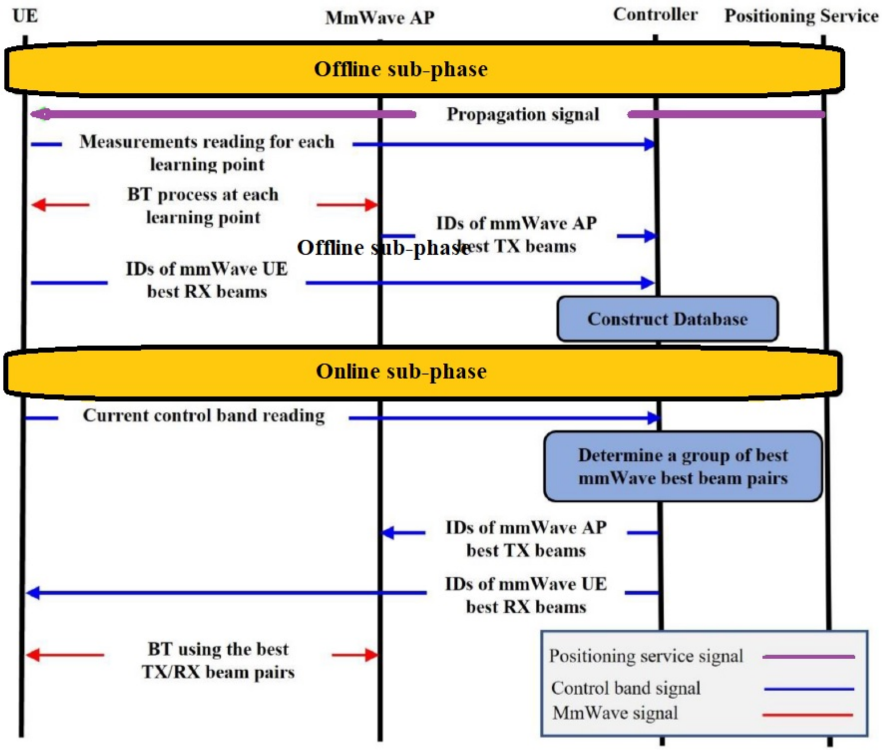

FIGURE 2.5: General workflow of learning-based beam training schemes. Adapted from [4].

gerprinting information or current and previous data for each UE in the network, the storage requirements can be substantial. Moreover, they cannot handle any changes in the environment, e.g., mobile obstacles and devices, because these models are trained offline.

Machine learning based beam training schemes pros and cons stand out in [20], where the problem of position-aided beam prediction is revisited in light of real-world measurements taken with commercial GPS devices. The authors propose three different approaches to construct the mapping function between the position in a cell and the best beam: lookup table, K-nearest neighbors and a fully connected neural network. In the work, intuitive approaches such as lookup table are compared with supervised machine learning ones, like fully connected neural network. The lookup table solution simply consists in discretizing the input space into small squared areas and and geometrically mapping each one of them to the correspondent best TX beam ID . The rationale behind K-nearest neighbors is that similar/neighbor positions should have similar optimal beams. N_{knn} nearest neighbors are first identified, then the selected neighbors report their best beam to the transmitting BS. The standard fully-connected neural network is trained checking the accuracy in the validation set that is the 20% of the collected data (60% training, 20% validation, and 20% testing). Eventually, according to [20] the fully connected neural network outperforms the other algorithms in terms of beam prediction accuracy in a real-world scenario. It is also important to outline that the fully connected neural network requires high computational complexity that could not be supported in some use cases. Moreover, the effectiveness of the procedure is proportional to the accuracy of the information in the database. Essentially, machine learning and database approaches in general find the inaccuracy of the positioning service as the main worsening factor [20]. The dataset must be reliable, but since it was constructed using positioning service measurements, e.g., GPS measurements, it ends up with some errors. This is a common factor with the schemes explored in Sec. 2.3.1, for this reason modeling positioning errors is a must in the overall analysis (see Sec. 2.5).

2.4 ENVIRONMENTAL AWARENESS VIA RADIO ENVIRONMENT MAPS

The importance of exploiting UE location information and, more in general, context information in the beam management procedure has been outlined so far in the work. Environmental awareness is an important network goal as beamsteering algorithms must be adjusted to site-specific channel conditions [13].

To demonstrate the potential impact of environmental-awareness, we examine two simple instances. Fig.2.6a depicts two UEs situated at equal distances from the BS, but with a building obstructing the path between UE2 and the BS. According to the conventional distance-dependent path loss model, one might erroneously assume that UE1 and UE2 have identical channels with the BS (at least from a statistical prospective), which is evidently incorrect. In reality, to draw a more accurate conclusion that UE2 experiences a poorer channel that UE1, one simply requires knowledge of the BS and UE locations, along with details about the building's attribute like location and size. Such information is either static or readily accessible through built-in sensors like GPS receivers. With environment-awareness, a communication system can precisely predict the channels based solely on location information, even before employing advanced channel estimation techniques like pilot-based training. As an alternative example, Fig.2.6b presents two beamforming strategies that do not require training. The first is location-based beamforming, where the signals are simply directed towards the UE's location. The second approach is environment-aware beamforming, where the signals are directed towards potential reflectors/scatterers that can guide the signal to the UE. Although both training-free beamforming methods rely on location information, the utilization of environmental knowledge in the latter enables a more substantial beamforming gain.

2.4.1 *Radio environment map definition and examples*

REMs are the main enablers toward environment-aware wireless communications according to the literature. A REM is a site-specific database, tagged with the locations of the TXs and/or RXs, that contains channel-related information useful to enhance environmental-awareness and facilitate real-time channel state information acquisition. Consequently, REMs are anticipated to have a significant impact on 6G networks aiming for high capacity, ultra-massive connectivity, by offering potential solutions to modern challenges brought by the significantly channel dimensions increase and training overhead [21]. That is because the network can take advantage of the location-related information stored in the beam alignment algorithms.

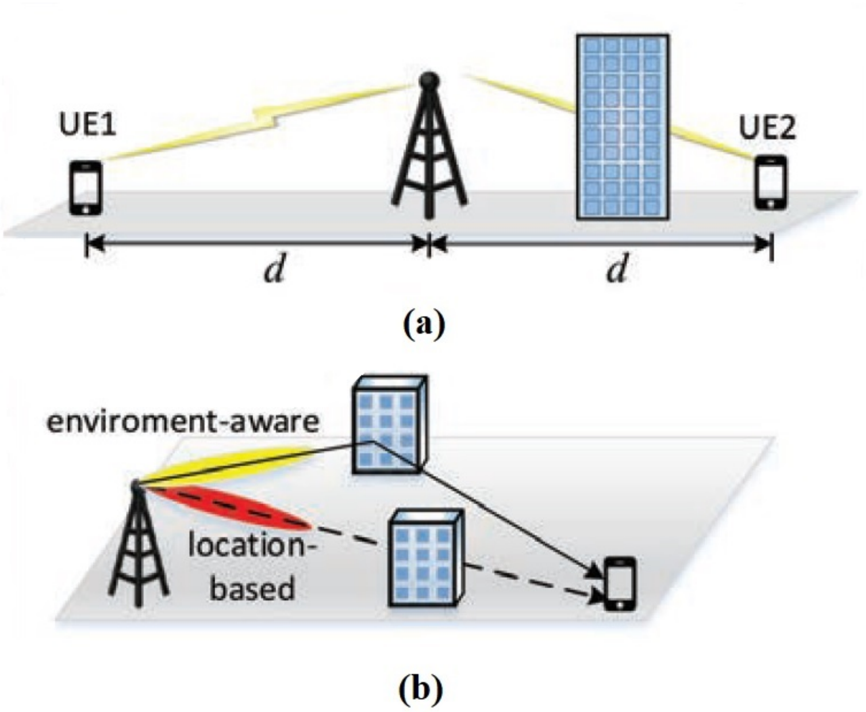

FIGURE 2.6: a) environment-aware channel gain prediction; b)environment-aware versus location-based training-free beamforming. Adapted from [21].

One basic example of REM is channel gain map, which is containing the channel gains of wireless links in a target area. Other possible instances of REMs include channel shadowing maps that predict the location-specific shadowing loss. Another option are channel path maps which predict the location-specific channel path information, such as the number of significant paths and their powers, phases, delays, angle-of-arrivals/departure, and so on. In [22], two specific types of REMs are proposed for hybrid beamforming design in mm-wave massive MIMO systems namely channel angle map that predict the location-specific channel angle information (i.e., angle-of-arrivals and angle-of-departure) of the potential channel paths, and beam index map that aims to provide the location-specific candidate transmit and receive beams for all possible UE locations. Simulation results over practical propagation environment demonstrate that the presented approach significantly outperform the benchmark schemes, even with moderate error on the UE location.

2.4.2 Data acquisition and REM learning

The information needed to construct a REM can be obtained through offline numerical simulations as well as online measurements. Offline simulation enables the generation of location-specific channel knowledge by ray-tracing based on the available online information on the physical environment. While offline simulation-based data acquisition is a cost effective approach, the quality of the resulting data relies on the accuracy and level of detail regarding the physical environment model. The authors in [23] show that ray tracing captures well the distribution of the multipath signal clusters in terms of number of multipath clusters per RX location, angle-of-arrival, angle-of-departure and individual cluster structure. Moreover, the results indicate that ray-tracing provides accurate propagation data based on publicly available 3D building models. That makes ray tracing a valuable tool to construct REMs via offline simulations.

On the other hand, data could also be collected online concurrently when actual communication takes place. Compared to offline simulation, the online measurement-based data collection is expected to provide more accurate data that better reflects the reality of the radio propagation environment, through with higher implementation cost. Thus a combination of the the online and the aforementioned offline data collection methods could be used to complement each other. For example, building a coarse REM based on offline numerical simulation and redefining it with online measurements. Another strategy to densify a coarse REM is to apply interpolation or learning techniques. In particular, deep neural networks can be trained and used to predict the interested channel knowledge given the RX location as the input [21].

When considering all data acquisition and densification methods, a fundamental questions arises regarding the appropriate frequency of data along the spatial and temporal dimensions in the REM. Intuitively, this depends on the specific type of channel knowledge provided by the REM and its corresponding spatial or temporal coherence distance/time. For example, regarding the spatial dimension, for large scale channel knowledge such as channel shadowing maps, data sampling on meter-level is typically sufficient, while for instantaneous channel state information due to multipath fading and Doppler frequency shift the data sampling must be much shorter in extension.

A final aspect is considered here regarding the availability and quality of data used to build REMs. Of course, the practical usefulness and implementation of these maps strictly depends on how accurate the data are [21]. For instance, if data are collected through wireless networks with a specific service, they will be affected by an error and this should that may or not impact on the final performance dependently on the specific map usage.

2.5 THE IMPORTANCE OF CONSIDERING LOCATION ERROR IN BEAM-MANAGEMENT ALGORITHMS

The accuracy of position-aided beam-management heavily relies on accurate localization information, which is affected by unavoidable errors. Hence, it is imperative to explore and understand the impact of these errors on beam-management algorithms to ensure their effectiveness and reliability. Localization errors are intrinsic nature of wireless communication systems. These errors can arise form factors such as multipath propagation or non-line-of-sight (NLoS) conditions. For instance, multipath errors in GPS are the result of satellite signals bouncing off landscape features like buildings, trees, or the ground before entering the device [24]. The presence of these inaccuracies can have a profound impact on beam-management algorithms, potentially leading to degraded system performance. First of all, inaccurate localization information can lead to improper beam alignment, resulting in a reduced signal

References	Accuracy effect	Realistic scenario	Error autocorrelation
[28]	No	No	No
[29]	No	No	No
[16]	Yes	No	No
[30]	Yes	Yes	No
[17]	Yes	No	No
[25]	Yes	No	No
[20]	Yes	Yes	No

TABLE 2.1: Comparison between positioning-based BT schemes in related works.

quality and increased interference. Beamforming techniques heavily depend on the accuracy of location estimates to align the beamforming vectors precisely, and errors in localization can lead o misalignment resulting in signal degradation and reduced system capacity. Moreover, localization errors can affect beam selection algorithms, which aim to choose the most suitable beam for each UE. Erroneous location information can lead to incorrect beam associations, causing unnecessary beam switches and reduced spectral efficiency. Also beam tracking procedure may be affected by inaccurate localization information, making it challenging to maintain stable and reliable beam connections over time. Beam tracking errors can result in frequent handovers, increased overhead, and disrupted communication links [25].

To ensure the effectiveness and reliability of beam-management algorithms, it is crucial to account for localization errors during their design and optimization. Errors need to be modeled in a realistic outlook starting from realistic mm-wave network scenarios. Moreover, the specific nature of the localization service involved needs to be considered. Many papers dealing with the topic of beam-management under position uncertainty simply model GPS uncertainty with a Gaussian distribution [16], [25]. Works related to GPS error modeling, such as [26], state in most of the cases that is a too simplistic assumption. In fact, if a Gaussian model is used to fit the error, it will have to have an artificially large variance to account for the outliers. Most importantly, the model will not account for the autocorrelation since Gaussian processes totally lacks of autocorrelation. Instead, [27] proves with on-field measurements on real trajectories traveled by walking, that GPS error features a relevant temporal and spatial autocorrelation.

Some of the related work in location-aided beam management are compared in Tab.2.1. Part of those papers do not even consider the topic of position information inaccuracy in their design, they in fact assume perfect context information at the TX side [28], [29]. This assumption is highly unrealistic for the aforementioned reasons. The second metric in 2.1 is related to the fact that the mm-wave network model considered should take into consideration the surrounding environment in a realistic way. That is also important since the design of a beam-management algorithm needs to be site-specific and site-optimized. The last metric examined in the table is the usage of a realistic enough error model that, as already said, should include GPS error autocorrelation. Most of the state-of-the-art related works, as the aforementioned [16] or [30], use a too simple approach in their error modeling.

As we can see from Tab.2.1, even if some of the works evaluated adapt their proposals to a realistic mm-wave scenario, none of them considers the specific error autocorrelation of the positioning service involved in the beam-management algorithm presented. The current thesis work attempts to further investigate this last aspect due to the lack in the literature. It exploits simulation tools on realistic network environment to outline the impact of positioning error on beamforming-related tasks.

3

SYSTEM MODEL, SIMULATION SETUP AND METHODOLOGY

In this chapter a complete presentation of the models and evaluation scenarios used in the simulation is furnished. Sec. 3.1 presents the network model in the study area the ray-tracing channel model applied. Moreover, the two evaluation scenario considered, respectively static and dynamic scenarios, are introduced. In Sec. 3.2 and relative subsection the selected static and dynamic GPS error models are described. In addiction, the error model fitting procedures are motivated. Finally, in Sec. 3.3 the decided simulation workflow and performance metrics are presented.

3.1 NETWORK MODEL AND SCENARIOS

In this section, the basis for the work is presented through the description of the network model in Sec. 3.1.1 and channel model in Sec. 3.1.2. Moreover, the two different evaluation scenarios for the simulation are introduced in Sec. 3.1.3.1 and Sec. 3.1.3.2.

3.1.1 Network model

The mm-wave network urban scenario of interest is at the BackstrinngebÃ¤ude area in the German city of Aachen. Fig.3.1 shows the study area seen from the top.

We consider a network composed by one single TX that is the cell BS, and every potential RX location measures $1m^2$ in area. The overall extent of the study area totals $350 \times 350m^2$, which makes up a grid of discrete receiving locations where the UE can be. The value of $1m^2$ of grid resolution is considered suitable for highlighting relevant differences in mm-wave signal reception between adjacent locations. The TX transmits at the central frequency of $f_c = 58.32\ GHz$, with a total system bandwidth of $B = 400\ MHz$. The TX uses a 8×8 antenna array and the RX uses a 4×4 antenna array. Both TX and RX use predefined codebooks and beam IDs. In particular, the TX has the possibility of switching among 64 different beams spanning the whole $360°$ space around it (i.e., the TX beam amplitude is $5.625°$). Instead, the RX is able to switch among 16 beams spanning the $360°$ space around (i,e., the RX beam amplitude is $22.5°$). A scheme of TX and RX beam IDs are shown respectively in Fig.3.2a and Fig.3.2b. In both cases beam ID number 1 is pointing East and the other ones are numbered counterclockwise. Fig.3.3 and Fig.3.4 show antenna patterns in azimuth cut for some example ID entries in TX and RX codebooks respectively. As we can see, every ID's pattern has a primary lobe that has a maximum corresponding to the predefined emission direction. For example, $ID = 1$ pattern finds its maximum for $\phi = 0°$ corresponding to the East direction.

FIGURE 3.1: SuperC/Backstrinngebäude area, Aachen.

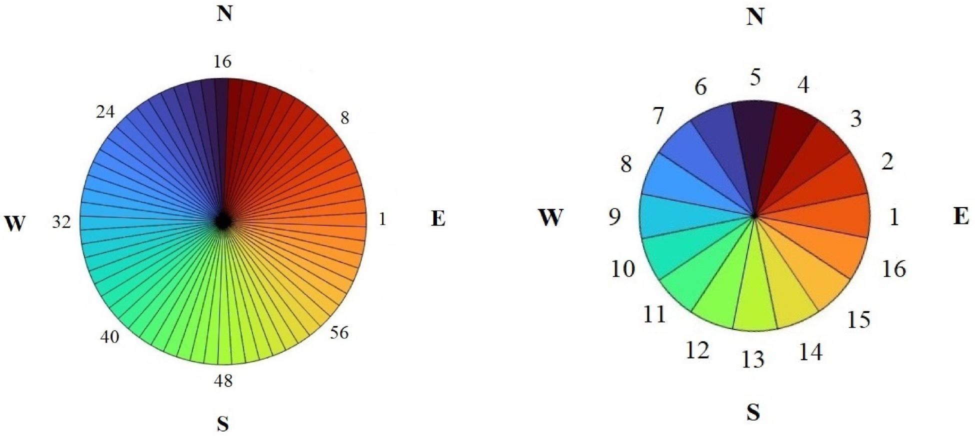

(A) TX beam IDs

(B) caption 2

FIGURE 3.2: Beam direction scheme for TX and RX with respect to the cardinal points.

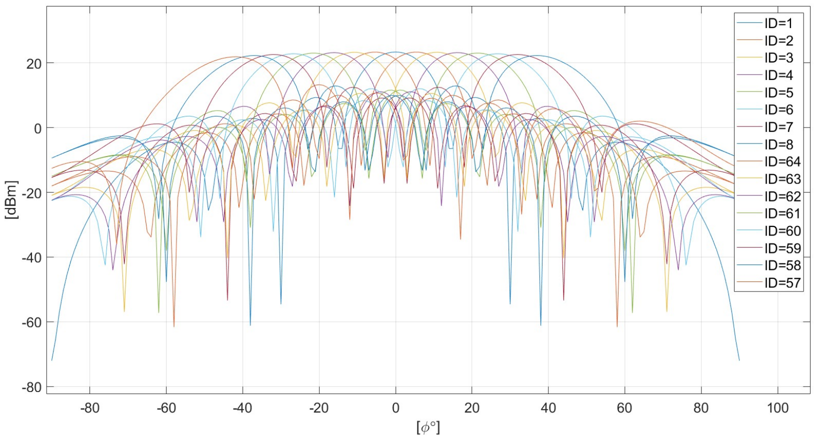

FIGURE 3.3: TX beam pattern in azimuth cut for selected example beam ID entries.

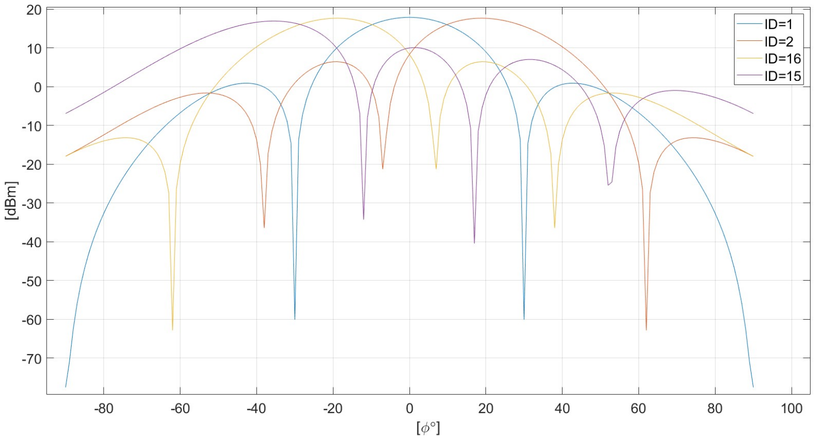

FIGURE 3.4: RX beam pattern in azimuth cut for selected beam ID entries.

3.1.2 *Channel model*

For the channel model, an open-source mm-wave ray-tracing tool [31] is used to obtain site-specific propagation data, based on publicly available 3D building data. In Fig.3.5 the ray-tracing building data are shown for the considered area, moreover TX and one potential RX are highlighted. In the simulation, free space propagation and strong reflections with up to two bounces are considered to be the dominant propagation mechanism; diffraction and scattering are neglected since they play a minor role at mm-wave [32]. The ray-tracing output is an inventory of all available propagation paths for each RX position in the aforementioned discrete grid. For each available propagation path k, the ray-tracer gives the: (*i*) type of path (LoS or NLoS), (*ii*) angle-of-arrival, angle-of-departure, (*iii*) path loss calculated as the free-space path loss plus any reflection losses. The nominal transmit power is $P_{TX} = 16dBm$.

FIGURE 3.5: Building data considered in the ray-tracing simulation. TX and one potential RX are highlighted.

Given the TX and RX antenna gains from the patterns shown in Fig.3.3,3.4, and the knowledge about the propagation paths from the ray-tracing simulation, it is possible to draw some conclusions about TX and RX antenna gains in the direction of an arbitrary propagation path. In general, the TX and RX antenna gains in the direction of the propagation path k between the TX and RX when their main lobes are steered respectively towards the directions corresponding to the serving beam IDs i and j, are given as

$$G_{TX,i,k} = G(\phi_{TX,k} - \phi_{TX,i}) \tag{3.1}$$

$$G_{RX,j,k} = G(\phi_{RX,k} - \phi_{RX,j}) \tag{3.2}$$

where $\phi_{TX,k}$ and $\phi_{TX,i}$ are respectively the k path azimuth angle of departure, and the TX main lobe direction given by the TX beam $ID = i$ azimuth angle. Similarly, $\phi_{RX,k}$ and $\phi_{RX,j}$ are respectively the k path azimuth angle of arrival, and the RX main lobe direction given by the RX beam $ID = j$ azimuth angle. Thanks to the path-related beam gains, it is possible to compute the total RSS given by the $\{i, j\}$ TX-RX beam combination. Given K propagation paths for the RX location (including both LoS path and all the NLoS paths), $RSS_{i,j}$ can be written as

$$RSS_{i,j} = P_{TX}\left(\sum_{k}^{K} PL_k G_{TX,i,k} G_{RX,j,k}\right) \tag{3.3}$$

where PL_k is the propagation loss of path k.

BPL (i, j)	**RSS [dBm]**
$(1, 1)$	$RSS_{1,1}$
$(1, 2)$	$RSS_{1,2}$
$(1, 3)$	$RSS_{1,3}$
.	.
.	.
$(64, 16)$	$RSS_{64,16}$

TABLE 3.1: BPL matrix for a given RX location.

Given the fixed RX position, a BPL matrix can be built. BPL matrix refers to a matrix that represents the potential communication links in terms of RSS between pairs of TX-RX beam combination. In Tab.3.1 a summary scheme of BPL matrix is shown for a RX placed in a generic position in the grid.

Following the procedure described, a 16×64 BPL matrix can be built for each location in the network grid. The result is the REM in which the channel related information per location is the BPL matrix. The dataset described provides complete information regarding the optimal TX-RX beam combination for every potential receiving location in the grid. This serves as the baseline to evaluate the performance degradation once applied the location error models presented in Sec. 3.2.1, 3.2.2.

In Fig.3.6 the omnidirectional RSS per position (i.e. the RSS given by the sum of all the propagation paths ending in that position in the grid) is shown with a heatmap. As we can see from Fig.3.6, signal is stronger in position closed to the TX and it progressively decreases with distance. The signal then suddenly decreases in the transition form LoS to NLoS condition. We can also notice that some locations that are in NLoS condition can be reached only thanks to signal reflections. Moreover, some of the positions are white since they can not be reached by the transmitted signal. In addition, the dataset does not provide data at the places corresponding to the buildings considered by the ray-tracing building model.

3.1.3 *Evaluation scenarios*

3.1.3.1 *Static scenario*

The first scenario evaluated is specific to the initial access procedure in a mm-wave network. Initial access in mm-wave cellular networks involves beam training which can be simplified using UE location information via location-based beam-management. More specifically, let us assume that a UE that is not connected to the network is placed in a certain location in the network area. It first shares its position through the dedicated link (e.g., via control band) to the BS, then, after the required beam-alignment steps, the directional data transmission can take place. In our case, once BS is updated with UE position, the REM described in Sec. 3.1.2 is queried and the best beam choice can be made for that position. We also consider in Sec. 4.1.1.2 the realistic case in which the map is erroneously built using measurements reported by UEs. As a consequence, the the incorrect BPL matrix may be stored for the position notified, leading to a systematic error in the following querying. In both the cases described,

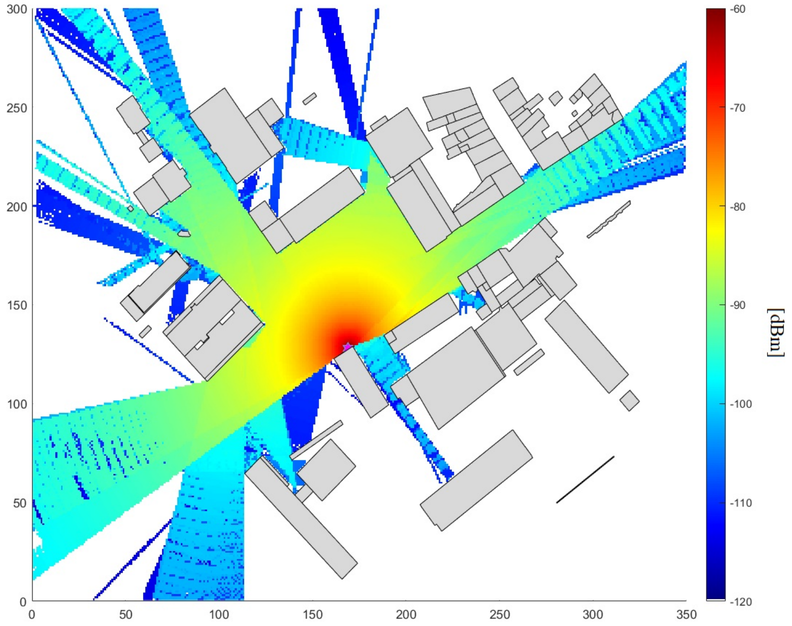

FIGURE 3.6: Heatmap showing the omnidirectional RSS in the study area.

UE position sharing is then affected by the error that is modeled and described in Sec. 3.2.1.

3.1.3.2 *Dynamic scenario and mobility paths*

The second scenario is emulating the beam tracking procedure in a mm-wave network. Beam tracking is the procedure through which already connected UEs moving in the cell maintain beam alignment respect to the BS. In fact, the BPL established for a given location may not be optimal once the UE has moved even a little, that is because beam-alignment condition may fail. BPL needs then to be updated over the time since UE mobility is a very common condition. Also beam tracking procedure can be facilitated by providing periodic location information to the BS, but the positioning notification is affected by error also in this case. Two error models are considered in this scenario: the first one is the correlated error model described in Sec. 3.2.2, then a simple uncorrelated Gaussian error model is applied. The reason to move from one to another is to outline the effect of error autocorrelation in a scenario where it should be considered, but, as outlined is Sec. 2.5, in most of the state-of-the-art papers it is not.

To evaluate the performance degradation using the error models, three mobility paths in the simulation area have been selected and are shown in Fig.3.7. The choice for the specific path was made considering the following criteria: i) the paths must emulate typical pedestrian routes in the area , ii) they need to be quite different one from each other, iii) a relevant channel variation should be experienced during the walk.

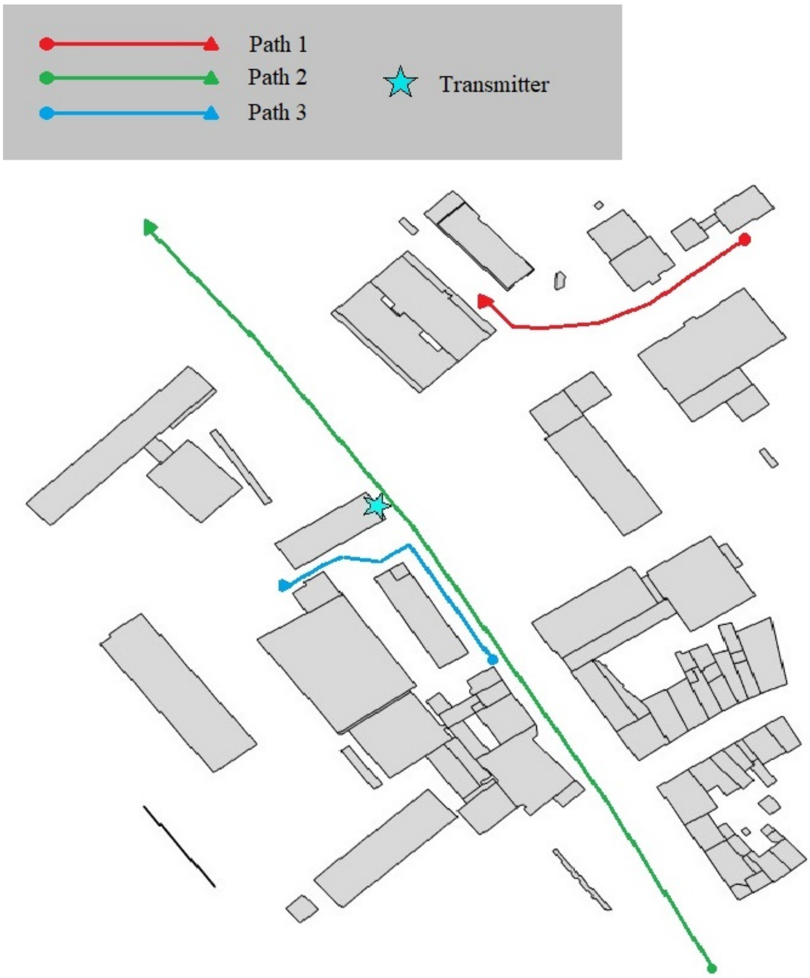

FIGURE 3.7: Paths considered in the simulation. The map of buildings has been rotated 90 degrees to the right from the one shown in Fig.3.6 and previous. This is to be consistent with the locations in the original dataset and it is done to facilitate references to error model realizations in the paths shown in Sec. 4.1.2.

As it can be seen from Fig.3.7, Path 1 is quite far from the TX position and a transition from LoS to NLoS condition is experienced around the end. Path 2 is entirely in LoS condition but an important channel variation is still be experienced because it starts from a very far position from the TX, gets close to it and walks away again. Path 3 is always pretty close to the TX and it experiences a sudden channel variation due sudden change in path direction with a corresponding transition of the connection from LoS to NLoS. The speed with which these paths are traveled in the simulations is always $1m/s$, meaning that the pedestrian is moving in the network grid from a location to a nearby one one in a time equal to $1s$.

3.2 GPS ERROR MODEL

The importance of modeling location service errors has been outlined in Sec. 2.5. For all the following evaluations, we refer to the GPS as the location estimation provider as GPS is the most widely used technology for localization in mobile applications. Moreover, its integration can play a pivotal role in enabling accurate beam-management processes. In this work, two different error model strategies are used: the first one's aim is to emulate the uncertainty in the position information provided by a new user accessing the network area covered by a BS; the second one is modeling the uncertainty of successive locations while the UE browses a path covered by the network cell.

3.2.1 *Static error model*

The first error model is specific to the initial access scenario (static scenario described in Sec. 3.1.3.1). Since in this first framework models the uncertainty in the first position estimation provided by a new UE's GPS system, there is no need to track for error time-space evolution. The idea is then to model the two-dimensional position error of the GPS with a statistical distribution that is both realistic and easy enough to implement in simulators.

The authors in [33] executed two abundant measurement campaigns (900000 and 237000 measurements respectively in two different geographical position) to evaluate GPS error statistical distribution. Then, the evaluation consists in selecting the commonly used distributions that provides the best fits with respect to the empirical data. In [33] the fit accuracy is evaluated in terms of probability density function (pdf) difference between the empirical data and the theoretical distributions. Results show that a normal distribution provides a good fit, while a logistic distribution performs even better. For this reason, normal and logistic shapes are the chosen error distributions for simulations in this first error scenario. Fig.3.8 compare normal and logistic pdfs for the same variance. In the case of logistic shape, the dispersion parameter provided as input to the curve is the scaling parameter s. The scaling parameter s can be computed form the selected variance Var with the following equation:

$$s = \frac{\sqrt{3}Var}{\pi} \tag{3.4}$$

As we can see from Fig.3.8, logistic shape has a rapid growth in the central part and slightly heavier tails respect to the normal shape. In our case, logistic distribution

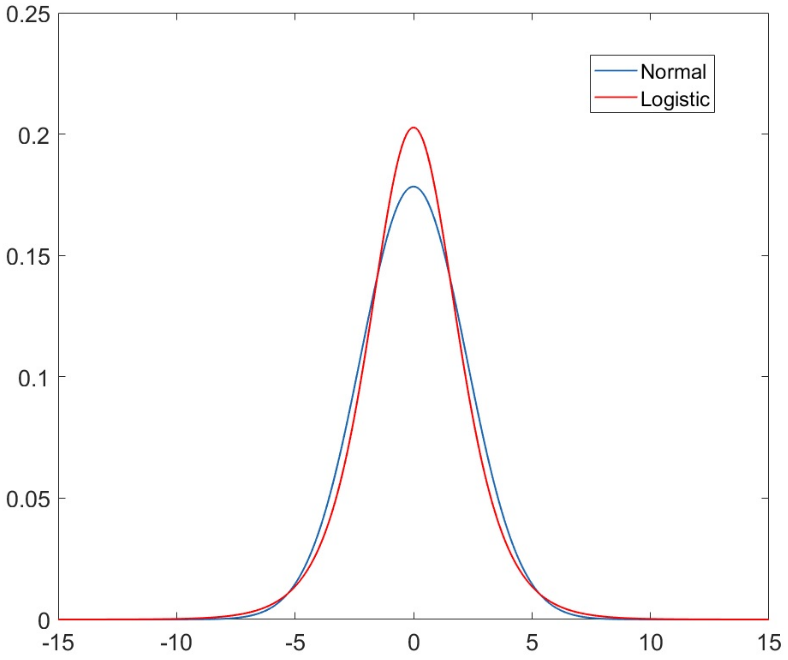

FIGURE 3.8: Gaussian pdf with standard deviation value $\sigma = \sqrt{5}$ (blue) and logistic pdf with scale parameter $s = \sqrt{5}$ (red) comparison.

makes either very small GPS errors or very large GPS errors more likely than the normal distribution having the same variance.

The other aspect of the problem is related to error variance (or standard deviation) tuning. In fact the more higher the error variance is the more the error impacts the simulated position estimation. The tuning procedure depends on many factors, the most important ones are the GPS device accuracy and the specific environment characteristics. Regarding the first factor, this work refers to typical commercial GPS receivers installed in mobile phones that neither have built-in error compensation mechanisms, nor external correction sources. The authors in [33] utilized GPS receiver including wide area augmentation system corrections [34], this results in finding GPS error variances that are too small for our hypothesis. The other main element contributing to error variance is the specific environment where the mm-wave network is operating. Intuitively, we expect a much larger GPS error in dense urban areas rather than in an open areas, since the main source of GPS errors are GPS signal bouncing off landscape features like buildings, trees, or the ground before entering the device [24]. For this reason, the variance decision is made considering GPS measurement datasets collected in different urban density areas through GPS receivers installed in typical mobile phones. More details about the GPS datasets in Sec. 3.2.3. Thanks to this analysis, it is possible to estimate an error variance range spanning different environments. The different values for latitude and longitude error variances that will be used in the simulations are summarized in Tab. 3.2.

From this it becomes clear that the longitude error variance is always smaller than the respective latitude error variance. In particular, they approximately follow a $\frac{3}{4}$

Variance set ID	Latitude error variance (m^2)	Longitude error variance (m^2)
1	0.5	0.37
2	1	0.75
3	5	3.75
4	10	7.5
5	30	22.5

TABLE 3.2: GPS error variances considered in the simulation performed.

proportional ratio. That comes from the analyzed error datasets and it is confirmed by [33], according to which GPS system exhibits larger errors in measuring latitude than longitude.

3.2.2 Dynamic error model

In the dynamic scenario described in Sec. 3.1.3.2, a reliable error model should account for error autocorrelation since according to [27] GPS errors feature relevant temporal and spatial autocorrelation. Physical sources of autocorrelation involved are signal multipath, shadowing, or second-order physical phenomena [35]. For this reason, simply modeling GPS error with a Gaussian process by adding a noise term to the true position is not realistic. The authors in [26] present different error models for uncertainties in GPS position measurements. To determine which one is the best they propose using the Akaike information criterion which uses maximum likelihood estimation to establish the likelihood of a set of parameters, and penalises the the number of adjustable parameters to safeguard against over-determining solutions. For a statistical model of the GPS positioning error process, with k parameters, the Akaike information criterion [36] is given by:

$$A_k = 2k - \log(L) \tag{3.5}$$

where L is the maximum likelihood for the model given the processed data. The Akaike information criterion is based on information theory and provides a balance between how well the model fits the data and the number of parameters in the model, to guard from overfitting. According to Akaike information criteria, one of the error models suggested by [26] is the Onrstein-Uhlenbeck process. An Ornstein-Uhlenbeck process is a mean-reverting process that satisfies the stochastic differential equation:

$$dX_t = \theta(\mu - X_t)dt + \sigma dW_t \tag{3.6}$$

where θ, μ, and σ are real parameters of the process, with θ, $\sigma > 0$. W_t is the fluctuation part, with $W_t \sim \mathcal{N}(0, t)$. The parameter θ is the speed of the mean reversion, telling how fast the process tends to its long-term average. μ is the long-term average value that the process tends to revert to, and σ is the volatility parameter, determining the magnitude of random fluctuations in the process. The Onrstein-Uhlenbeck process can be discretized through the Eurler-Maruyama approximation [37], to ease the implementation in the simulation software:

$$X_{n+1} = X_n + \theta(\mu - X_n)\Delta t + \sigma \Delta W_n \tag{3.7}$$

where Δt is the time increment and $\Delta W_n \sim \mathcal{N}(0, \Delta t)$.
Also in this case, model parameters are fitted according to GPS measurement dataset. The fitting procedure is described in the following section.

3.2.3 GPS error dataset and model fitting

As for the error variance tuning in the static analysis described in Sec. 3.2.1, the Ornistein-Uhlenbeck error model parameters needs to be fitted using GPS error measurements. Three different datasets are selected so that the effect in GPS error of three different urban densities can be evaluated. Dataset 1 was collected from [38] while traveling on the Bayshore Freeway, a highway route along the eastern shore of the San Francisco Bay Area in California, United States. Since it is mainly an open area, we expect relatively low GPS errors due to the rare multipath signal receptions. Dataset 2 was collected from [39] in Frankfurt am Main in Germany in the streets surrounding the Main Tower. This is an urbanized area given the presence of high buildings and skyscrapers. Dataset 3 was collected from [40] in a deeply urbanized area of Hong Kong, China. A summary description of the three datasets is presented in Tab.3.3.

	Reference	**Area**	**Urbanization**
Dataset 1	[38]	San Francisco bay	Open Area
Dataset 2	[39]	Frankfurt	Urbinazied
Dataset 3	[40]	Hong Kong	Deeply urbanized

TABLE 3.3: GPS error datasets considered in the simulation.

The Onsterin-Uhlenbeck model parameters have then been fitted to each one of the three datasets. In each case, the fitting strategy consists in fitting the model to the first 5 minutes of the GPS error measurements, in order to obtain the model for a 5 minutes walk. In Fig.3.9 are shown the geographic location in which measurements were collected for the three datasets in the 5 minutes path scenario. In particular, in Fig.3.9a San Francisco path is shown from a top view, and in Fig,3.9b we can see a street view frame thanks to which we can verify that this is an area unobstructed by buildings. In Fig.3.9d we can notice that Frankfurt path goes through very narrow urban canyons. In Fig.3.9f we can observe that Honk Kong path passes near several tall buildings but which are relatively far from the road. We can therefore expect that the model fitted for Frankfurt generates more impactful errors than the one fitted for Hong Kong.

The quality of the fit is assessed by visually checking the similarity between the single realization of the process and the measured dataset error in the same plot. Process realization and measurement need to be similar in terms of noise and spread around the average value given by the parameter μ. An example of what is considered good fit is shown in Fig.3.10.

Fig.3.10 shows that the fitting strategy does not consist in accounting for the isolated large error events in the measurements in order not to overfit the data. In fact, that event may be due to a specific environment characteristic, the crossing of a narrow

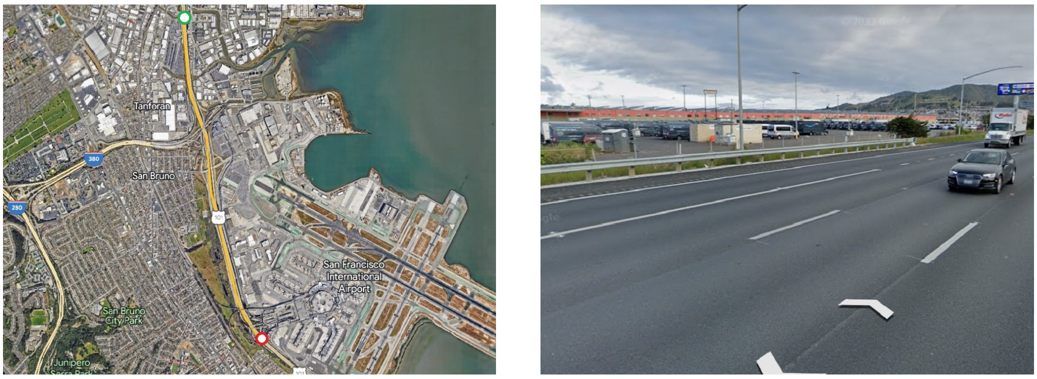

(A) San Francisco top view. (B) San Francisco street view.

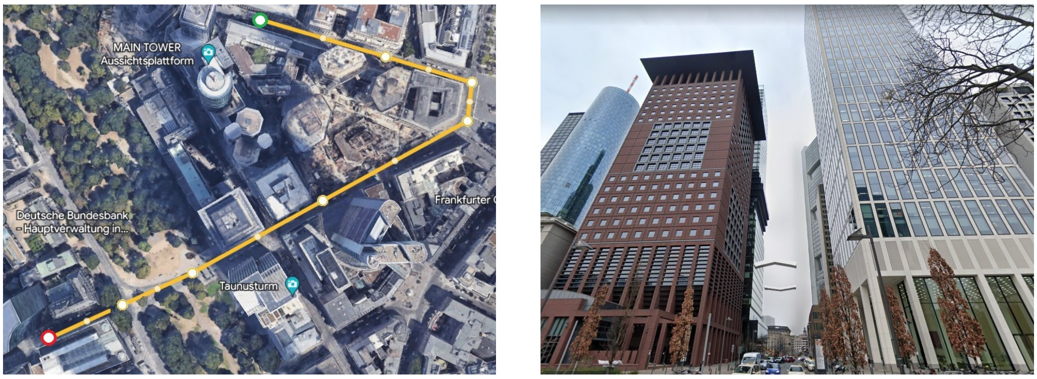

(C) Frankfurt top view. (D) Frankfurt street view.

(E) Hong Kong top view. (F) Hong Kong street view.

FIGURE 3.9: 5 minutes paths top and street views for the three datasets in Tab. 3.3.In the top views, the green dot indicates the starting point, the red one the ending point.

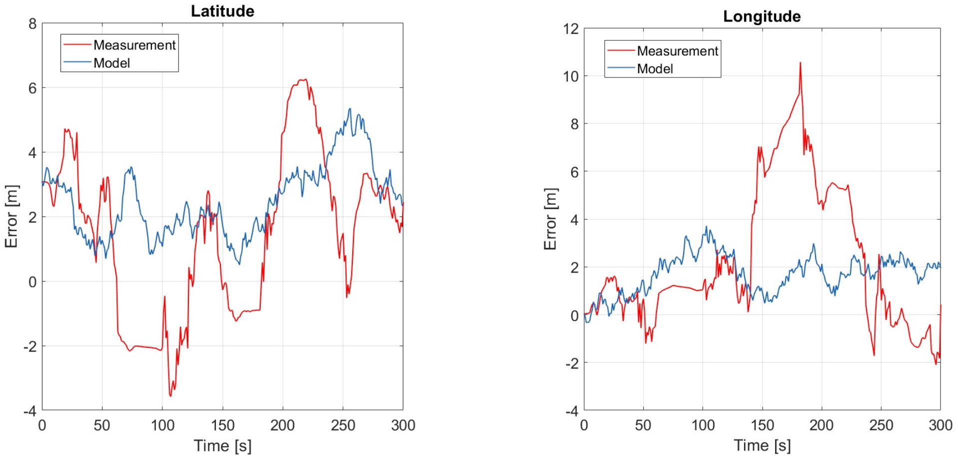

(A) TX beam IDs

(B) caption 2

FIGURE 3.10: Latitude and longitude measurement error (red) and single realization of Ornstein-Uhlenbeck error process (blue) for the 5 minutes walk in Hong Kong.

urban canyon for instance. The fitting procedure was further simplified by the fact that the measurement rate for the three datasets is 1 measurement per second. For this reason, the first 300 measurements were considered for the 5 minutes walk fitting. In Tab.3.4 and Tab.3.5 the selected Ornistein-Uhlenbeck fitted parameters are reported respectively for latitude and longitude GPS error.

	θ	μ	γ
San Francisco	5	0.8	2.4
Frankfurt	6	8.1	8.6
Hong Kong	6.2	1.5	3.8

TABLE 3.4: Ornstein-Uhlenbeck fitted parameters for the 5 minutes walk for latitude GPS error.

	θ	μ	γ
San Francisco	5.1	-0.3	2.1
Frankfurt	4	-1.7	4
Hong Kong	3.9	2.4	4.2

TABLE 3.5: Ornstein-Uhlenbeck fitted parameters for the 5 minutes walk for longitude GPS error.

As anticipated in Sec. 3.2.2, the main reason to use a correlated error model like the Ornstein-Uhlenbeck model is to incorporate GPS error autocorrelation. The autocorrelation in the model should be considered as a spatio-temporal autocorrelation since GPS measurements were collected in successive time instants while moving in the environment. To further investigate the quality of the fitting, autocorrelation curves

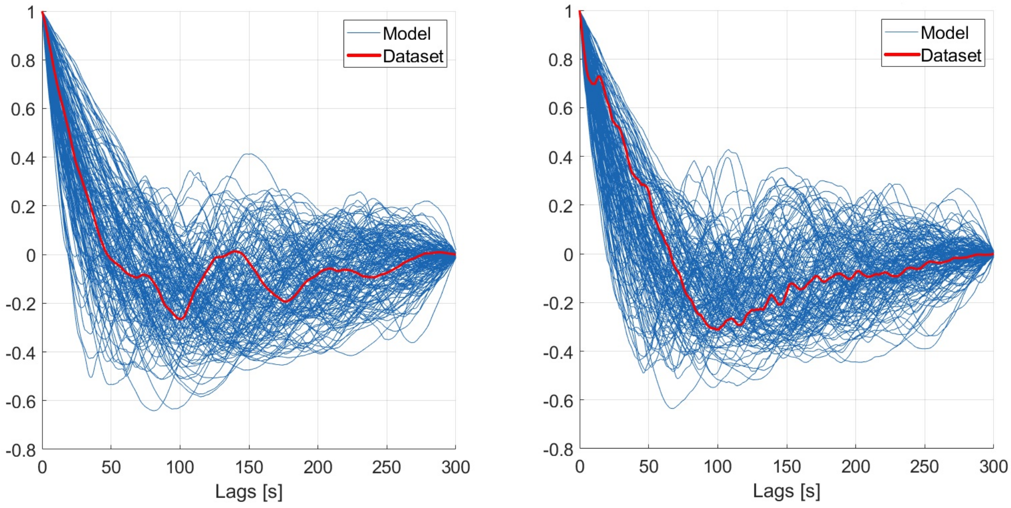

(A) Latitude

(B) Longitude

FIGURE 3.11: Measurement and model autocorrelation curves for the 5 minutes walk in San Francisco.

must be considered. Visual comparisons between the dataset autocorrelation and 150 realization of model autocorrelation are shown in Fig.3.11, 3.12, 3.13 for the 5 minutes walk.

By looking at the measurement autocorrelation plots, we can notice that they reach zero for the first time in about 50 seconds. The exception to this trend is represented by the 5 minutes walk in Frankfurt shown in Fig. 3.12, in fact latitude plots reaches the zero in about 75 seconds. Some of the plots present subsequent autocorrelation peaks, this particularly applies to the 5 minutes walk longitude plot in Frankfurt shown in Fig.3.12b after around 225 seconds. We can also notice that the measurement autocorrelation is always between the maximum and minimum Ornstein-Uhlenbeck realization for each lag in the plot for all the datasets and walks considered, except for the 5 minutes walk in Frankfurt for the longitude shown in Fig 3.12b. In this last case, the Ornstein-Uhlenbeck model is not able to track for the last autocorrelation peak. This occurrence is rare enough to also consider the parameters for the third dataset a good fit.

3.3 SIMULATION WORKFLOW AND PERFORMANCE METRICS

In this section, the detailed analysis regarding the general simulation procedure is presented and motivated in Sec. 3.3.1. Subsequently, all performance metrics for evaluating simulation output are listed and explained in Sec. 3.3.2.

3.3.1 *Simulation workflow*

The analysis is performed following the workflow shown in Fig.3.14. The input is the ray tracing REM described in Sec. 3.1.2, and one of the GPS location error models

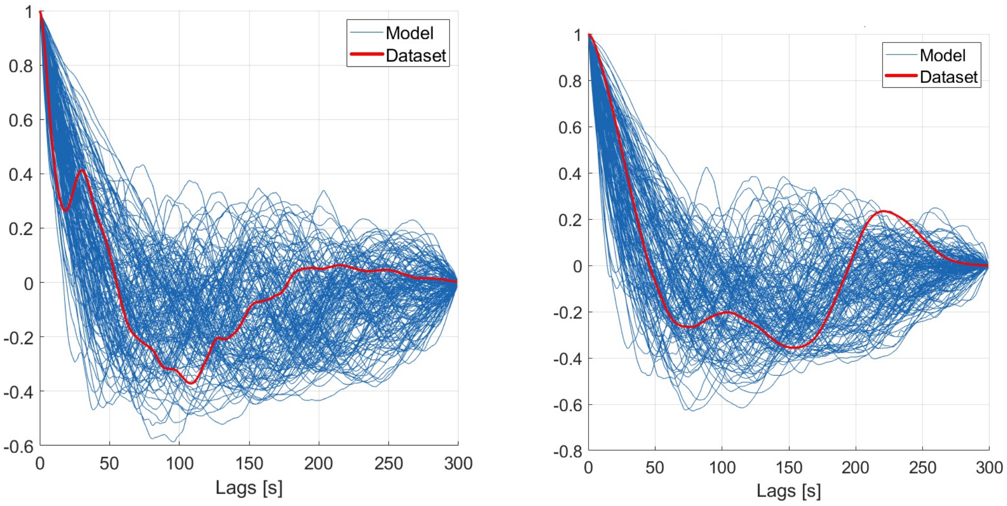

(A) Latitude (B) Longitude

FIGURE 3.12: Measurement and model autocorrelation curves for the 5 minutes walk in Frankfurt.

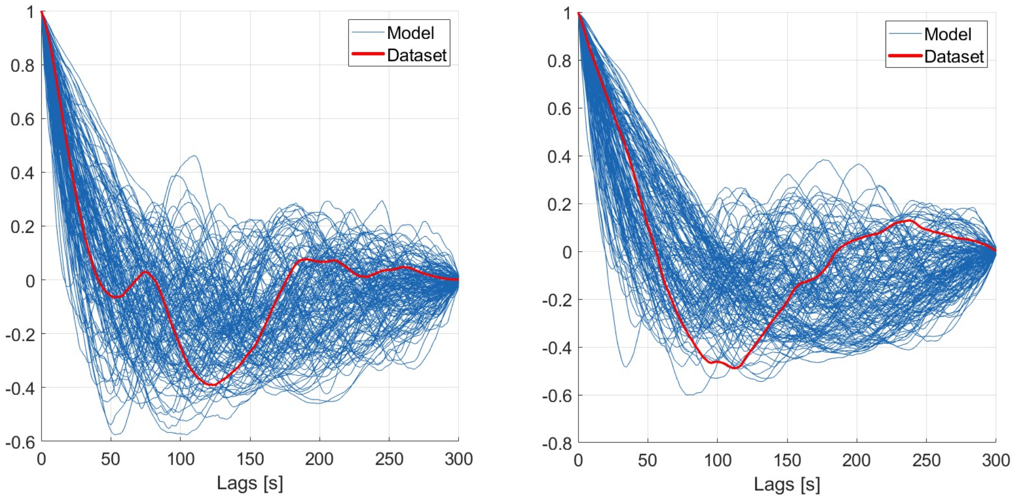

(A) Latitude (B) Longitude

FIGURE 3.13: Measurement and model autocorrelation curves for the 5 minutes walk in Hong Kong.

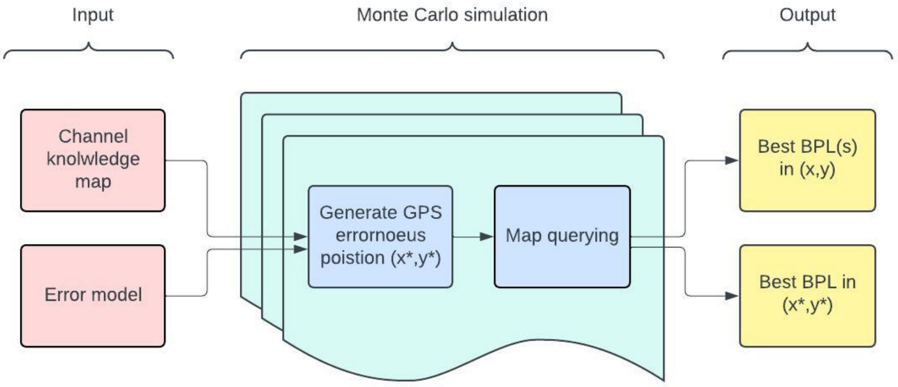

FIGURE 3.14: Explanatory workflow.

described Sec. 3.2.1 and Sec. 3.2.2. A randomly selected true RX position is generated in the map (x, y), from which an erroneous position (x^*, y^*) is generated using the error model. After that, the REM is queried in order to obtain the optimal BPL in the true position, i.e., maximum RSS of the BPL matrix in position (x, y). The sub optimal BPL is generated as in the scheme in Fig.3.15. The best BPL is searched for the erroneous position (x^*, y^*) and the correspondent TX and RX beam IDs are saved. Subsequently the true position (x, y) BPL matrix is queried for the same beam IDs. The sub optimal behavior is given to the fact that the best BPL is searched in a wrong UE location, so the actual exploited BPL is not necessarily the best. The optimal and sub optimal position generation and the consequent matrix querying steps are repeated n times in a Monte Carlo simulation with $n = 10000$ to obtain a distribution for the optimal and sub optimal performances. Thanks to the comparison we can evaluate an overall performance degradation due to GPS errors.

3.3.2 *Performance metrics*

The comparison between the optimal and sub optimal behavior is carried out through the following evaluation metrics:

1. **RSS and RSS difference**

   In most of the simulations, the relation is evaluated simply by considering the optimal and sub optimal distribution in terms of RSS expressed in dBm or at the distribution of the difference between them. This is the most immediate approach since the REM directly provides RSS values.

2. **Bit-rate and bit-rate difference**

   A similar distribution evaluation can be conducted in terms of bit rate to better visualize the link performance. Through the following data rate model [41], the

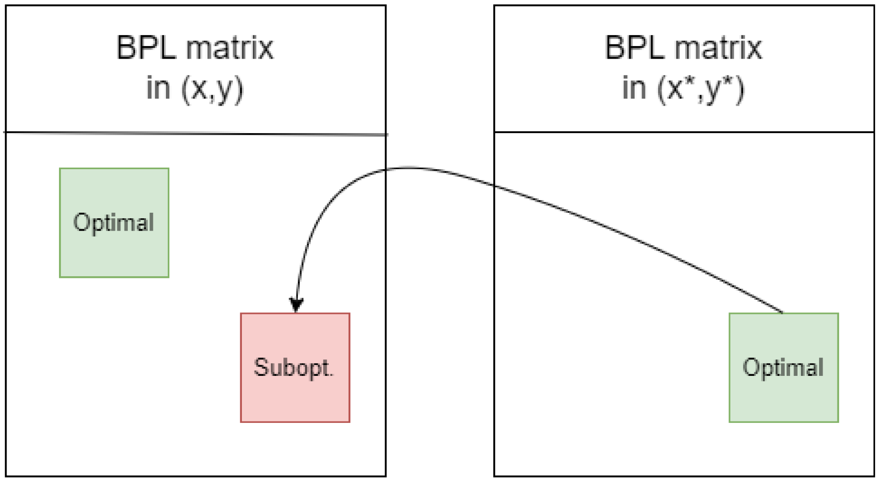

FIGURE 3.15: Sub optimal BPL generation scheme.

general BPL $RSS_{i,j}$ value can be mapped to the corresponding data rate. First, $RSS_{i,j}$ is converted to signal to noise ratio (SNR) using:

$$SNR_{i,j} = RSS_{i,j} - N \tag{3.8}$$

where N denotes the noise power in dBm and it is given by:

$$N = N_0 + N_F = 10\log(kTW) + N_F \tag{3.9}$$

Where k is the Boltzmann constant, T is the temperature in Kelvin (room temperature of approximately $290K$ is considered), and W is the considered bandwidth of $400MHz$. N_F is the considered noise figure at the RX. Overall, we have that the total noise contribution is $N = -78dBm$.

To map $SNR_{i,j}$ to the estimated achievable data rate $R_{i,j}$, the attenuated truncated Shannon bound is used:

$$R_{i,j} = \begin{cases} 0 \text{ Gbps}, & \text{if } SNR_{i,j} \leq SNR_{min} \\ 2 \text{ Gbps}, & \text{if } SNR_{i,j} > SNR_{max} \\ \alpha W \log_2(1 + SNR_{i,j}) \text{ Gbps} & \text{otherwise,} \end{cases} \tag{3.10}$$

where $\alpha = 0.75$ is the factor for implementation losses, $SNR_{min} = -5\text{dB}$ and $SNR_{max} = 20.5\text{dB}$. The transmission bandwidth is $W = 400\text{MHz}$.

3. **Beam ID matching fraction**

   Aside from optimal/sub optimal BPL evaluation, the n-best BPLs in the true position (x, y) can be considered and memorized. From those BPLs we can extract the n-best TX and RX beam IDs for the true position (x, y). Let $tx_{\text{best}} = [tx_1, tx_2, ..., tx_n]$ be the set of the n-best TX beam IDs for position (x, y), and $rx_{\text{best}} = [rx_1, rx_2, ..., rx_n]$ be the set of the n-best RX beam IDs for the same position. Instead, tx_1^* and rx_1^* are respectively the best TX and RX beam IDs in the erroneous position (x^*, y^*). The evaluation consists in checking for the matching percentage of tx_1^* in tx_{best} set and of rx_1^* in rx_{best} set after Monte Carlo simulation. This performance metric is relevant because we can infer regard the optimal number of TX and RX beam IDs that should be memorized and explored in a search. In fact, if by enlarging the number of beam IDs n checked we do not notice a significant matching percentage enlargement, it means that it is not necessary to carry out an exhaustive search but there can be considered in only n BPLs entries.

4

SIMULATION RESULTS AND ANALYSIS

4.1 SIMULATION RESULTS

In this chapter, the results of the various simulation scenarios outlined in Sec. 3.1.3 are presented and analyzed. In particular, results for the static scenario described in Sec. 3.1.3.1 are presented and commented in Sec. 4.1.1. Results for the dynamic scenario described in Sec. 3.1.3.2 are analyzed in Sec. 4.1.2 for the three mobility paths considered in the network area.

4.1.1 Static Scenario

First, the result of simulation of the static scenario described in Sec. 3.1.3.1 are presented, which involves the static error model described in Sec. 3.2.1 for performance degradation evaluation. The simulation workflow follows the description in Sec. 3.3.1. Simulation outputs are assessed using the performance metrics discussed in Sec. 3.3.2.

The reminder of this section is organized as follows. The impact of the erroneously reported UE location while querying the REM is assessed in Sec. 4.1.1.1 in terms of RSS and bit-rate degradation. In Sec. 4.1.1.2 similar considerations are carried out including an additional degradation factor in building the REM.

4.1.1.1 Effect of localization error while querying the REM

The results for normal distributed static error model having variance set in Tab.3.2 are analyzed first. Fig.4.1 presents optimal (i.e. the error-free one) and sub optimal RSS distributions measured in dBm over the positions in the REM with two different graphic formats. Fig.4.1a shows the optimal and sub optimal RSS distributions in the form of box-plots. In particular, optimal distribution is the leftmost one and, the sub optimal ones are on its right following an increasing order of error variance in Tab.3.2. On each box, the central red mark indicates the median, and the bottom and top edges of the blue box indicate the 25th and 75th percentiles, respectively. The whiskers extend to the most extreme data points not considered outliers, and the outliers are plotted individually using the red '+' marker symbol. Moreover, black and green horizontal thresholds indicate the lower and upper RSS values, respectively, for which the data rate mapping function in Eq.3.10 saturates at the lowest and highest values.

As we can see from Fig.4.1a, the medians of the distributions follow a decreasing trend as an error with higher variance is applied. The same trend is followed by the 25th percentiles, in detail it drops to the minimum RSS value for the box-plot corresponding to $VarSet = 5$, meaning that at least $\%25$ of UEs experience BPL failure. The difference is less evident for the 75th percentiles that are always over

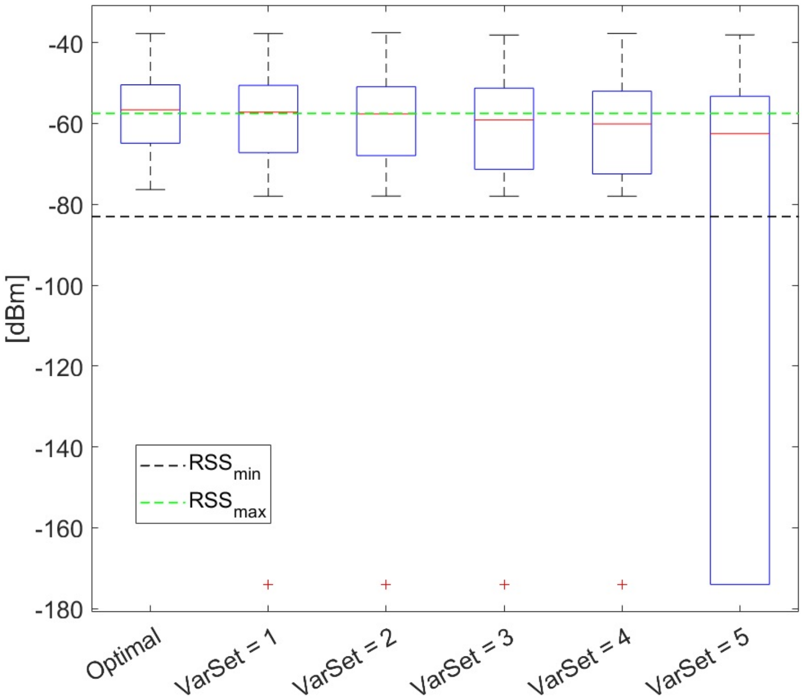

(A) caption 1

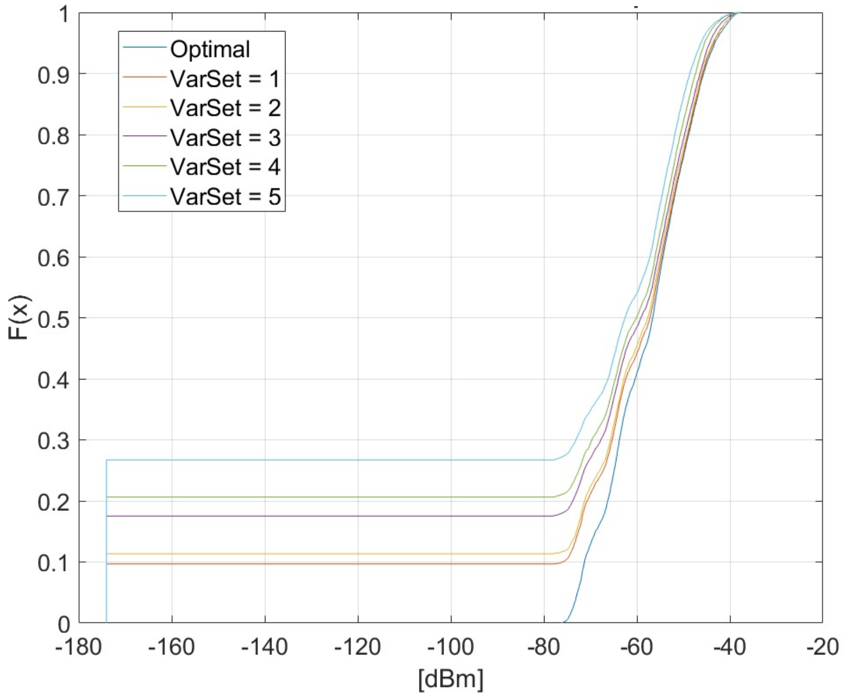

(B) caption 2

FIGURE 4.1: Optimal and sub optimal RSS comparison using normal distributed static error GPS model for variance values in Tab.3.2.

the upper rate threshold. All the sub optimal distributions show some outliers in the minimum RSS region, these are BPL failure events and they are further analyzed through the plots in Fig.4.3. Fig.4.1b is showing the same distributions in the form of cumulative distribution function (cdf). As we can notice, each cdf graph is always above the one having immediately lower variance set. Additionally, In this modality is possible to recognize the amount of BPL failure events for each distribution. These events correspond to RSS values equal to -174 dBm. They are about 10% of the total for $VarSet = 1$ and $VarSet = 2$, about 20% for $VarSet = 3$ and $VarSet = 4$, and about 27% for $VarSet = 5$.

To better visualize the link performance, Fig.4.1 shows optimal and sub optimal bit-rate distributions measured in Mbps over the positions in the REM with the same two graphic formats. The evaluation was done for the same GPS error variance sets as Fig4.1, thus taken from Tab.3.2. The RSS to bit-rate mapping procedure is described in Sec. 3.3.2. In Fig.4.2a shows optimal and sub optimal distributions in the form of box plots, where the optimal is the leftmost one and on its right we can find the sub optimal ones for increasing GPS error variance. We can notice that distributions for $VarSet = 1$ and $VarSet = 2$ are not far from the optimal in terms of median values. In particular, $VarSet = 1$ and $VarSet = 2$ have median reaching the value of 2000Mbps that is the maximum allowed from the link. Moreover, the 25th percentiles are over 1000Mit/s for those two sub optimal distributions. From $VarSet = 3$ on, the performances are evidently starting to deteriorate, in fact median values become more and more distant from 2000Mbps. Distribution correspondent to $VarSet = 5$ as expected provides the worst results, and it is the most spread in the bit-rate range with its 25th percentile equal to 0Mbps and $75th$ one equal to 2000Mbps. In Fig.4.2b we can visualize the same distributions through cdf plots. The plots shows that BPL failure events outlined by RSS cdfs in Fig.4.1b are mapped to 0Mbps events. Fig.4.2b also confirms that $VarSet = 1$ and $VarSet = 2$ provide similar results since the correspondent cdf plots are almost overlapping. The graph also provides information regarding the fraction of UE who experience the maximum bit rate for the error-free scenario and the five GPS error scenarios. Around 55% of UEs reach the maximum bit-rate in the error-free scenario, the worst performer is as expected $VarSet = 5$ with slightly more than 40% of UEs reaching it.

BPL failure events experienced in the simulation can be distinguished in two different roots. The first one is the complete link misalignment given by the GPS error. The other cause is that the error affected location reported to the TX is a location where data are not available. These are either locations occupied by the building considered by the ray-tracing building model or locations outside the network grid. Obviously, this second cause of BPL failure is to be considered less serious than the first, since it can be obviated by procuring a more complete and richer dataset. However, such achievement is costly in many realistic scenarios. In Fig.4.3 BPL failure event fractions are plotted for normal distributed GPS having error variance sets in Tab.3.2. Additionally, in Fig.4.3 BPL failure events are distinguished into those caused by lost signal and those caused by unavailability of data. We can notice that signal lost fraction increases approximately linearly with the error variance set considered. BPL failure events caused by non-availability of data increase more quickly, meaning that one limitation of the simulation is the lack of available data in the REM and this becomes more relevant in large GPS error scenario.

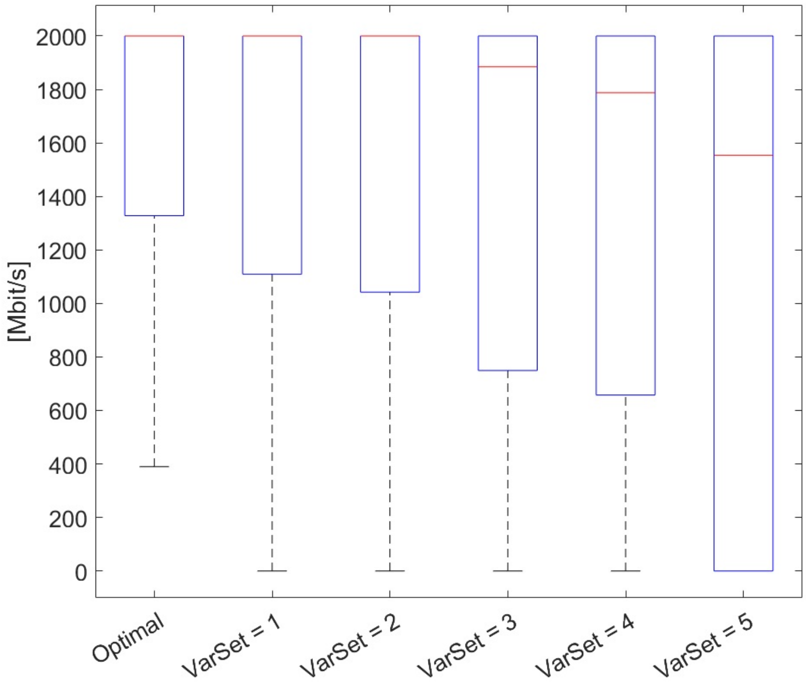

(A) Box-plot bit-rate comparison.

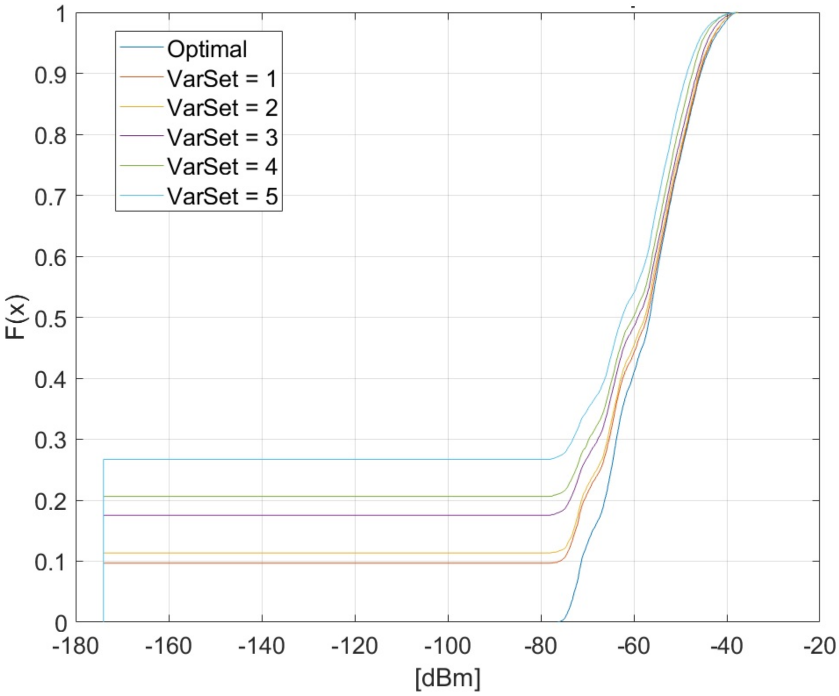

(B) cdf bit-rate comparison.

FIGURE 4.2: Optimal and sub optimal bit-rate comparison using normal distributed static error GPS model for variance values in Tab.3.2.

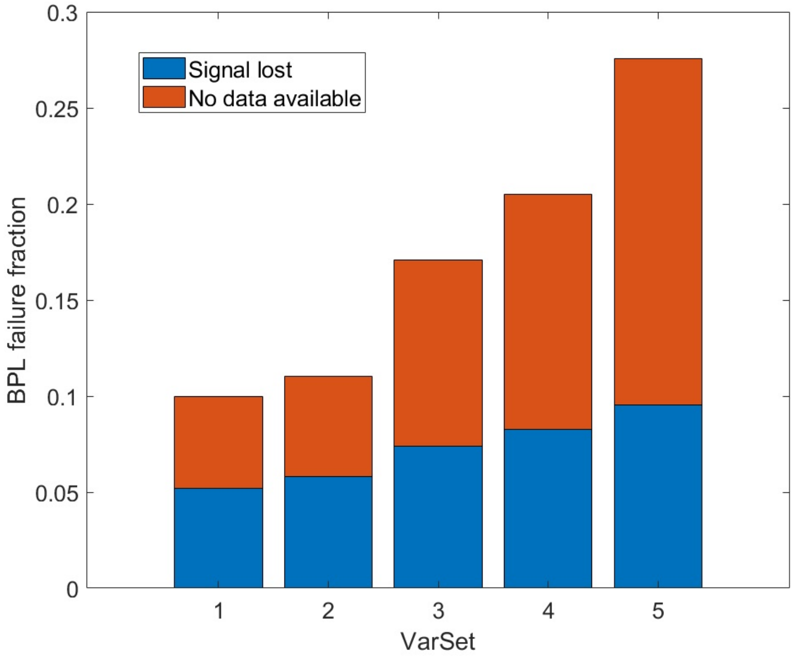

FIGURE 4.3: BPL failure events fraction normal distributed GPS error for error variances in Tab3.2. BPL failure events are distinguished into those caused by lost signal and those caused by unavailability of data.

The purpose of the following analysis is to highlight the effect of using the logistic distribution instead of the normal distribution for modeling static GPS error. Therefore, Fig.4.4 present optimal and sub optimal bit-rate distributions for normal distributed GPS error (red) and logistic distributed GPS error (blue). The error shape comparison is made fair by the fact that normal and logistic distributions have the same input variance for the same error variance set (error variance sets in Tab.3.2). Thus, the diversity between the two error models lies in the distribution shape, as outlined in Sec. 3.2.1. We can notice a difference in the median values for the boxes correspondent to $VarSet = 3$, $VarSet = 4$, and $VarSet = 5$. For these error variance sets, logistic distribution median value is a larger bit rate value than the correspondent normal distribution median value. This can be explained by the fact that the logistic distribution pdf has faster growth at the mean value than the normal one having the same variance, this is visually confirmed by Fig.3.8 in Sec. 3.2.1. Since the mean value of the GPS error is the true UE position, we expect more values close to the true position for the logistic distributions leading to larger median values.

The analysis can be extended by considering the n best BPLs for the true UE position in the comparison instead of only the best one. In Fig.4.5 box-plot bit-rate distributions for the 5-best BPLs in the true UE position (green) are shown. To their right, sub optimal bit-rate distribution box-plots for normal (blue) and logistic (red) GPS error introduced in Fig.4.4 are reported again for comparison purposes. As can be seen, bit-rate results for $BestBPL1$ and $BestBPL2$ are better than any result obtained by

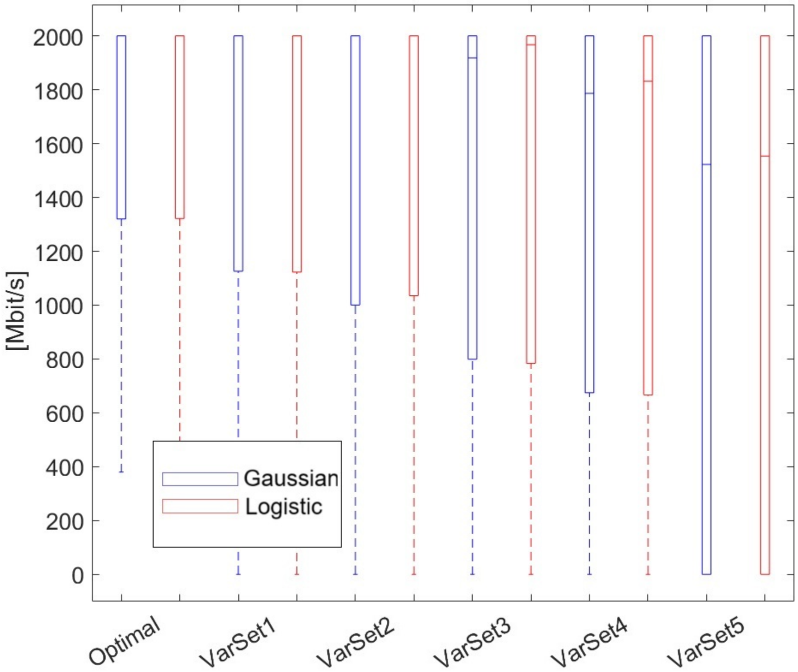

FIGURE 4.4: Optimal and sub optimal bit-rate comparison using normal distributed GPS error (blue) and logistic distributed GPS error (blue).

applying GPS error with variance set in Tab.3.2. Instead, it can be noted that the performance achieved introducing GPS error for $VarSet = 1$ is comparable with the one obtained by $BestBPL3$ for the true GPS location in terms of 25th and 75th percentiles. Similar consideration can be made for $BestBPL4$ and $VarSet = 2$. Differently, $VarSet = 3$ and $VarSet = 4$ achieve worse performances than $BestBPL5$ in terms of 25th percentile but better in terms of median value. Instead, $VarSet = 5$ provides the worst result from every point of view.

To further investigate in the comparison, Fig.4.6 presents the cdf bit-rate distribution comparison between the performance achieved using the 5-best BPLs for the true UE position and the ones achieved by including normally distributed GPS error with error variance sets in Tab.3.2. Fig.4.6a presents the comparison for $VarSet = 1$. It can be seen that $VarSet1$ distributes a larger number of UEs than all error-free 5-best BPLs in the low bit-rate half between 0Mbps and 1000Mbps, then it distributes a similar number of UEs than $BestBPL3$ in the high bit-rate half between 1000Mbps and 2000Mbps. Lastly, $VarSet = 1$ assigns the maximum bit-rate of 2000Mbps to more UEs than $BestBPL3$, $BestBPL4$, $BestBPL5$, and less than $BestBPL1$ and $BestBPL2$. Fig.4.6b shows that $VarSet = 2$ provides the worst results in the in the low bit-rate half, and similar results to $BestBPL3$ in the high bit-rate half. This confirms that $VarSet = 2$ gives only slightly worse outcomes than $VarSet = 1$. Performance for $VarSet = 3$ can be evaluated in Fig.4.6c. It can be seen that $VarSet = 3$ in largely the worst in the low bit-rate half with as much as the 20% of the UEs experiencing no connection, and it behaves similarly to $BestBPL4$ in the high bit-rate half.

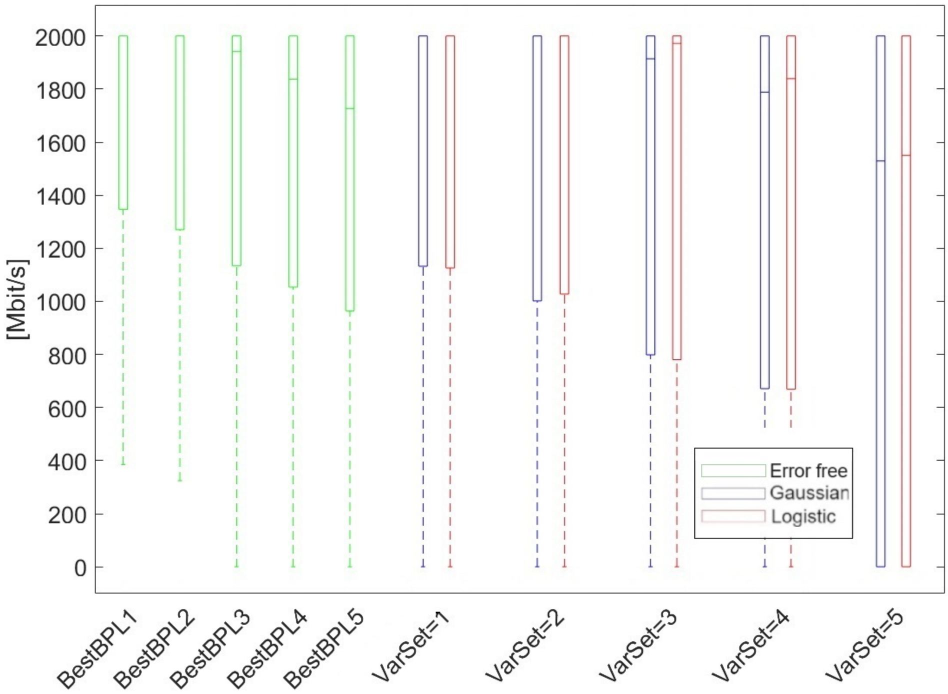

FIGURE 4.5: Bit-rate distribution for the 5-best BPLs in the true UE position (green) compared to sub optimal bit-rate distributions using variance sets in Tab.3.2, and normal (blue) or logistic (red) distributed GPS error.

The poor performances achieved by $VarSet = 4$ and $VarSet = 5$ can be evaluated respectively in Fig.4.6d and Fig.4.6e. Symptomatic of this truly negative result are the amount of UEs who experience 0Mbps bit-rate, these are slightly more than 20% for $VarSet = 4$, and almost 30% for $VarSet = 5$. Overall, the main difference between distributions for true UE position and the ones obtained by including GPS error, lies in the amount of UEs having a connection of 0Mbps. In fact, these are generally more if GPS error is included. This can be explained by the fact that the GPS error may cause a positioning report of data-less location to the BS. As outlined in Fig.4.3, this phenomenon is becoming increasingly common by enlarging GPS error variance.

Another interesting study that can be conducted by considering and memorizing the n-best BPLs for the true UE position is the one introduced in Sec. 3.3.2. From the n-best BPLs the n-best TX and RX beam ID sets can be extracted. The inspection consists in verifying that the best TX and RX beam IDs for the erroneous location are respectively within the n-best TX set and RX beam IDs set for the error-free location, and checking for the matching fraction after the Monte Carlo simulation. Fig.4.7 shows the result for TX and RX beam ID matching fraction as a function of TX and RX best ID sets numerosity. The simulation is performed by applying normally distributed GPS error having error variance sets in Tab3.2. Fig.4.7a presents the study results for $VarSet = 1$. It can be noticed that TX and RX beam ID matching curves grow by enlarging the number of beam considered in the set since it is more likely to have a match in a larger

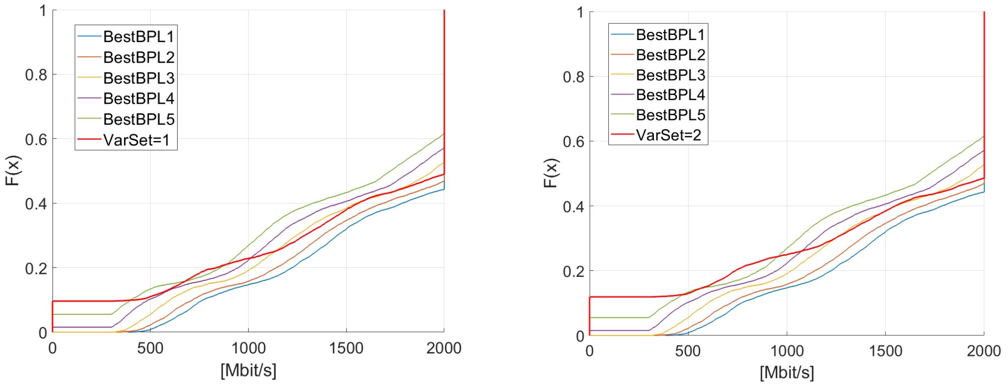

(A) $VarSet = 1$ and 5-best BPLs comparison.

(B) $VarSet = 2$ and 5-best BPLs comparison.

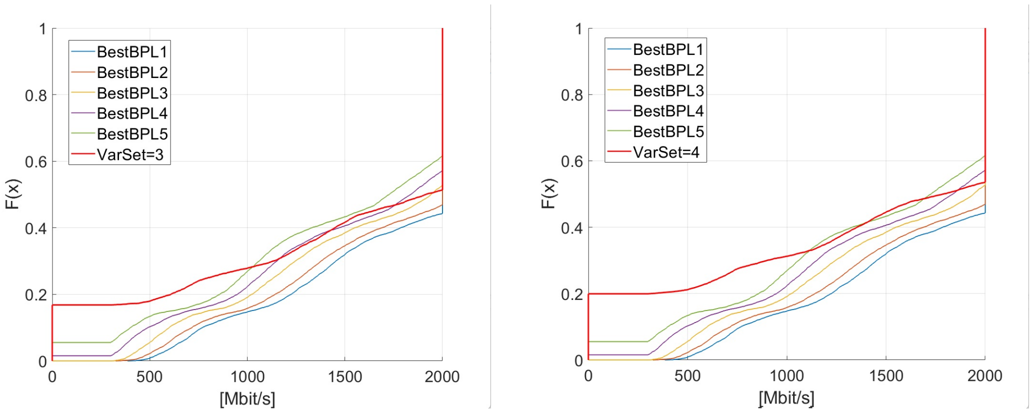

(C) $VarSet = 3$ and 5-best BPLs comparison.

(D) $VarSet = 4$ and 5-best BPLs comparison.

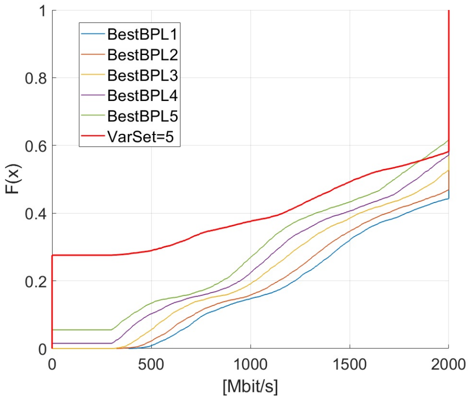

(E) $VarSet = 5$ and 5-best BPLs comparison.

FIGURE 4.6: cdf bit-rate comparison between error-free performance using the 5-best BPLs and sub optimal performances using variance sets in Tab.3.2 and normally distributed error.

set. Furthermore, RX beam ID matching curve is always above than TX one. This holds for every error variance set and is explained by the fact that the RX has only 16 IDs, unlike the TX which has 64 IDs making the potential match less likely for smaller sets. In Fig.4.7a RX best beam ID for the erroneous position is in 95% of the cases the same as error-free position best one. RX matching curve then grows very rapidly to very high matching fractions: that is about 97% for the size 2 set, and close to 100% for larger sets but remaining quite flat. Eventually, the graph reaches 100% of match if the beam ID search is done among the top 16 RX beam IDs. It could not be otherwise since the RX has available a total of 16 beams. TX matching curve for in Fig.4.7a starts with a percentage of 85% and then reaches flatness from set size 6 onward with a matching percentage of about 90%. As anticipated in Sec. 3.3.2, if the curve reaches the flatness from set size 6, it means that it is not necessary to carry out an exhaustive search but instead only the supposed 6 best TX beams should be considered and checked. In Fig.4.7b TX and RX beam ID matching plots are reported for $VarSet = 2$. RX matching curve is similar to the one for $VarSet = 1$ except for the set size 1 match, which drops to about 93%. TX matching curve provides worst results in particular for the match on small size sets. The largest difference. The biggest difference from $VarSet = 1$ TX matching curve is again for set size 1, which matching percentage is slightly more than 80%.
Expectantly, ID matching results are getting worse for $VarSet = 3$, as can be seen in Fig.4.7c. In particular, the match for the size 1 set drops precipitously to less than 90% for RX beam matching and less than 70% for TX beam matching. Moreover, it may be noted that both curves never exactly reach flatness as was the case for less impacting GPS errors. In fact, both of them keep growing in the matching percentage, meaning that it is probably less effective to focus in a limited number of IDs in the search. Fig.4.7d shows the same results for $VarSet = 4$. RX beam match drops to slightly more than 85% for set size 1, reaching a reliable matching percentage of 97% only from set size 4 on. The TX matching curve is getting for its entirety further distant from the RX one curve compared the graphs with less impacting GPS error. This means that having a greater amount of beam IDs in the codebook makes it even more difficult to match in large GPS error scenarios. Also relevant is the really poor TX ID match value for set size 1, that is around 65%. The worst results are the ones provided by $VarSet = 5$, as shown is Fig.4.7e. In this case, even RX beam ID match drops to around 80% for set size 1. RX beam match curve than grows to the reliable rate of 97% only for set size 10. This is really discouraging since it means that to be enough sure to find the best RX beam ID there is the need to check 10 beams out of 16, leading to small resource saving. The TX match plot for $VarSet = 5$ is for its entirety very unpromising. It starts from the extremely low value of 50%, and only grows to 90% for set size 16. Moreover, it never reaches a flat state, on the contrary, it is always evidently tilted and will probably maintain this state even for best beam ID sets larger than 16 in size.

Overall, results for static scenario strictly depend on the importance of GPS error. As a consequence, the results depend on the urban density where the GPS system is used, as the variance of the GPS error was adjusted according to real-world GPS

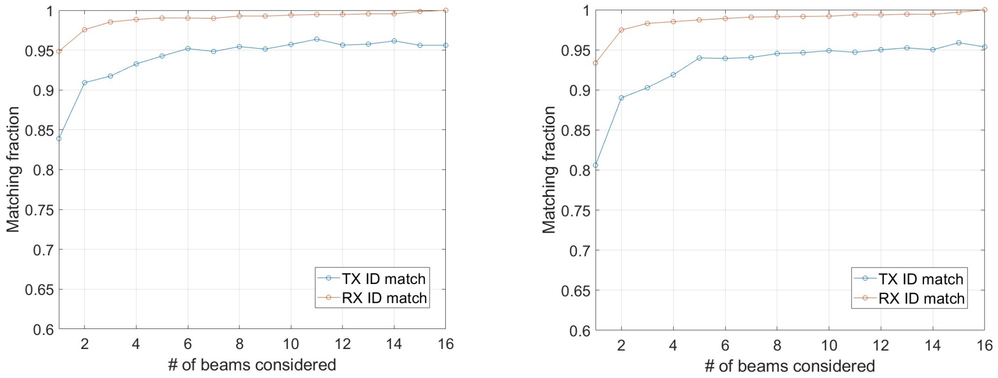

(A) Beam ID matching with $VarSet = 1$.

(B) Beam ID matching with $VarSet = 2$.

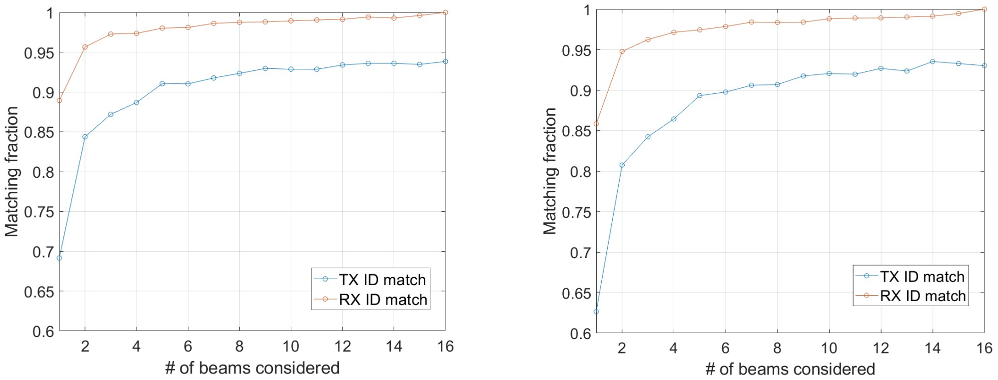

(C) Beam ID matching with $VarSet = 3$.

(D) Beam ID matching with $VarSet = 4$.

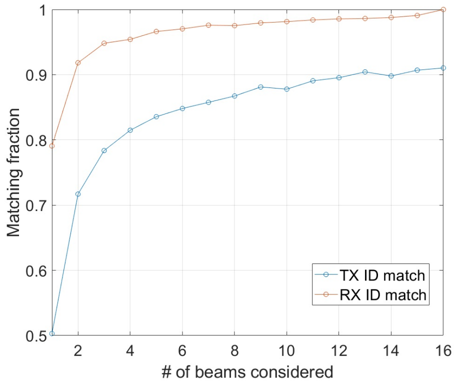

(E) Beam ID matching with $VarSet = 5$.

FIGURE 4.7: TX (blue) and RX (orange) beam ID matching respectively in the sets of the TX and RX best beam IDs as a function of the set numerosity. The evaluation is carried out for the 5 GPS error variance sets in Tab.3.2, and normally distributed error.

error measurements. In the next section, an additional realistic degradation factor is including to the simulation while constructing the REM.

4.1.1.2 Effect of localization error in constructing and querying the REM

In practical settings, the REM is constructed from measurements reported in different modalities. As a consequence, during the REM construction procedure the location information reported may not be associated with the correct position where the measurement was taken. It was decided that the REM is constructed from measurements communicated by UEs in the area. Since the location related to the communicated information is provided by GPS, it is reasonable to apply the same GPS error model as in the previous section for the REM construction. More precisely, the BPL matrix saved for a specific position may be saved in a wrong position generated according to a normal or logistic distribution having mean value in the true position and variance set in Tab.3.2. It could therefore be the case that the BPL matrix for one position is recognized instead for a neighboring one. The purpose of this section is to analyze the combined effect of the error in REM construction and the error in the subsequent querying.

In order to isolate the effect of the error in the map construction, Fig.4.8 shows the RSS degradation map resulting from the difference between the RSS value provided by the supposed best BPL in a position and the RSS value provided by the real best BPL for that position. White areas, on contrast, are where data are not available. In the example of Fig.4.8, the GPS error for the construction is featured with $VarSet = 3$ in Tab.3.2. In the same figure it can be seen that in most of the LoS positions, the loss is limited to a value around 10 dBm. This is different for positions very close to the TX where for some of them the loss is around 25 dBm and even around 100 dBm for extremely close positions. This can be explained by the fact that the best BPLs can change even between positions very close together given the proximity to the TX. For this reason, the BPL matrix switching effect given by the error is particularly decisive. Apart from this specific case, the largest losses are recorded in positions close to the transition between LoS and NLoS conditions. For these positions the losses are very high and are between 100 dBm and 120 dBm. This happens because LoS and NLoS neighboring locations are likely to be reached by different main propagation paths. If this is the case, these positions are probably going to have different best BPLs. Other relevant losses of around 80 dBm are visible in the form of stripes in LoS areas far from the TX. This phenomenon can be seen in the northeast, northwest, and south in the map in Fig.4.8. The explanation for this occurrence is to be related to an artifact of the simulator, so there is no physical reason behind it.

To evaluate the compound effect of the error in the REM construction and the one in the subsequent querying, the following approach is followed. An erroneously built REM is generated for each error variance set in Tab.3.2 and, in each case the variance set decides the impact of the GPS error in the REM generation. The procedure thus results in 5 different erroneously built REMs. Next, in the REM query is applied the

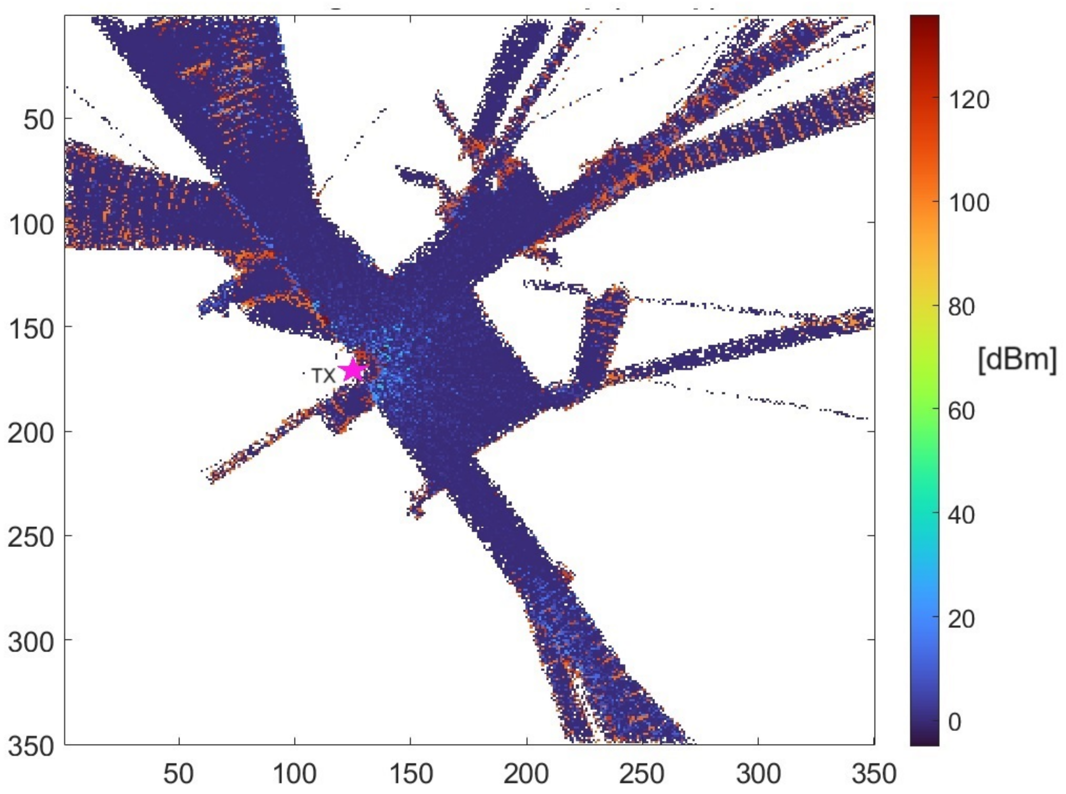

FIGURE 4.8: RSS degradation map in the study area once applied normally distributed GPS with error with $VarSet = 3$ in the map construction procedure. The TX position is highlighted with the pink star.

same GPS error used in the generation, having then the same normal distribution and the same variance set. The reasoning behind the choice made is motivated by the fact that the accuracy of the GPS system depends mainly on the urban characteristics (urban density, multipath opportunities, etc.) in which it operates and not on its specific use. Thus, the idea is that the urban characteristics are the same both for map construction and querying. Fig.4.9 presents the results of RSS distributions measured in dBm over the positions in the REM in the box-plot and cdf graphic formats. In Fig.4.9a the comparison is carried out in terms of box-plots. Optimal RSS distribution is plotted in the leftmost side as a reference. Sub optimal distributions are on its right following an increasing order of error variance set in Tab.3.2. The performances obtained with the true REM and the erroneous REM are overlapped for the same GPS error variance set in order to highlight the effect of using the erroneous REM. Specifically, the achieved RSS distributions obtained by using the true REM are plotted in blue and the ones achieved with the erroneous REM are plotted in red. Moreover, black and green horizontal thresholds indicate the lower and upper RSS values, respectively, for which the data rate mapping function in Eq.3.10 saturates at the lowest and the highest values.

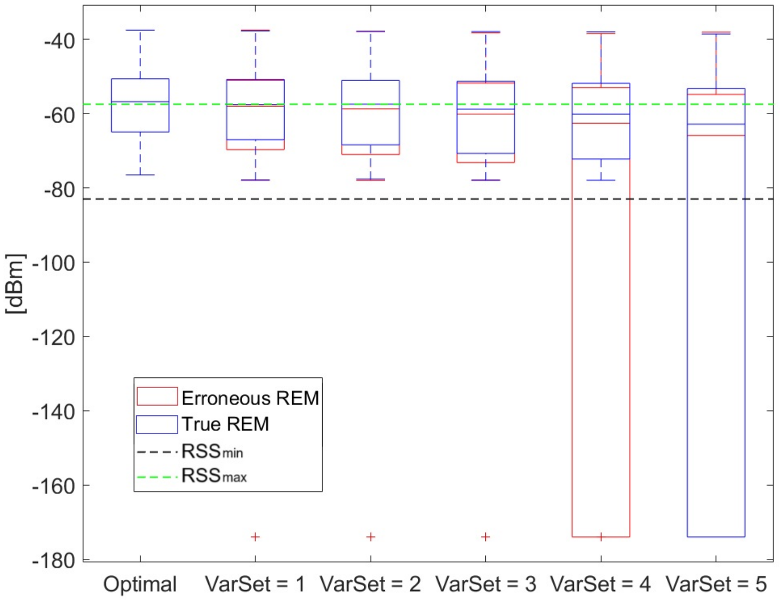

(A) Box-plot RSS comparison.

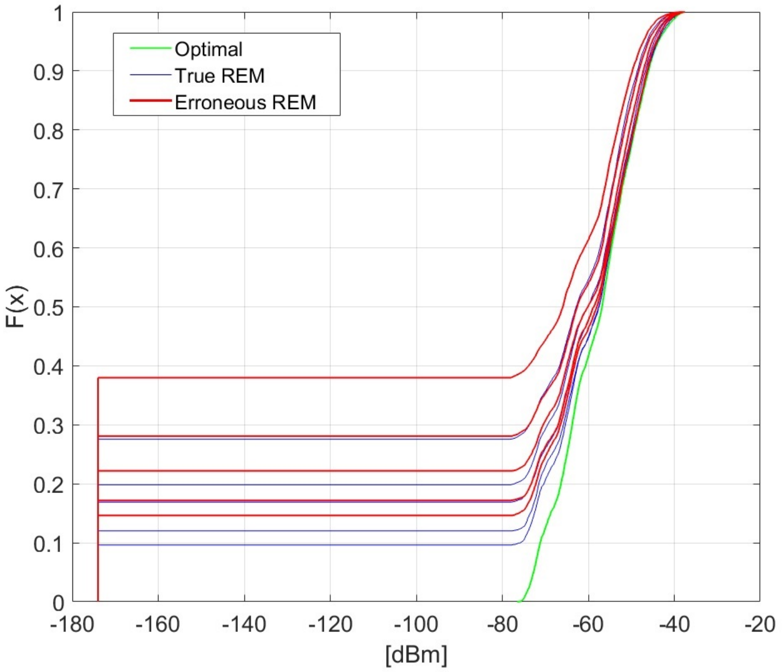

(B) cdf RSS comparison.

FIGURE 4.9: Sub optimal RSS distribution comparison for correct REM (blue) and erroneous REM (red). GPS errors in the map construction and in the subsequent querying are both normally distributed having variance set in Tab.3.2.

As it can be seen from Fig.4.9a, the differences between the two performances for the same variance set are in general evident in the median values and in the 25th percentiles. Distributions for $VarSet = 1$ are mainly differentiated by the 25th percentile, which differ in about 2 dBm. In contrast, the box-plots for $VarSet = 2$ differ both in the median value and in the 25th percentile. The difference in the 25th percentile slightly increases to about 3 dbm. $VarSet = 3$ distributions differ slightly in the 75th percentile as well as the median value and the 25th percentile. The largest difference in performance is visible for $VarSet = 4$. The two distributions differ in the 75th percentile by about 1 dBm, in the median value by about 3 dBm, but especially in the 25th percentile as the 25th percentile obtained with the erroneous REM drops to value of lost connection (i.e., the value of -174 dBm). Lastly, the distributions for $VarSet = 5$ achieve the largest difference in the 75th percentile of about 2 dBm, and the largest difference il the median value of about 4 dBm. Fig.4.9b is showing the same RSS distribution results in the form of cdf. Both for distributions using the true REM and the ones using the erroneous REMs, each graph line is always above the one having immediately lower variance set. For this reason, all curves obtained with the true REM were plotted with the same color (blue), as were those obtained with the wrong REM (red). Lastly, the curve indicating the optimal performance is plotted in green as reference. It may be seen that in general the amount of BPL failure events increases greatly as a result of the erroneous REM. For the erroneous map, BPL failure events are about the 15% for $VarSet = 1$, about the 18% for $VarSet = 2$, about the 22% for $VarSet = 3$, about the 28% for $VarSet = 4$, and even about the 39% for $VarSet = 5$. Thanks to cdf representation in Fig.4.9b, one can see the difference in BPL failure events between $VarSet = 4$ and $VarSet = 5$ that could not be appreciated at the same way with in the box-plot representation in Fig.4.1a.

To better visualize the link performance, Fig.4.10 shows bit-rate distribution results measured in Mbps using the true REM and erroneously built REM. The evaluation was done by applying GPS error in REM building and in the following querying as explained for Fig.4.9. The RSS to bit-rate mapping procedure is described in Sec. 3.3.2. In Fig.4.10a the comparison is carried out in terms of box-plots. Optimal bit-rate distribution is plotted in the leftmost side as a reference. Sub optimal distributions are on its right following an increasing order of variance set in Tab.3.2. Also in this case, the performances obtained with the true REM and the erroneous REM are overlapped for the same GPS error variance set in order to highlight the effect of using the erroneous REM. Specifically, the achieved bit-rate distributions obtained by using the true REM are plotted in blue, and the ones achieved with the erroneous REM are plotted in red. As it can be seen from Fig.4.10a, the difference between the two performances for the same variance set are in general evident in the median values and especially in the 25th percentiles. Distributions for $VarSet = 1$ differ only in the 25th percentile, which differ in more than 200Mbps. Distribution for $VarSet = 2$ differ by about 200Mbps in the 25th percentile but also by about 50Mbps in the median value which is below the maximum achievable bit-rate. Distributions for $VarSet = 3$ differ in the median value by about 100Mbps and in the 25th percentile by about 150Mbps. Distribution for $VarSet = 4$ differ by around 200Mbps in the median value, and even by more than 600Mbps in the 25th percentile. Lastly, distributions for $VarSet = 5$ differ by around

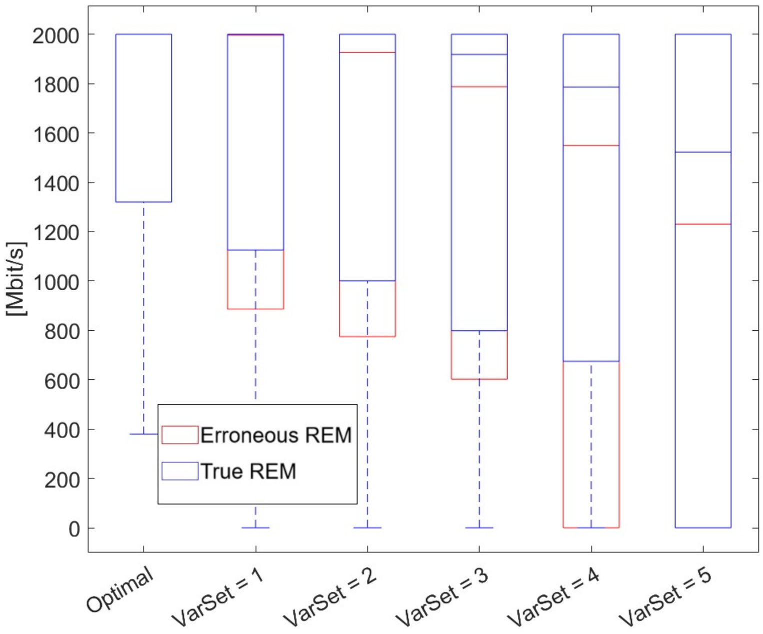

(A) Box-plot bit-rate comparison.

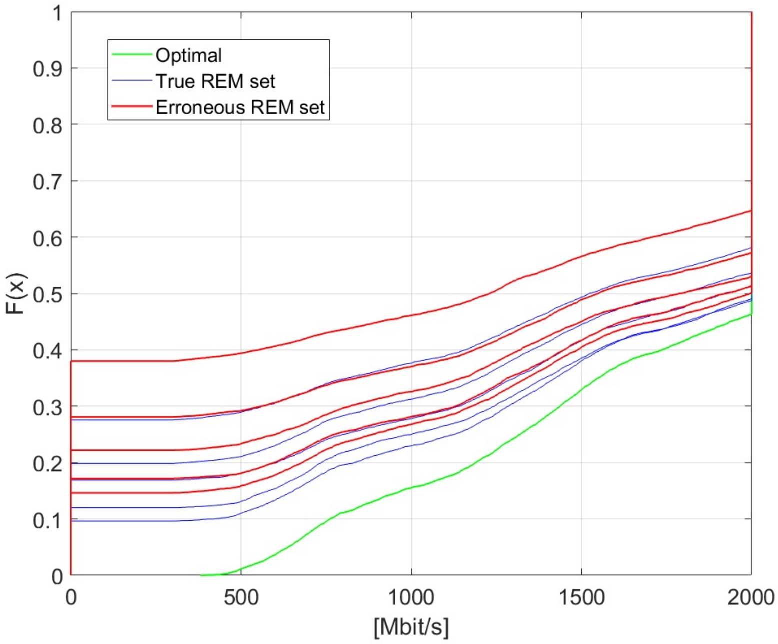

(B) cdf bit-rate comparison.

FIGURE 4.10: Sub optimal bit-rate distribution comparison for correct REM (blue) and erroneous REM (red). GPS errors in the map construction and in the subsequent querying are both normally distributed having variance set in Tab.3.2.

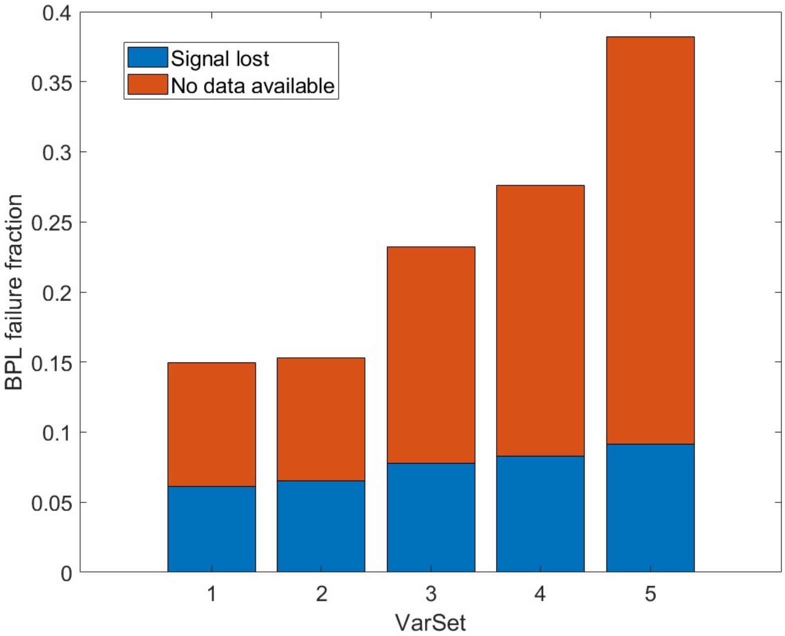

FIGURE 4.11: BPL failure events fraction by using erroneous REMs and for GPS error variance sets in Tab3.2. BPL failure events are distinguished into those caused by lost signal and those caused by unavailability of data.

300Mbps in the median value. Fig.4.10b is showing the same bit-rate distribution results in the form of cdf. The curves obtained with the true REM are plotted in blue, the ones obtained with the erroneous REMs are plotted in red. The curve indicating the optimal performance is plotted in green as a reference. As for Fig.4.9b, each cdf curve for is always above the one having immediately lower variance variance both for the group of lines obtained with the true REM and for the group of lines obtained with the erroneous REMs. It can be seen from Fig.4.10a that BPL failure events outlined by Fig.4.9b are mapped to 0Mbps events. For the erroneous REMs, these are around the 15% for $VarSet = 1$, around the 17% for $VarSet = 2$, around the 23% for $VarSet = 3$, around the 28% for $VarSet = 4$, and even around the 38% for $VarSet = 5$. Respect to the amount of BPL failure events obtained by using the true REM these are increased by 5% for $VarSet = 1$, $VarSet = 2$ and $VarSet = 3$, by 8% for $VarSet = 4$, and by 10% for $VarSet = 5$. Thus, it is evidenced that by increasing the weight of error in REM construction, the worsening in terms of BPL failure events increases accordingly. Fig.4.10b also provides information regarding the fraction of UEs who experience the maximum bit-rate in case of erroneously built REMs. These are around the 50% for $VarSet = 1$, $VarSet = 2$, and $VarSet = 3$, around the 44% for $VarSet = 4$, and around the 35% for $VarSet = 5$. The most evident deterioration respect to the true REM is given by $VarSet = 5$ in which the number of UEs experiencing the maximum bit-rate decreases by the 6%.

Fig.4.11 shows the amount of BPL failure events using erroneous REMs. BPL failure events are distinguished into those caused by lost signal (blue) and those caused by unavailability of data (orange). It can be noted that BPL failure events due to signal lost do not increase evidently due to the effect of the erroneous REMs. In fact, the difference respect to the same result shown in Fig.4.3 is minimal for all the error variance sets. The most important contribution is therefore the BPL failure events caused by unavailability of data. These increases respect to the true REM simulation of about 5% for $VarSet = 1$, $VarSet = 2$ and $VarSet = 3$, of about 8% for $VarSet = 4$, and more than the 10% for $VarSet = 5$. Overall, this most decisive cause of BPL failure events is to be considered less serious than the first, since it can be obviated by procuring a more complete and richer dataset.

For all the evaluations made so far in the section, the REM generated with a single sweep on the locations was used. This means that a single BPL information from a UE was collected and memorized for each position in the REM. The outcome of this operation is shown in Fig.4.8 and, as demonstrated in this section, using an REM constructed in this way results in a significant deterioration in performance. What could be done to limit this problem is to rely on not just a single measure for each position, but multiple. In this way, the network can look to different maps and make a decision regarding the best BPL based on a larger dataset. For example, the decision can be made based on the average information reported by multiple UEs for the same location.
Fig.4.12 shows the degradation map resulting from the positional average RSS loss on different REMs constructed. More specifically, for each position in the map, the average resulting from the RSS value provided by the best BPL according to multiple UE notifications was calculated. For all the REM constructions normally distributed GPS error is applied featured with $VarSet = 3$ in Tab.3.2. Fig.4.12a is providing the reference and showing the RSS degradation map for 1 notification sweep REM construction. The same figure also highlights the positions of greatest loss: those near the TX and those at the transition between the LoS and NLoS conditions. In Fig.4.12b it can be seen the RSS degradation map resulting from 5 REMs average. Similar losses to the 1 sweep scenario are obtained in the areas of very low losses. On the other hand, in the transition areas between LoS and NLoS conditions significant improvements are visible with RSS losses decresing to values in the range between 60 and 100 dBm. Similar improvements are achieved in the area close to the TX. In Fig.4.12c a further reduction in RSS losses in the transition zones between LoS and NLoS and in the areas close to the TX can be seen thanks to the 20 REMs average operation. In this case, the maximum losses are between the 60 and 80 dBm. In fact, positions where RSS losses of 90 dBm are reached are very rare and isolated. In contrast, the improvement between considering 20 REMs and considering 100 REMs in the average is almost negligible, as can be noted by comparing Fig.4.12c and Fig.4.12d. The small difference is visible for the positions close to the TX, in fact in the 100 REMs scenario the area of high losses is more restricted in space. There is practically no difference instead between the degradation map for 100 REM average and the degradation map for 500 REM average showed in Fig.4.12e. The loss-reducing effect given by the averaging operation then reaches saturation. This phenomenon is confirmed by the Fig.4.13, showing the RSS distributions over the positions resulting from the per-position best RSS average on increasing number of erroneously built REMs. Moreover, the cdf of the

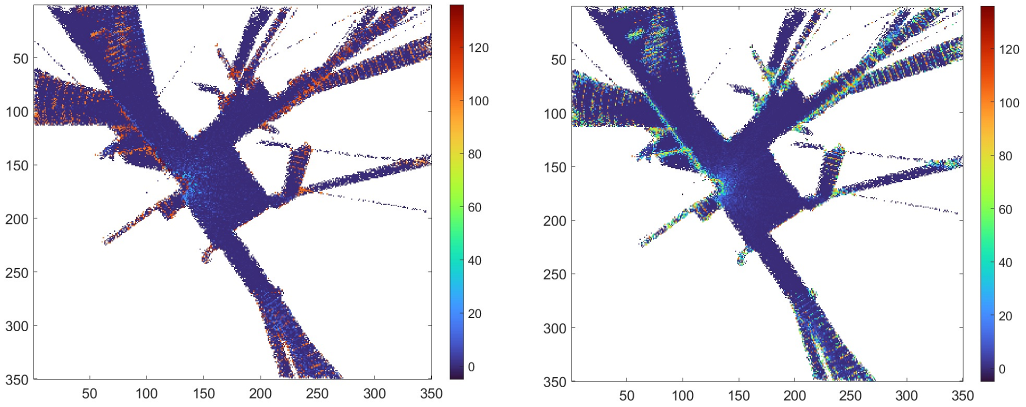

(A) 1 REM average. (B) 5 REM average.

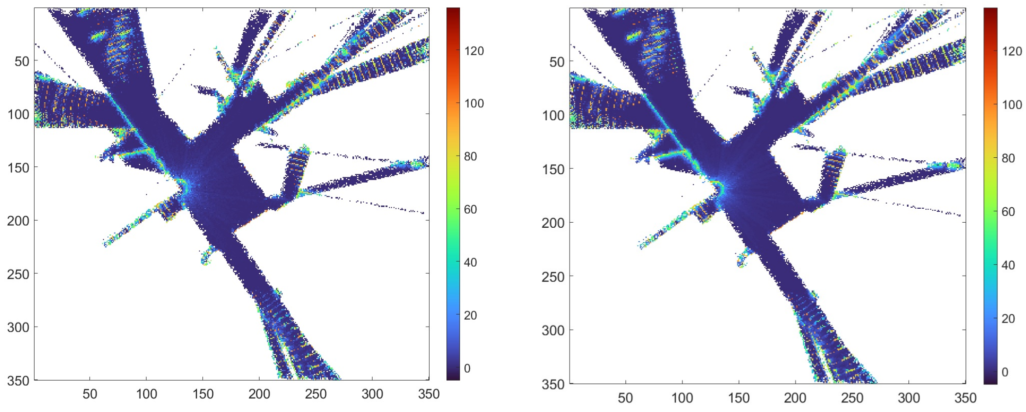

(C) 20 REMs average. (D) 100 REMs average.

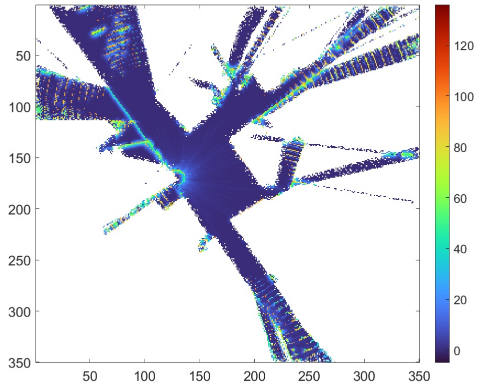

(E) 500 REMs average.

FIGURE 4.12: RSS degradation maps showing the average RSS loss respect to the error-free scenario for increasing number of REMs. The RSS loss is measured in dBm and the GPS error in the REMs construction procedure is normally distributed with $VarSet = 3$ in Tab.3.2.

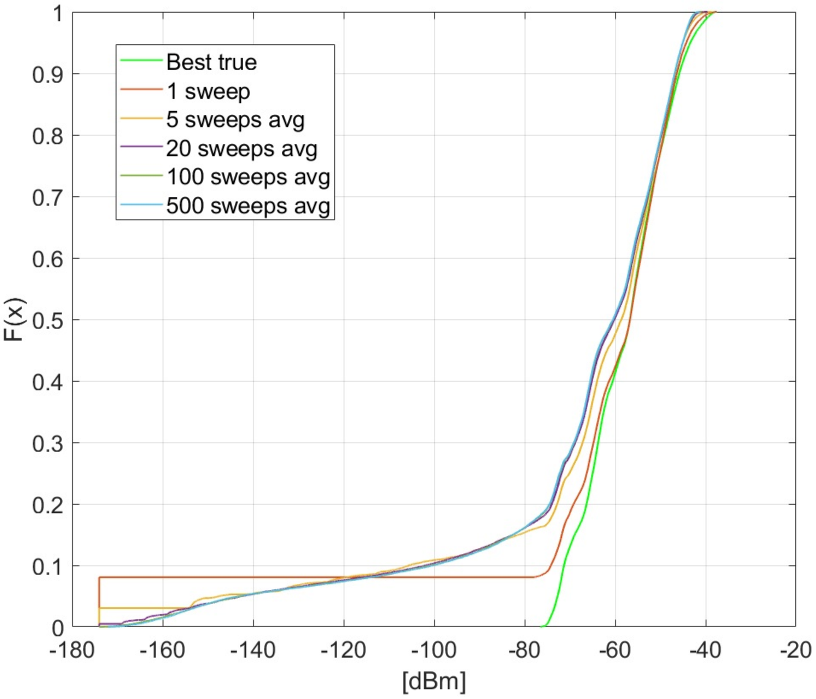

FIGURE 4.13: RSS distributions over the positions in cdf format resulting from the per-position average RSS on increasing number of REM. cdf of the RSS distribution using the correct REM is plotted in green as a comparison. The RSS is measured in dBm and the GPS error in the REMs construction procedure is normally distributed with $VarSet = 3$ in Tab.3.2.

RSS distribution using the correct REM is plotted in green for comparison purposes. Distributions are presented in cdf format.
It can be seen from Fig.4.13 that the worst results is obtained by relying on the 1 sweep erroneous built REM since almost 10% of the attempts result in the minimum RSS. A considerably better result is furnished by the 5 sweeps average scenario, with less than 5% of the total attempts resulting in the minimum RSS value. Averaging on 20 REMs turns out in a further improvement visible with an overall higher average RSS, and in an almost non-existent BPL failure percentage. Further increasing the number of REMs with which to average leads to a barely perceptible performance enhancement, as already pointed out with Fig.4.12. In facts, the cdf curves for 100 sweeps and 500 sweeps overlap, telling that the loss reducing effect consequence of the average reaches saturation.

4.1.2 *Dynamic Scenario*

In this section, the results of the simulation for the dynamic scenario described in Sec. 3.1.3.2 are presented. The dynamic scenario involves the 5 minutes dynamic error model described in Sec. 3.2.2 for performance degradation evaluation. The dynamic error model is correlated, in order to single out the effect of correlation, a comparison is also made by applying the uncorrelated error model described in the following section. The simulation workflow follows the description in Sec. 3.3.1.

The section is organized by presenting and commenting on the results for the correlated GPS error models for the three mobility paths presented in Sec. 3.1.3.2. Sec. 4.1.2.1 shows results for mobility path 1, Sec. 4.1.2.2 shows results for mobility path 2, and Sec. 4.1.2.3 shows the result for the third mobility path. For all the three paths the results are assessed in terms of TX and RX beam ID offset respect to the error-free path, and in terms of bit-rate degradation along the path.

4.1.2.1 *Mobility path 1*

The results for Onrstein-Uhlenbeck correlated error model applied to the first mobility path are analyzed first. As can be seen from Fig.3.7, path 1 starts from a position away from the TX, then approaches while maintaining the LoS condition, and then curves and ends in the NLoS condition. The path crosses a total of 127 positions in the network grid. The latitude and longitude error model parameters selected are those shown respectively in Tab.3.4 and Tab.3.5. The analysis is performed with the parameters for the 5-minute walk and for the three different urban scenarios discussed in the Sec. 3.2.3: San Francisco, Frankfurt, and Hong Kong. To single-out the effect of the correlation, an uncorrelated Gaussian process is also used in the same path as error model. To make a fair comparison, the variance of the error applied to the Gaussian process is the same as the realization instances of the Ornstein-Uhlenbeck correlated error process. In this approach, the correlated and uncorrelated GPS error models have the same impact in terms of error.

San Francisco error model in path 1 Fig.4.14 shows one error model realization in path 1 for correlated error model in Fig.4.14a, and uncorrelated error model in Fig.4.14b using San Francisco GPS error dataset for models tuning. In both the sub figures, the green line indicates the correct path, and the red line indicates the path made incorrect by the GPS error model. In addition, the position of the TX is indicated by the light blue dot. Dark blue areas indicate locations where the data is not available, so these are locations occupied by buildings or not reached way by the TX signal either directly or through reflections. The white-colored areas, on the other hand, are those reached by the signal, so they are positions where the BPL matrix is saved. It can be seen immediately from both Fig.4.14a and Fig.4.14b that the GPS error generated from San Francisco dataset is very small along the path. The difference, however, between the two models is visible: in the correlated case, the erroneous path tends to stay on one side of the true path and then crosses it only infrequently; in the uncorrelated case, on the other hand, the erroneous path crosses the line indicating the true path many times.

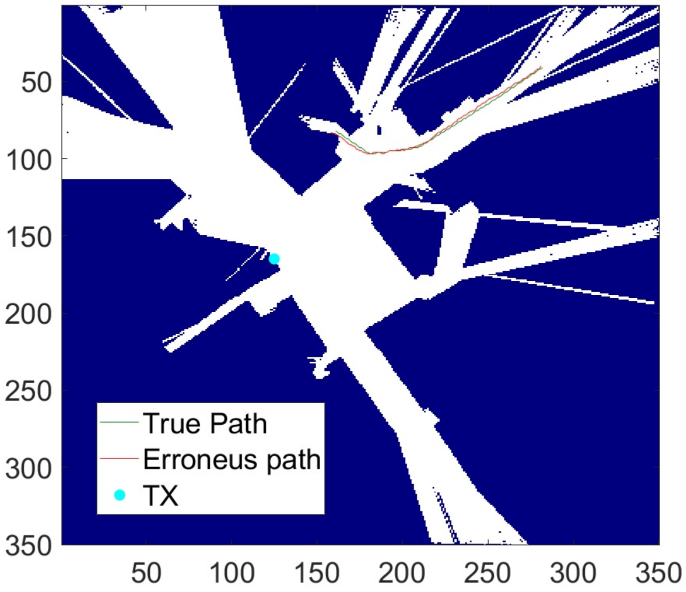

(A) Correlated error model realization instance in the path.

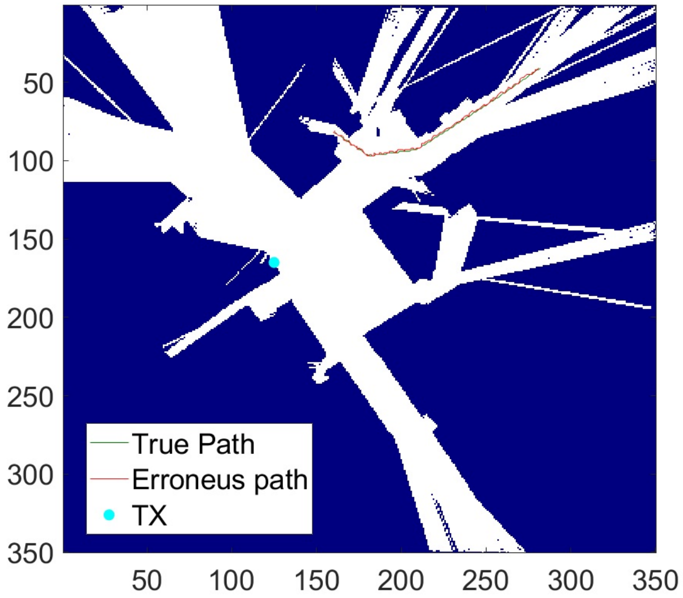

(B) Uncorrelated error model realization instance in the path.

FIGURE 4.14: Error model realization for mobility path 1 with San Francisco error model in the semantic building map. White areas are those where data are available, dark blue areas are areas where data are not available, thus areas occupied by buildings or not reached by the TX signal.

To analyze the causes of worsening performance given by correlated and uncorrelated GPS error models, Fig.4.15 presents results regarding TX and RX beam IDs along the path for the same realization instances of the error models shown in Fig.4.14a and Fig.4.14b. Specifically, the best transmission beam IDs along in path are shown in Fig.4.15a. In the same figure, it can be seen that in the first part of the path the TX beam ID is always the same, except for some isolated fluctuations. This is explained by the fact that initially the UE moves moves toward the TX while staying in front of it, thus is likely to be served by the same TX beam ID. The best beam ID starts to vary gradually as the path begins to curve, and then changes discontinuously at the transition between the LoS and NLoS condition. Offsets of TX beam IDs selected by the correlated and uncorrelated error model with respect to the best beam IDs along the path are illustrated respectively in blue and red in Fig.4.15b. To clarify, most of the blue dots are covered by red dots of equal value. It can be noted that, apart from isolated cases of large mismatch, the offset is for the most part equal to zero for both the correlated error model and uncorrelated error model.
The best RX beam ID along the path shown in the Fig.4.15c has the same characteristics as the best TX beam ID in Fig.4.15a. In fact, it varies at the same points in time but in a more discontinuous manner since the RX has only 16 beams available compared to 64 for the TX. The RX beam ID offsets shown in Fig.4.15d are also almost always equal to zero for both the correlated and the uncorrelated GPS error model. Points other than zero in this case are even rarer than for the TX, this due to the fact that the sector covered by a RX beam ID is larger respect to the TX one.

The effect of the worsening performance given by San Francisco correlated and uncorrelated GPS error models are shown in Fig.4.16 in terms of bit-rate degradation. In particular, Fig.4.16a illustrate the bit-rate performance achieved by the correlated GPS error model, Fig.4.16b the same for the uncorrelated error model. In both the figures, the green line represents the bit-rate along the path in the error-free scenario, it is then the upper bound for the performance. The blue line indicates the average bit-rate along the path for 1000 realizations of the error model. The red line represents the bit-rate achieved by the specific realization displayed in Fig.4.14, and the gray lines indicate the bit-rate reached by other 150 error model realizations. In Fig.4.16a optimal performance is below the maximum achievable bit-rate of 2000Mbps in several points in the first 25 meters. That is because first positions for path 1 are very far from the TX, so the RSS is low because of the distance. Then the UE approaches the transmitter, consequently the optimal bit-rate is equal to the maximum for positions between 25 and 118 meters. The situation changes when switching to NLoS condition, with a sub-optimal bit-rate from position 118 onward and very low from position 123 onward. The average bit-rate follows the optimal bit-rate fairly closely until the transition to NLoS condition when it reaches smaller values. This is explained by the fact that for these in the latter steps the original path passes very close to areas where there is no data, some error realizations may then overlap these areas bringing a bit-rate of zero to those locations and lowering the average. This is exactly the case with the realization shown with the red color, in fact as you can see from the Fig.4.14a the last steps of this realization overlap with areas without data, causing zero bit-rate for those positions. The other grey realizations in Fig.4.16a that deviate from the average do so around the 8th position and 40th position due to proximity and likely overlap with buildings.

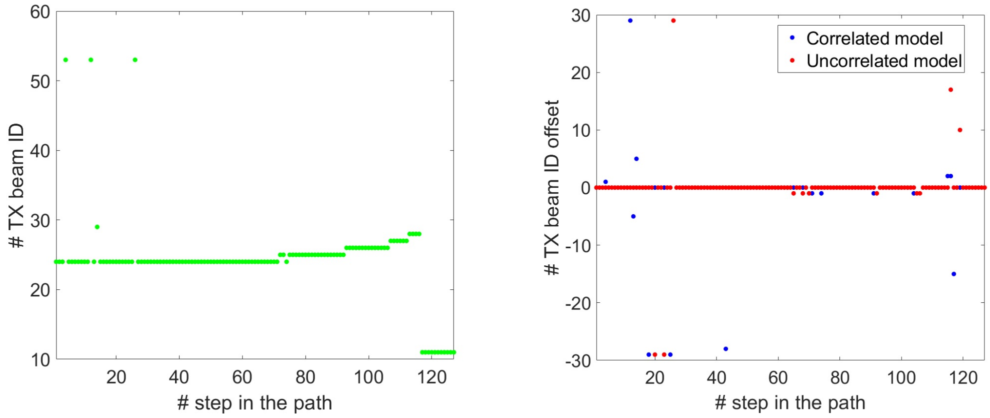

(A) TX best beam ID. (B) TX beam ID offset.

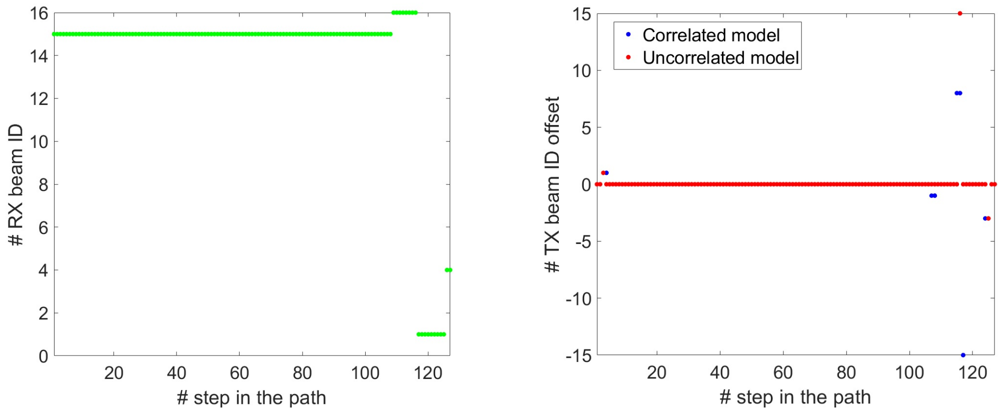

(C) RX best beam ID. (D) RX beam ID offset.

FIGURE 4.15: The top and bottom graphs in the left column show the best TX and RX beam IDs along path 1, respectively. The top and bottom graphs in the left column show offsets against the best beam IDs of San Francisco correlated and uncorrelated error model. Specifically, the upper right graph shows the offset for the TX beam ID and the lower right graph shows the offset of the RX beam ID.

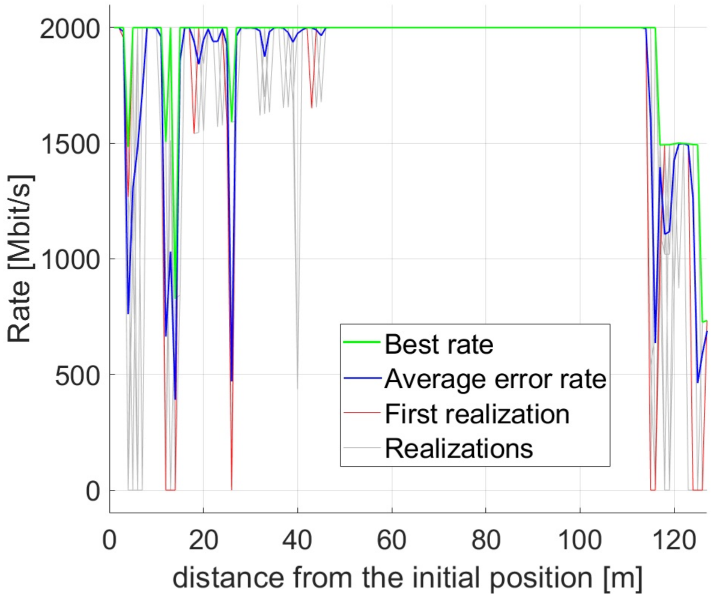

(A) Bit-rate degradation for correlated error model.

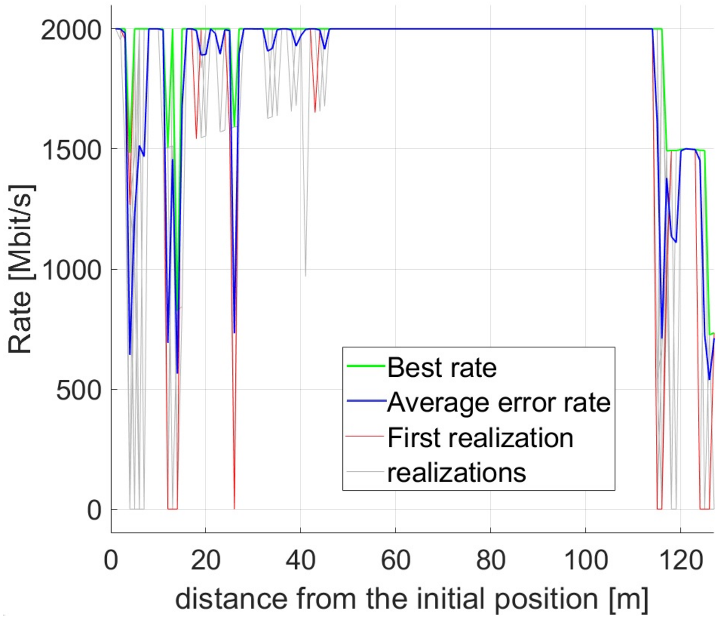

(B) Bit-rate degradation for uncorrelated error model.

FIGURE 4.16: Bit-rate degradation along the path 1 caused by San Francisco error model. Green line represents the rate bit-rate in the error-free scenario, blue line indicates the average bit-rate over 1000 realizations of the error model applied in the path, red line represents the bit-rate achieved by the specific erroneous realization showed in Fig.4.14, and grey lines indicate the bit-rate reached by other 150 error model realizations.

Results for the uncorrelated error model showed in Fig.4.14b are very similar, so the plots need no further comment. The reason why the correlated and the uncorrelated error models achieve similar performance lies in the GPS error dataset with which the models were fitted. GPS errors in San Francisco are very limited because the measurements were collected in an open area, this is therefore reflected by the models. When GPS errors are so small, it is therefore not very important whether the error model is correlated or not.

Frankfurt error model in path 1 Fig.4.17 shows one error model realization for correlated error model in Fig.4.17a, and uncorrelated error model in Fig.4.17b using Frankfurt dataset for model tuning. In both the sub figures, the green line indicates the correct path, and the red line indicates the path made incorrect by the GPS error model. It can be seen from the Fig.4.17a that the error has an important effect, in fact the incorrect path is significantly distant from the correct path almost all the way. This is expected because the Frankfurt error model was fitted to a set of measurements collected in very narrow urban canyons, as explained in Sec. 3.3. Moreover, the error realization shown in Fig.4.17a tends to stay for long periods on the same side from the correct path. Thus, the difference with respect the realization of the uncorrelated error model shown in Fig.4.17b is evident. In fact, the latter continuously crosses the correct path due to the complete lack of correlation. In both scenarios also, the erroneous path overlaps with data-free areas in its last steps.

To analyze the causes of worsening performance given by correlated and uncorrelated GPS error models, Fig.4.18 presents results regarding TX and RX beam IDs along the path for the same realization instances of the error models shown in Fig.4.17a and Fig.4.17b. Specifically, the best TX beam IDs along path 1 are shown in Fig.4.18a and it is reported again for the sake of completeness. Offsets of TX beam IDs selected by the correlated and uncorrelated error models with respect to the best TX beam ID along the path are illustrated respectively in blue and red in Fig.4.18b. It may be noted that the correlated model realization has significant negative TX ID offsets in the first stretch between position 0 and 40. There is also a tract of constant negative offset between positions 23 and 32. Next, between positions 40 and 75 the offset is absent, this is probably because the erroneous position communicated by the UE in this tract is still a frontal position with respect to the TX as it can be seen from Fig.4.17a, it will therefore probably be served by the same TX beam. Between positions 76 and 100 in correspondence with the path curve the offest of the correlated realization is slightly positive. Lastly, at the final positions where the path switches into the NLoS condition, the offset is largely negative and constant. The offset for the uncorrelated error realization shown Fig.4.18b has a wilder and less predictable pattern. In fact, constant offset features are almost absent, and this often changes from negative to positive and vice versa for close positions. The best RX beam ID along path 1 is shown in Fig.4.18c. The RX beam ID offsets shown in Fig.4.18d presents similar characteristics to TX beam ID offsets. Indeed, the correlated realization has a non-zero offset only for the initial positions far from the TX and for the final positions in the NLoS condition. Constant traits can also be noted for the offset of the RX beam ID for the correlated

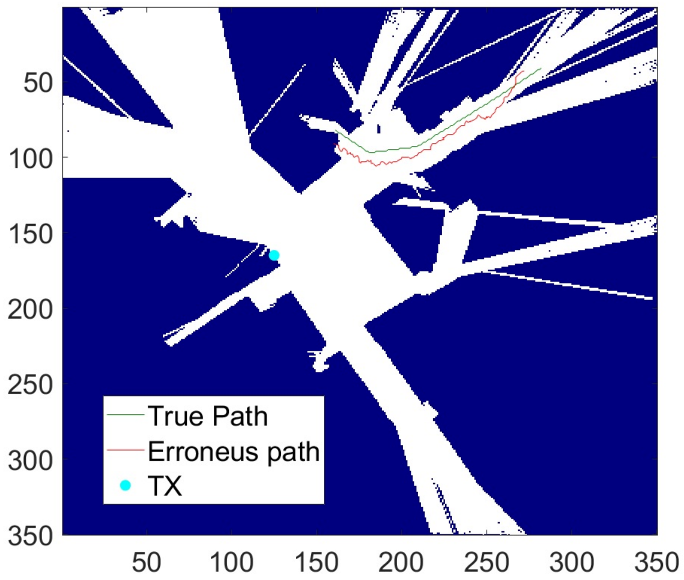

(A) Correlated error model realization instance in the path.

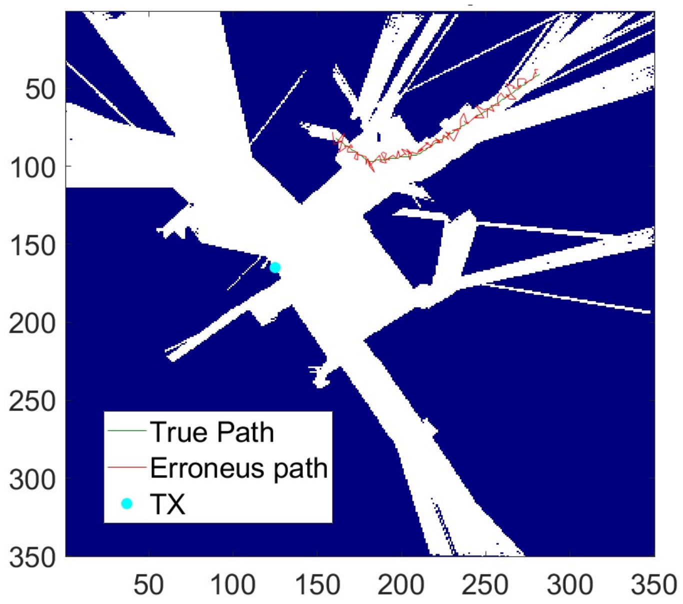

(B) Uncorrelated error model realization instance in the path.

FIGURE 4.17: Error model realization for mobility path 1 with Frankfurt error model in the semantic building map. White areas are those where data are available, dark blue areas are areas where data are not available, thus areas occupied by buildings or not reached by the TX signal.

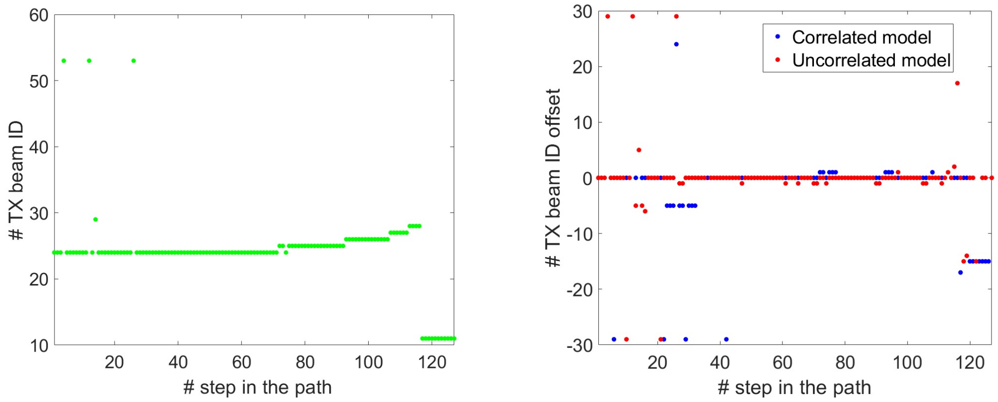

(A) TX best beam ID. (B) TX beam ID offset.

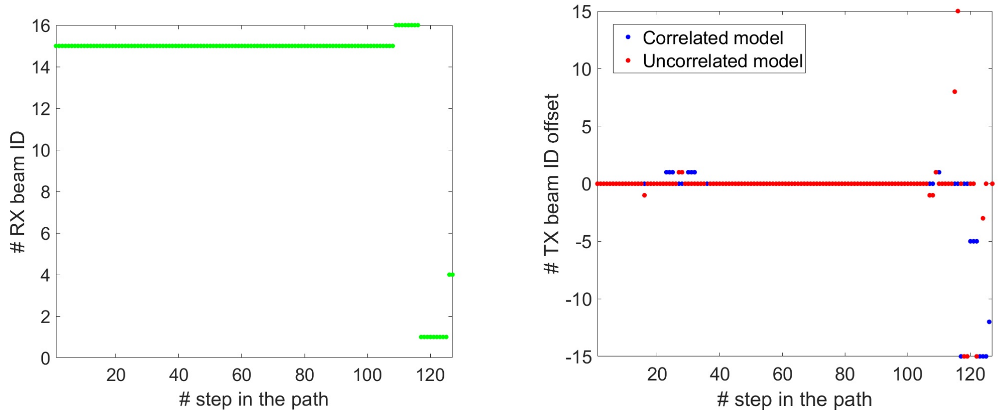

(C) RX best beam ID. (D) RX beam ID offset.

FIGURE 4.18: The top and bottom graphs in the left column show the best TX and RX beam IDs along path 1, respectively. The top and bottom graphs in the left column show offsets against the best beam IDs of Frankfurt correlated and uncorrelated error model. Specifically, the upper right graph shows the offset for the TX beam ID and the lower right graph shows the offset of the RX beam ID.

realization and a wilder behavior for the uncorrelated one. Thus, both the TX and RX beam ID offsets exhibit more predictable behavior for the correlated model. This is because of the fact that the correlated model tends to generate similar errors for successive positions due to correlation.

The effect of the worsening performance given by Frankfurt correlated and uncorrelated GPS error models are shown in Fig.4.19 in terms of bit-rate degradation. In particular, Fig.4.19a illustrate the bit-rate performance achieved by the correlated error model, Fig.4.19b the same for the uncorrelated error model. In both the figures, the green line represents the bit-rate along the path in the error-free scenario, it is then the upper bound for the performance. The blue line indicates the average bit-rate along the path for 1000 realizations of the error model. The red line represents the bit-rate achieved by the specific realization displayed in Fig.4.17, and the gray lines indicate the bit-rate reached by other 150 error model realizations. It can be noted that the correlated model achieves a higher average bit-rate than the uncorrelated model in the initial positions between positions 0 and 60. This is given by the fact that many realizations of the correlated model tend to be located closer to the TX than the true path for these initial positions. This is the case, for example, of the realization shown in Fig.4.17a. Both the average bit-rate for the correlated and the uncorrelated error model reach the maximum value for positions between 87 and 110, these are in fact the closest positions to the TX for path 1 and the GPS error therefore does not seem to impact. The uncorrelated model, however, achieves a higher average bit-rate in the last positions of the path, those characterized by the NLoS condition. This phenomenon can be explained by the fact that many realizations of the correlated model have large overlaps with the data-free areas in the map at these final positions. This leads 0 bit-rate for those realizations and a consequent lowering of the average. It is also the case for the realization shown in Fig.4.17a. Another evident difference between the two models lies in the lower average bit-rate of the uncorrelated model for positions between 55 and 67, this is demonstrated by the numerous gray realizations in the Fig.4.19b having very low bit-rates for those positions.

Hong Kong error model in path 1 Fig4.20 shows one error model realization for correlated error model in Fig.4.20a, and uncorrelated error model in Fig.4.20b using Frankfurt dataset for model tuning. In both the sub figures, the green line indicates the correct path, and the red line indicates the path made incorrect by the GPS error model. It can be seen in Fig.4.20a that Hong Kong dataset generates an error model that is more impactful than that generated for San Francisco but less than that generated for Frankfurt. This follows expectations because the measurements are collected in an urban area but with less narrow urban canyons than Frankfurt, as described in Sec. 3.2.3. Also the erroneous realization shown in Fig.4.20a tends to stay for long periods on the same side from the correct path. Instead, the uncorrelated model shown in Fig.4.20b tends to cross the green line representing the correct path many times because of the lack of correlation.

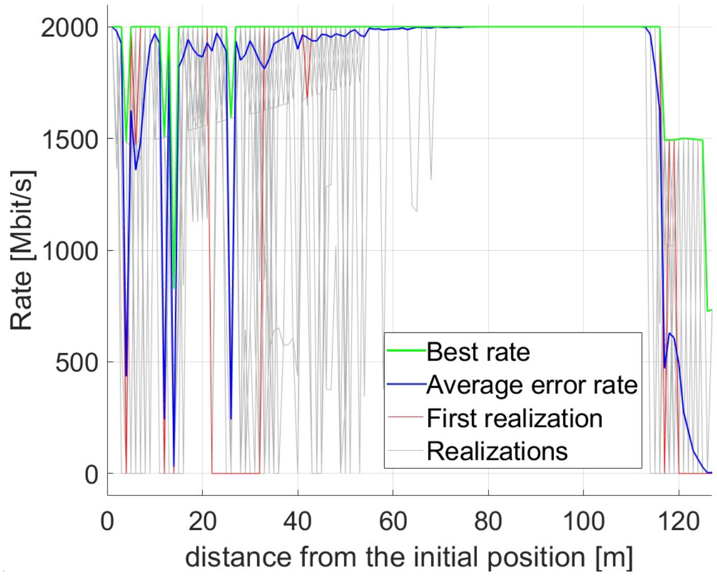

(A) Bit-rate degradation for correlated error model.

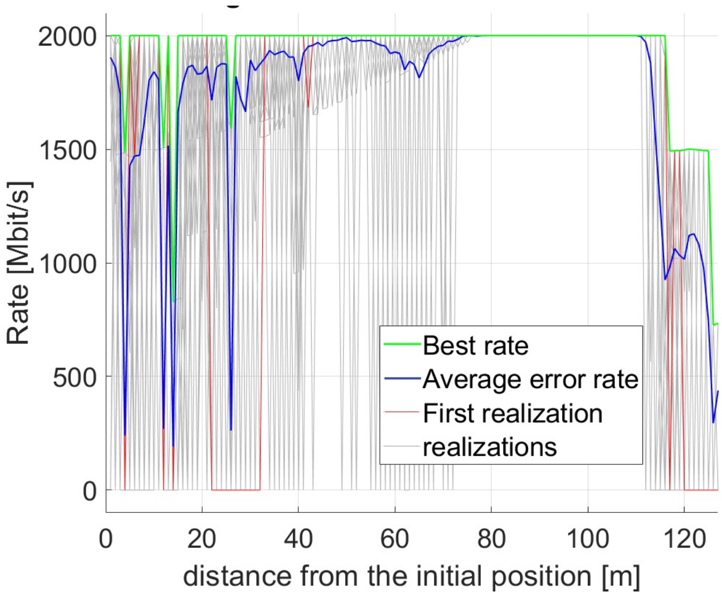

(B) Bit-rate degradation for uncorrelated error model.

FIGURE 4.19: Bit-rate degradation along the path 1 caused by Frankfurt error model. Green line represents the rate bit-rate in the error-free scenario, blue line indicates the average bit-rate over 1000 realizations of the error model applied in the path, red line represents the bit-rate achieved by the specific erroneous realization showed in Fig.4.17, and grey lines indicate the bit-rate reached by other 150 error model realizations.

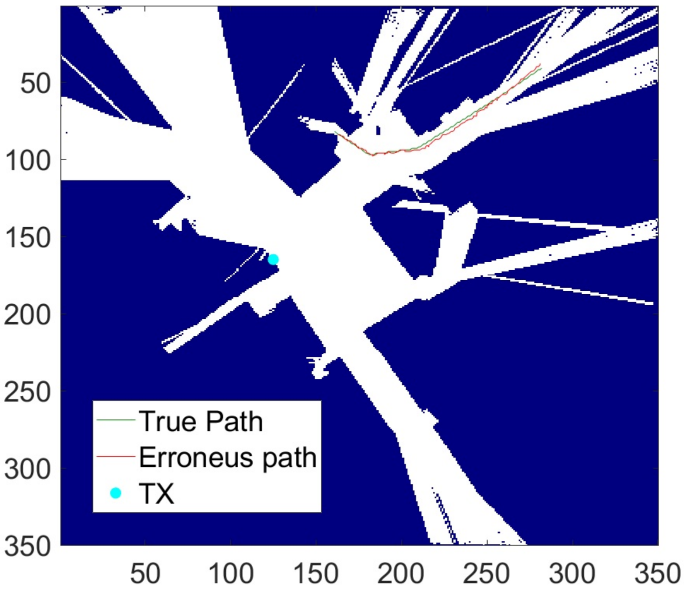

(A) Correlated error model realization instance in the path.

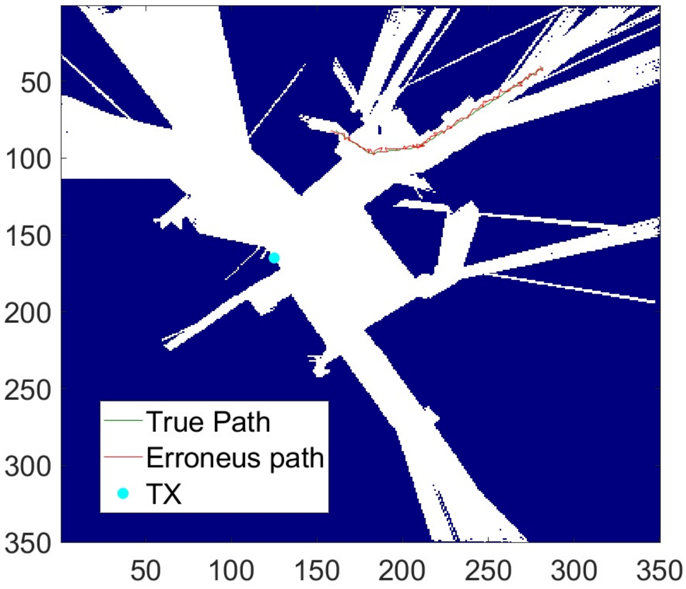

(B) Uncorrelated error model realization instance in the path.

FIGURE 4.20: Error model realization for mobility path 1 with Hong Kong error model in the semantic building map. White areas are those where data are available, dark blue areas are areas where data are not available, thus areas occupied by buildings or not reached by the TX signal.

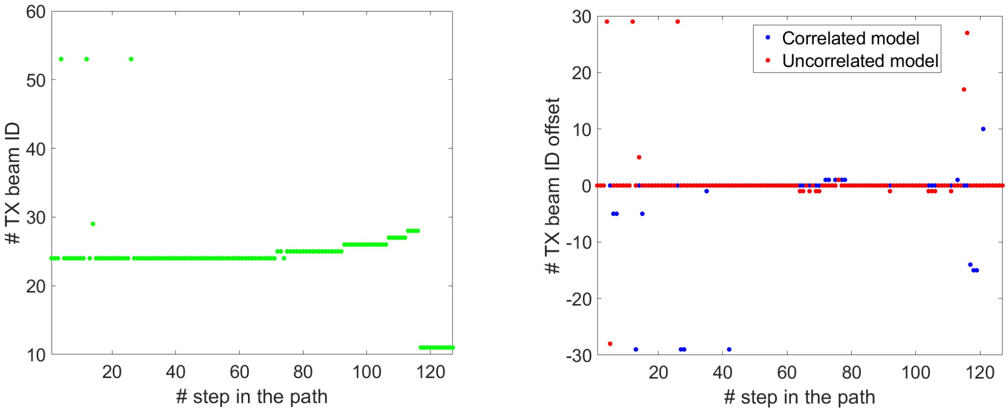

(A) TX best beam ID.

(B) TX beam ID offset.

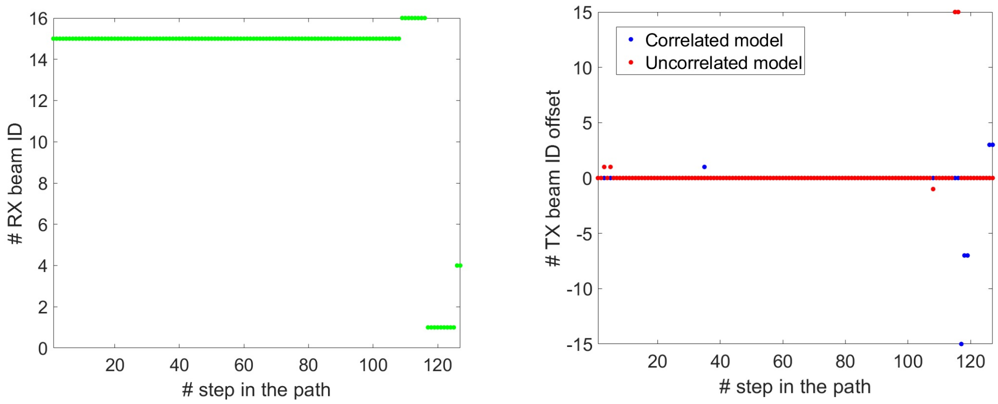

(C) RX best beam ID.

(D) RX beam ID offset.

FIGURE 4.21: The top and bottom graphs in the left column show the best TX and RX beam IDs along path 1, respectively. The top and bottom graphs in the left column show offsets against the best beam IDs of Hong Kong correlated and uncorrelated error model. Specifically, the upper right graph shows the offset for the TX beam ID and the lower right graph shows the offset of the RX beam ID.

Fig.4.21 presents results regrading TX and RX beam IDs along the path for the same realization instances of the error models shown in Fig.4.20a and Fig.4.20b. Specifically, the best TX beam IDs along path 1 are shown in Fig.4.18a and it is reported again for the sake of completeness. Offsets of TX beam IDs selected by the correlated and uncorrelated error model with respect to the best beam ID along the path are illustrated respectively in blue and red in Fig.4.21b. It can be noted that TX ID offsets for the correlated path are are all either zero or negative in the first half of the path. This can be explained by the fact that the realization for which the offset was calculated almost always remains on the same side with respect to the true path for the first half of the path, as can be seen in Fig.4.20a. Immediately after the half of the path, the offset is slightly positive and constant for the positions between 72 and 78. When the UE switches to the NLoS condition at the end of the path, the TX offset for the correlated model assumes both largely positive and largely negative values. Regarding the TX offset for the uncorrelated model shown in Fig.4.21b, this shows no particular pattern except between positions 64 and 70 where it takes on constant slightly negative values. The best RX beam ID along path 1 is shown in Fig.4.21c. The RX beam ID offset plots shown in Fig.4.21d has very few non-zero points for both the correlated and the uncorrelated model. The only points noticeably different from zero for both models are related to some positions at the end of the path, thus in the NLoS condition.

The effect of the worsening performance given by Hong Kong correlated and uncorrelated error models are shown in Fig.4.22 in terms of bit-rate degradation. In particular, Fig.4.22a illustrate the bit-rate performance achieved by the correlated error model, Fig.4.22b the same for the uncorrelated model. In both the figures, the green line represents the bit-rate along the path in the error-free scenario, it is then the upper bound for the performance. The blue line indicates the average bit-rate along the path for 1000 realizations of the error model. The red line represents the bit-rate achieved by the specific realization displayed in Fig.4.20, and the gray lines indicate the bit-rate reached by other 150 error model realizations. It can be seen that correlated and uncorrelated models achieve similar average bit-rate performances, especially in the first half of path 1 when the UE sufficiently far from the TX. Then the average bit-rate provided by the two models remains equal to the maximum bit-rate up to the path curve and then to the next NLoS condition transition for position 114. Under NLoS condition, the correlated error model gives a lower average bit-rate than the uncorrelated one, as it can be seen from the two average bit-rate relevant drops for positions 117 and 126 in Fig.4.22a. Average bit-rate provided by the uncorrelated model reaches negative peaks for the same positions, but these are less serious. The explanation lies in the fact that for those two positions the path passes very close to data-free areas, and the correlated model makes overlap with these areas more likely. Also relevant is the fact that the realization plotted in red in both Fig.4.22a and Fig.4.22b achieve bit-rates equal to zero for the same position equal to 118. Events of this occur for positions very close to the transition between zones served by different TX or RX beams, so that even a small imprecision in the notified position causes a drop in performance, regardless of the GPS error model is correlated or not.

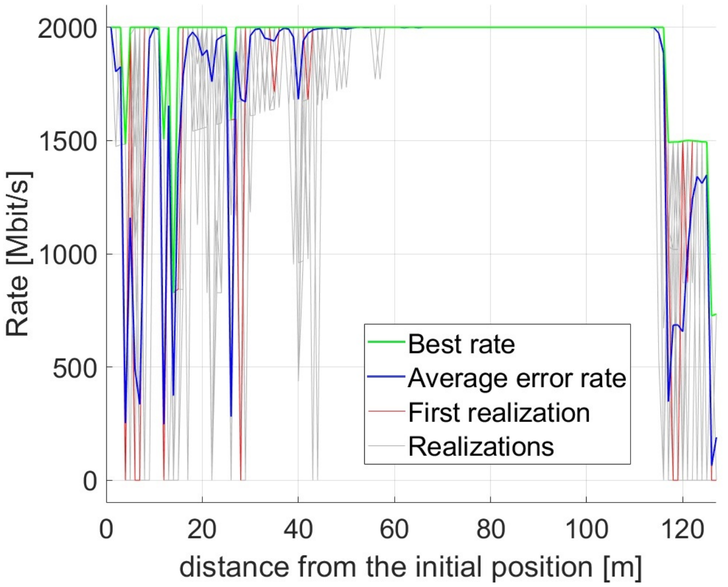

(A) Bit-rate degradation for correlated error model.

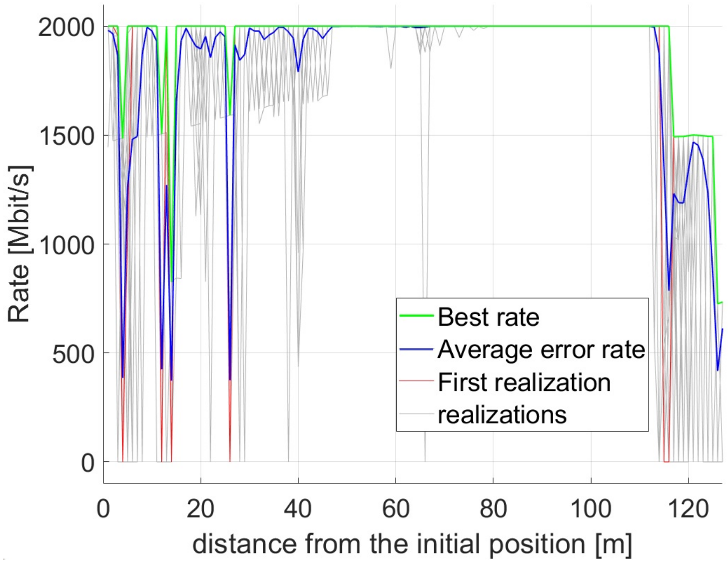

(B) Bit-rate degradation for uncorrelated error model.

FIGURE 4.22: Bit-rate degradation along the path 1 caused by Hong Kong error model. Green line represents the rate bit-rate in the error-free scenario, blue line indicates the average bit-rate over 1000 realizations of the error model applied in the path, red line represents the bit-rate achieved by the specific erroneous realization showed in Fig.4.20, and grey lines indicate the bit-rate reached by other 150 error model realizations.

4.1.2.2 Mobility path 2

The results for Ornstein-Uhlenbck correlated error model applied to the second mobility path are now analyzed. As it can be seen from Fig.3.1.3.2, path 2 is entirely in LoS condition but it starts from a very far position from the TX, gets close to it and walks away again. For this reason, a significant channel variation is expected. Path 2 is the longest since it crosses 196 positions in the network grid. The latitude and longitude error model parameters selected are those shown respectively in Tab.3.4 and Tab.3.5. The analysis is performed for the 5-minutes walk and for the three different urban scenarios discussed in Sec. 3.3: San Francisco, Frankfurt, and Hong Kong. To single-out the effect of the correlation, an uncorrelated Gaussian process is also used in the same path as error model. To make a fair comparison, the variance of the error applied to the Gaussian process is the same as the realization of the Ornstein-Uhlenbeck correlated error process. In this approach, the correlated and uncorrelated GPS error models have the same impact in terms of error.

San Francisco error model in path 2 Fig.4.23 shows one error model realization in path 2 for uncorrelated error model in Fig.4.23a, and uncorrelated error model in Fig.4.23b using San Francisco GPS error dataset for model tuning. In both the sub figures, the green line indicates the correct path, and the red line indicates the path made incorrect by the GPS error model. In addition, the position of the TX is indicated by the light blue dot. It can be seen from Fig.4.23a and Fig.4.23b that the GPS error generated from San Francisco dataset is very small also in path 2. Despite this, the correlated model realization shown in Fig.4.23a tends to visibly deviate from the correct path in the first stretch and then move back closer to the green line. This phenomenon can occur and is typical of Ornstein-Uhlenbeck process due to its mean-reverting property. On the other hand, the realization of the uncorrelated error model shown in Fig.4.23b is again without a definite pattern.

Fig.4.24 presents results regarding the TX and RX beam IDs along the path for the same realization instances of the error models shown in Fig.4.23a and Fig.4.23b. Specifically, the best TX beam IDs for the correct path are shown in Fig.4.24a. In the same figure it can be seen that best TX is constant between position 0 and 70, except for some isolated small fluctuation. This makes sense because the corresponding map positions are far from the TX and probably covered by the same TX beam sector given a hypothetical projection of these sectors. The correct TX beam ID then changes quickly and in almost continuous manners between the positions 71 and 115. These are the positions corresponding to the transition in front of the TX, consequently moving even a little implies changing TX beams given the proximity. In the last portion of the path the correct beam ID returns to be almost constant given the movement away from the TX. Offsets of TX beam IDs selected by the correlated and uncorrelated error model with respect to the best beam IDs along the path are illustrated respectively in blue and red in Fig.4.24b. It can be noted that the correlated error model acquires more non-zero offsets than the uncorrelated one in the first positions. This is given by the specific correlated realization plotted since, as already pointed out in the section, the model acquires extraordinarily large error values for this first positions. On the other hand, the uncorrelated model acquires some very large offset values for the position

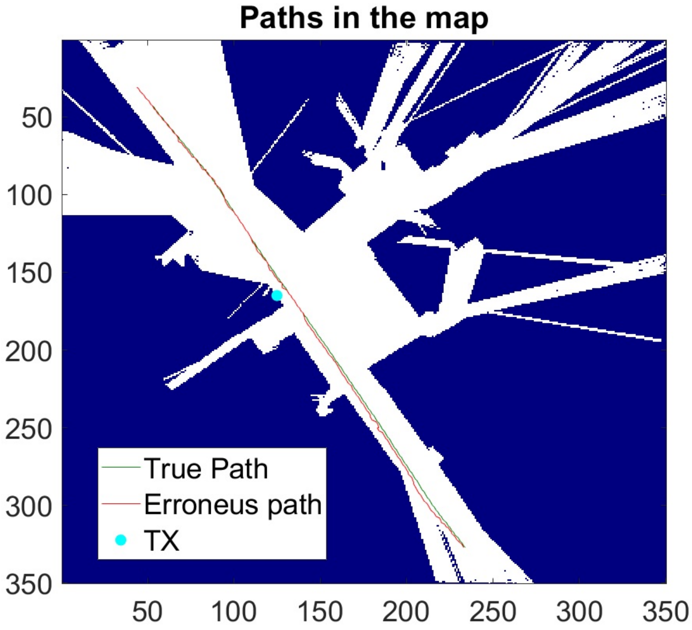

(A) Correlated error model realization instance in the path.

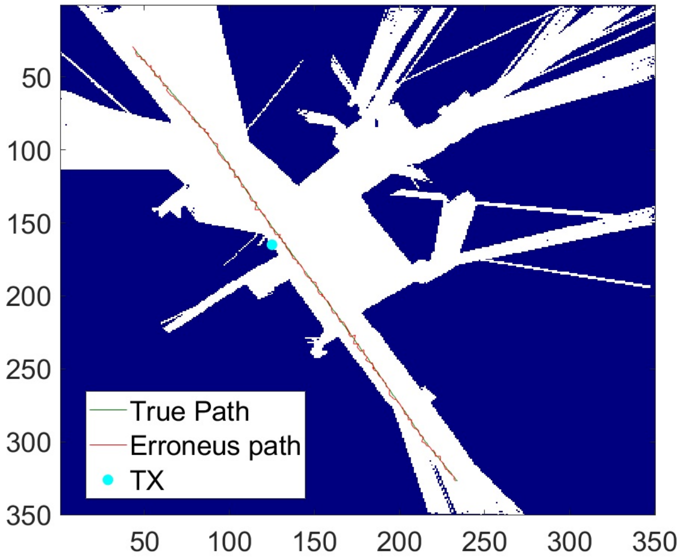

(B) Uncorrelated error model realization instance in the path.

FIGURE 4.23: Error model realization for mobility path 2 with San Francisco error model in the semantic building map. White areas are those where data are available, dark blue areas are areas where data are not available, thus areas occupied by buildings or not reached by the TX signal.

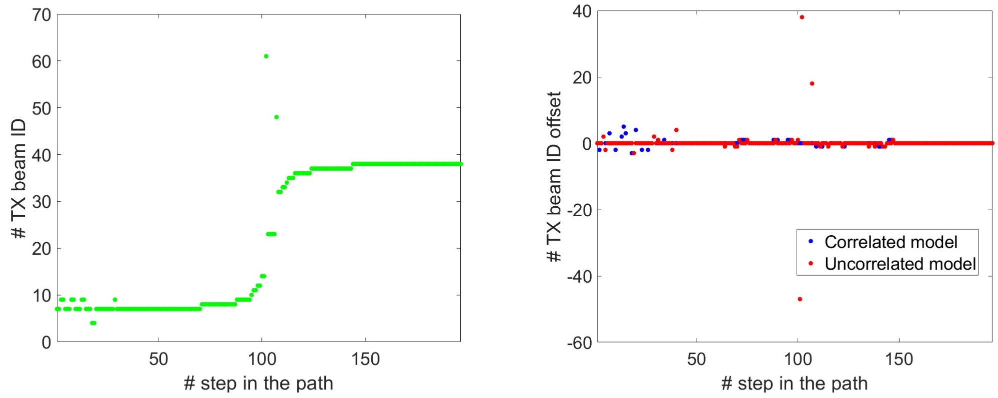

(A) TX best beam ID.

(B) TX beam ID offset.

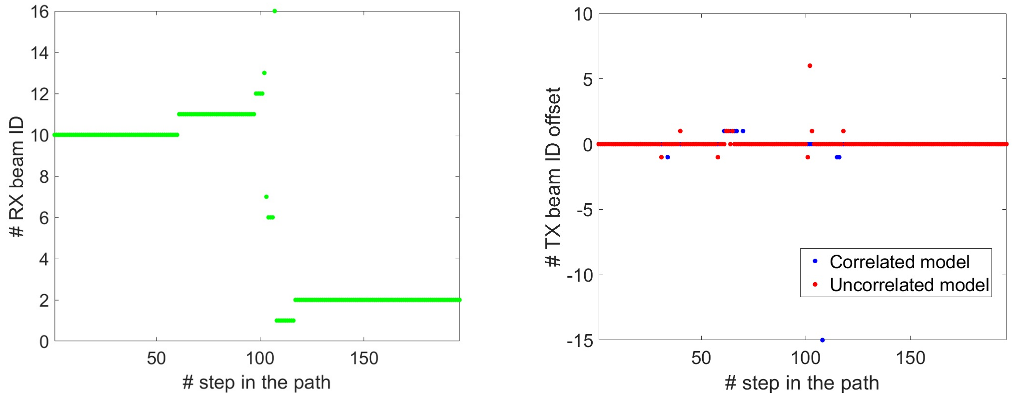

(C) RX best beam ID.

(D) RX beam ID offset.

FIGURE 4.24: The top and bottom graphs in the left column show the best TX and RX beam IDs along path 2, respectively. The top and bottom graphs in the left column show offsets against the best beam IDs of San Francisco correlated and uncorrelated error model. Specifically, the upper right graph shows the offset for the TX beam ID and the lower right graph shows the offset of the RX beam ID.

close to the TX. This does not happen for the correlated model because that realization acquires almost negligible error for those position, as it can be seen from Fig.4.23a. In the last part of the path both correlated and uncorrelated error model have almost always zero offset. The best RX beam ID along the path are shown in the Fig.4.24c has the same characteristics as the best TX beam ID in Fig.4.24a. In fact, it varies at the same points in time but in a more discontinuous manner since the RX has only 16 beams available compared to 64 for the TX. The RX beam ID offsets shown in Fig.4.24d are almost always equal to zero for both the correlated and the uncorrelated GPS error model. However, the slightly positive constant offset for the correlated error model can be noted between positions 61 and 67.

The effect of the worsening performance given by San Francisco correlated and uncorrelated GPS error models applied for path 2 are shown in Fig.4.25 in terms of bit-rate degradation. In particular, Fig.4.25a illustrate the bit-rate performance achieved by the correlated GPS error model, Fig.4.25b the same for the uncorrelated error model. In both the figures, the green line represents the bit-rate along the path in the error-free scenario, it is then the upper bound for the performance. The blue line indicates the average bit-rate along the path for 1000 realizations of the error model. The red line represents the bit-rate achieved by the specific realization displayed in Fig.4.23, and the gray lines indicate the bit-rate reached by other 150 error model realizations. In Fig.4.25a optimal bit-rate performance is below the maximum achievable bit-rate of 2000Mbps in the first 30 positions. That is because these are positions very far from the TX so the RSS is low on average. The other positions where the best bit-rate is below the maximum achievable are the ones very close to the TX. It can be noted that by comparing the average bit-rate for the correlated model in Fig.4.25a and the average bit-rate for uncorrelated error model if Fig.4.25b, that the average bit-rate achieved by the uncorrelated error model is higher in the first 30 positions. That is evident by looking at the different entity of the negative peak reached by both the models for position equal to 18. That is because that is a position very close to data-free area and correlated error model is likely to overlap those areas for longer periods. This phenomenon lowers the average bit-rate because bit-rate equal to 0 is reported for overlapping realizations. Average bit-rate is also below the best one for positions between 100 and 108 in front of the TX. In this circumstance, the average bit-rate for correlated model is higher with respect to the uncorrelated one. This probably happens because the wilder position fluctuations given by the uncorrelated model are particularly harmful in areas very close to the TX. Areas where two adjacent positions might be characterised by two different best TX and RX beam IDs. Example of this occurrence is the realization of the uncorrelated model marked in red in the Fig.4.25b at position 107.

Frankfurt error model for path 2 Fig.4.26 shows one error model realization for the correlated error model in Fig.4.26a, and uncorrelated error model in Fig.4.26b using Frankfurt dataset for model tuning. In both the sub figures, the green line indicates the correct path, and the red line indicates the path made incorrect by the GPS error model. It can be seen from Fig.4.26a that the error has a non negligible effect, in

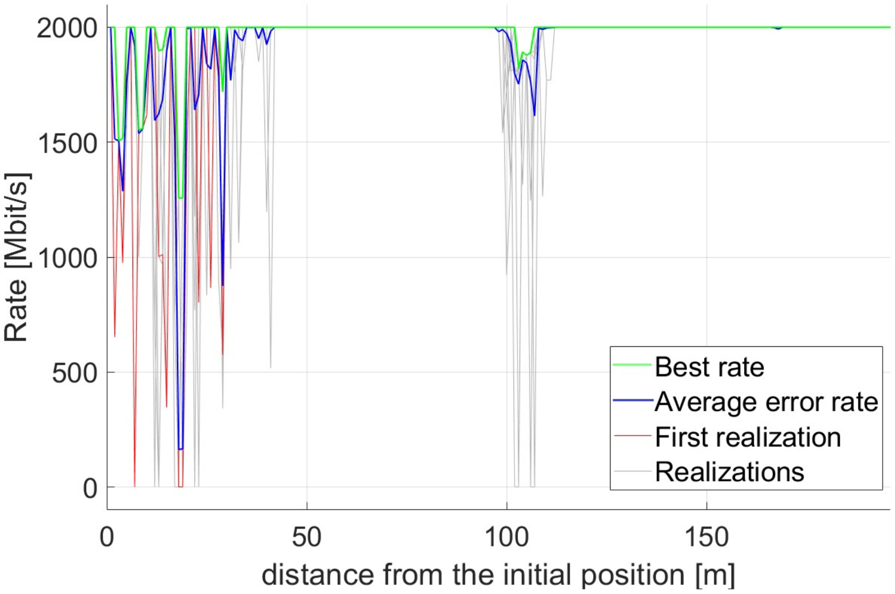

(A) Bit-rate degradation for correlated error model.

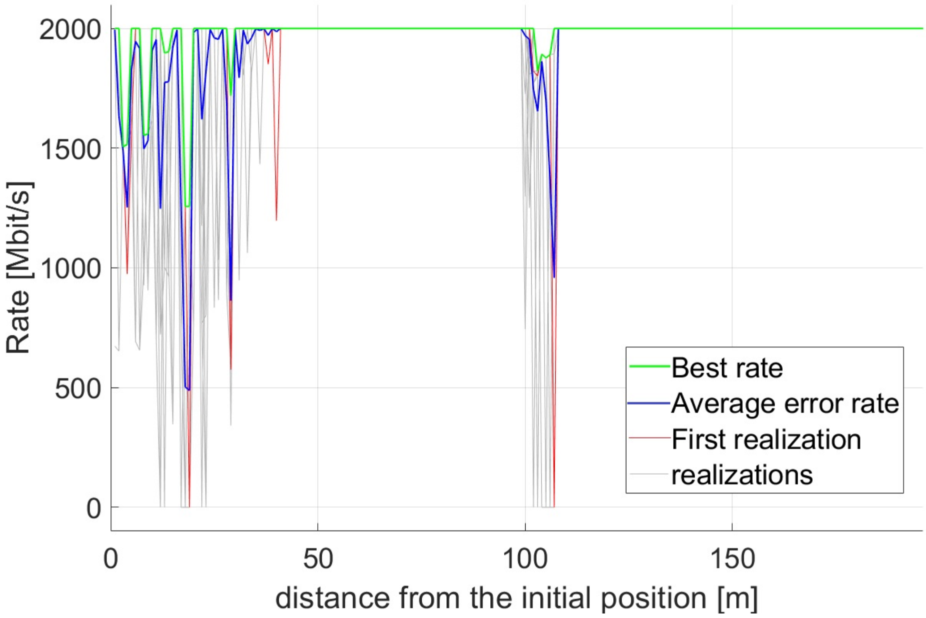

(B) Bit-rate degradation for uncorrelated error model.

FIGURE 4.25: Bit-rate degradation along the path 2 caused by San Francisco error model. Green line represents the rate bit-rate in the error-free scenario, blue line indicates the average bit-rate over 1000 realizations of the error model applied in the path, red line represents the bit-rate achieved by the specific erroneous realization showed in Fig.4.23, and grey lines indicate the bit-rate reached by other 150 error model realizations.

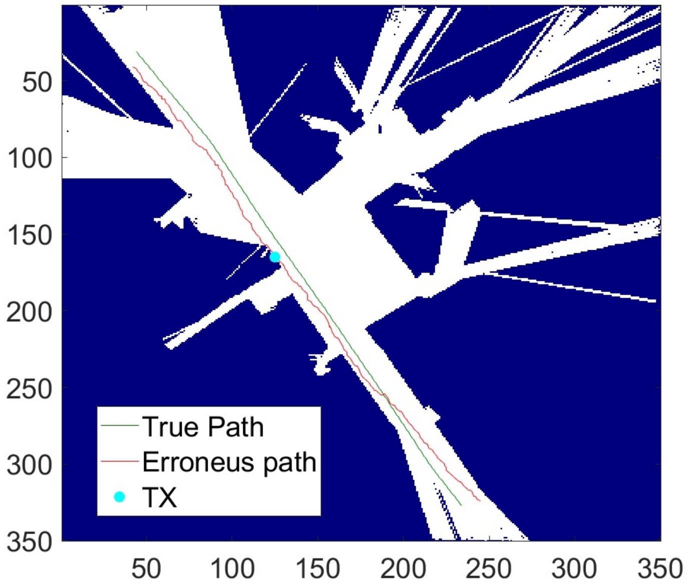

(A) Correlated error model realization instance in the path.

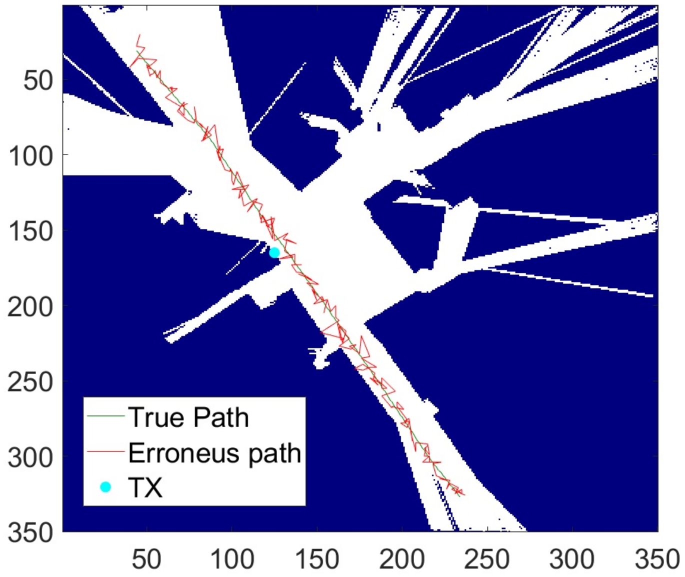

(B) Uncorrelated error model realization instance in the path.

FIGURE 4.26: Error model realization for mobility path 2 with Frankfurt error model in the semantic building map. White areas are those where data are available, dark blue areas are areas where data are not available, thus areas occupied by buildings or not reached by the TX signal.

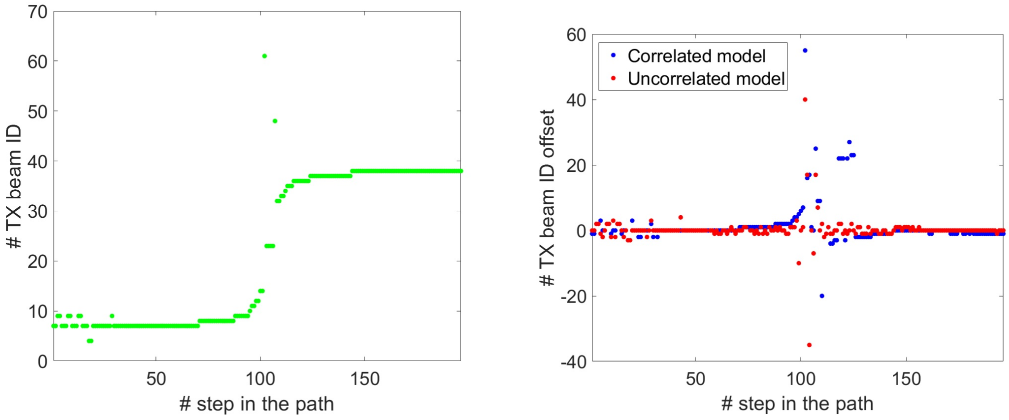

(A) TX best beam ID.

(B) TX beam ID offset.

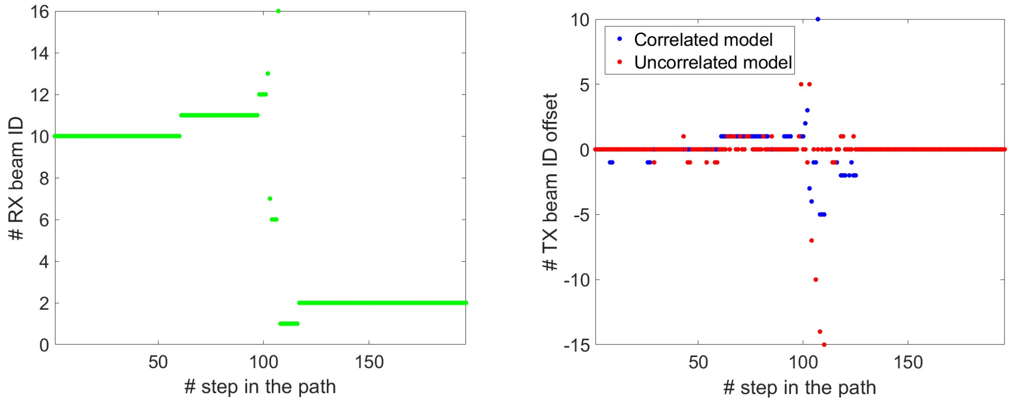

(C) RX best beam ID.

(D) RX beam ID offset.

FIGURE 4.27: The top and bottom graphs in the left column show the best TX and RX beam IDs along path 2, respectively. The top and bottom graphs in the left column show offsets against the best beam IDs of Frankfurt correlated and uncorrelated error model. Specifically, the upper right graph shows the offset for the TX beam ID and the lower right graph shows the offset of the RX beam ID.

fact some erroneous positions are even 10 meters far from the correspondent correct position. This is because the Frankfurt error model is the heaviest in terms of error among the three considered. Moreover, the correlated realization instance shown in Fig.4.26 crosses the green line indicating the correct path only once, and then stays at the same side of it until the end. On the other hand, the uncorrelated error realization shown in Fig.4.26b crosses the green lines continuously and sometimes it overlaps the data-free areas.

Fig.4.27 presents results regarding TX and RX beam IDs along the path for the same realization instances of the error models shown in Fig.4.26a and Fig.14.26b. Specifically, the best TX beam IDs along path 2 are shown in Fig.4.27a and reported again for the sake of completeness. Offsets of TX beam IDs selected by the correlated and uncorrelated error models with respect the best TX beam ID along the path are illustrated respectively in blue and red in Fig.4.27b. It may be noticed that both correlated and uncorrelated error models provides small but frequent TX ID offset for positions between 0 and 32. The largest offsets are achieved by both the models in correspondence of positions very close to the TX. However, a difference can be seen between the two offset trends. In fact, the correlated offset increases very rapidly as it comes close to the TX and, once passed, assumes very negative values to quickly return to values around 0. On the other hand, the uncorrelated TX offset in Fig.4.27b also takes values very different from zero for those positions but in a more confusing way and without following a pattern. The RX best beam IDs for the correct path are shown in Fig.4.27c. RX beam ID offset for correlated model plotted in Fig.4.27d follows a similar trend to the TX correlated offset, since it assumes positive values when UE gets closer to the TX and negative values once passed it. RX beam ID offset for uncorrelated model assumes larger absolute offset values then the correlated one for positions close to the TX but in a more discontinuous trend.

The effect of the worsening performance given by Frankfurt correlated and uncorrelated GPS error models applied for path 2 are shown in Fig.4.28 in terms of bit-rate degradation. In particular, Fig.4.28a illustrate the bit-rate performance achieved by the correlated GPS error model, Fig.4.28b the same for the uncorrelated error model. In both the figures, the green line represents the bit-rate along the path in the error-free scenario, it is then the upper bound for the performance. The blue line indicates the average bit-rate along the path for 1000 realizations of the error model. The red line represents the bit-rate achieved by the specific realization displayed in Fig.4.26, and the gray lines indicate the bit-rate reached by other 150 error model realizations. It can be seen that correlated and uncorrelated error models achieve similar average bit-rate for initial positions between 0 and 40, with the uncorrelated error model performing slightly worse. In contrast, for positions between 40 and 80 the uncorrelated model gives a significantly lower average bit-rate than the correlated one. That can also be seen through the many gray realizations with low bit-rates for those positions in the Fig.4.28b, instead that area of the graph is almost clean for the correlated model in the Fig.4.28a. Both models have a significantly lower average bit-rate than the best achievable for positions between 80 and 120 corresponding to areas very close to the TX, this is especially true for the correlated model. The bad performance is because the sector covered by one beam ID is very narrow for these position, so even a slight inaccuracy about the location can be very damaging. Lastly, both error models give an average bit-rate close to the optimal for the remaining positions between 120 and 196, with the uncorrelated model performing slightly worse for the very last positions.

Hong Kong error model for path 2 Fig.4.29 shows one error model realization for the correlated error model in Fig.4.29a, and uncorrelated error model in Fig.4.29b using Frankfurt dataset for model tuning. In both the sub figures, the green line indicates the correct path, and the red line indicates the path made incorrect by the GPS error model. It can be seen that Hong Kong error models have greater impact than the model for San Francisco but less than the model for Frankfurt. In fact model

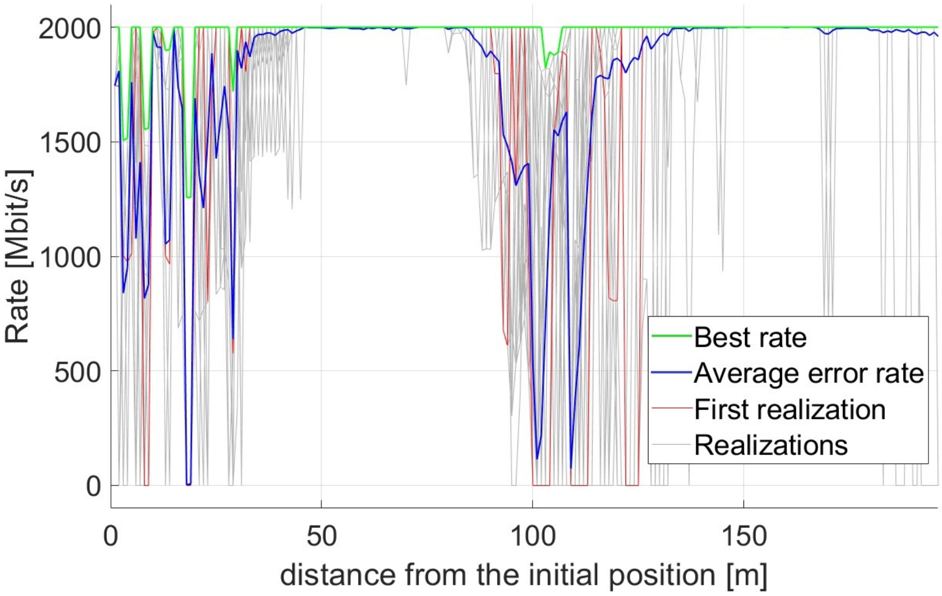

(A) Bit-rate degradation for correlated error model.

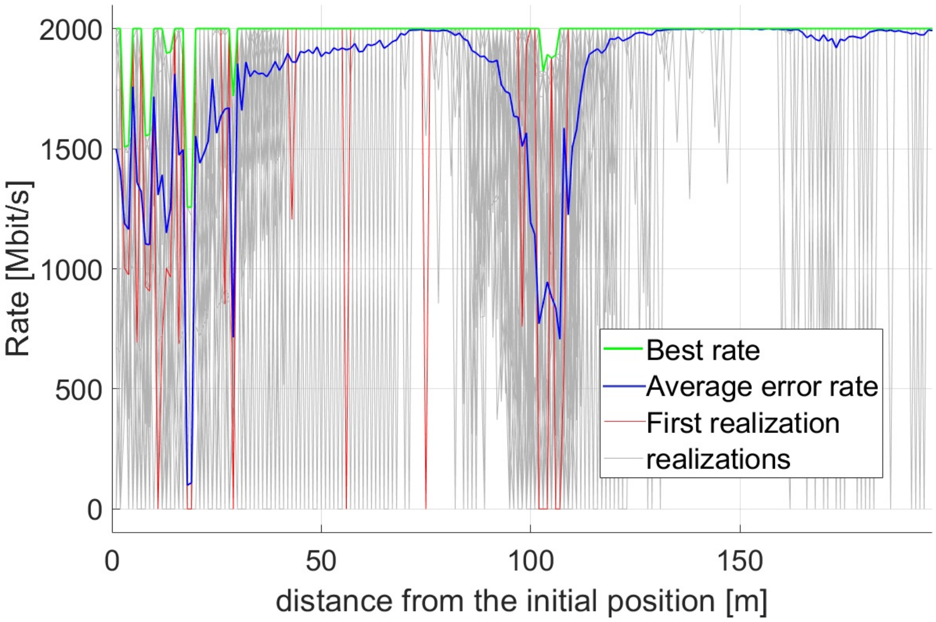

(B) Bit-rate degradation for uncorrelated error model.

FIGURE 4.28: Bit-rate degradation along the path 2 caused by Frankfurt error model. Green line represents the rate bit-rate in the error-free scenario, blue line indicates the average bit-rate over 1000 realizations of the error model applied in the path, red line represents the bit-rate achieved by the specific erroneous realization showed in Fig.4.26, and grey lines indicate the bit-rate reached by other 150 error model realizations.

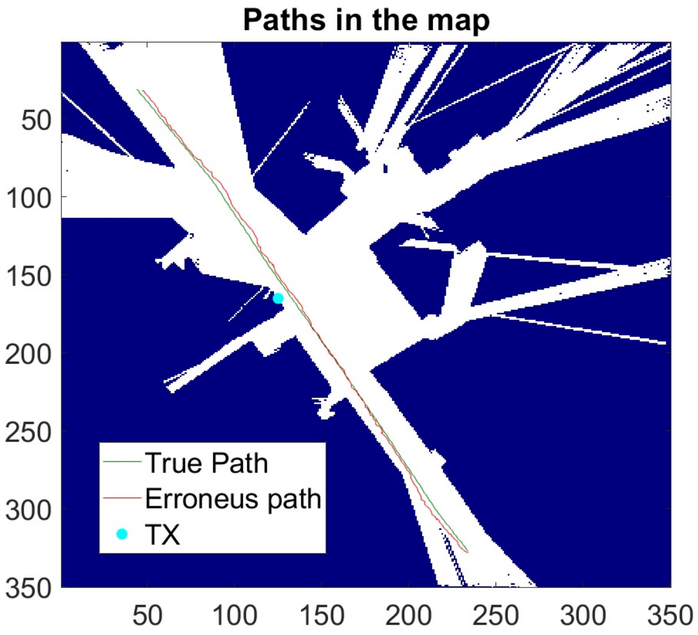

(A) Correlated error model realization instance in the path.

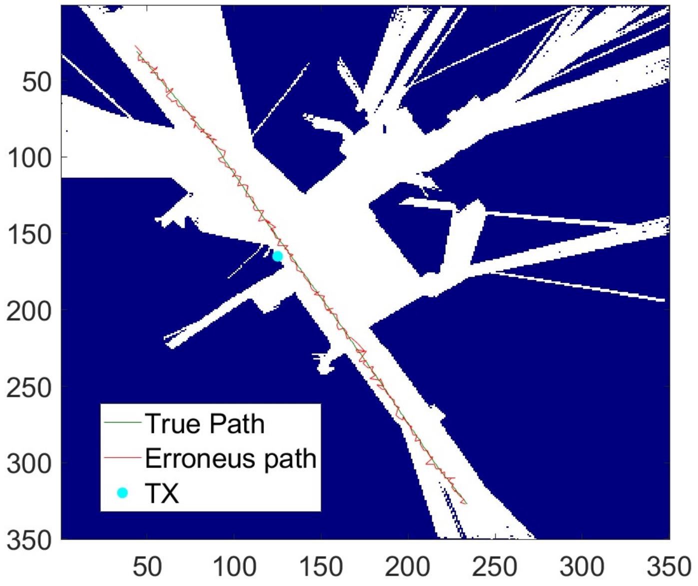

(B) Uncorrelated error model realization instance in the path.

FIGURE 4.29: Error model realization for mobility path 2 with Hong Kong error model in the semantic building map. White areas are those where data are available, dark blue areas are areas where data are not available, thus areas occupied by buildings or not reached by the TX signal.

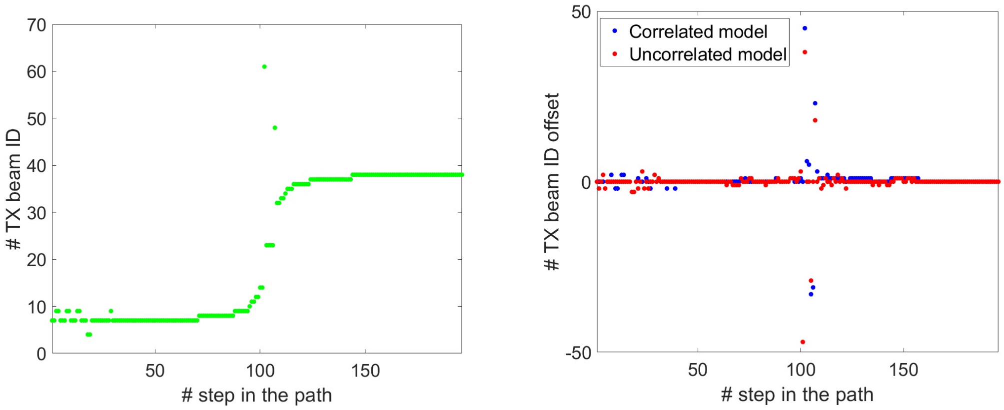

(A) TX best beam ID.

(B) TX beam ID offset.

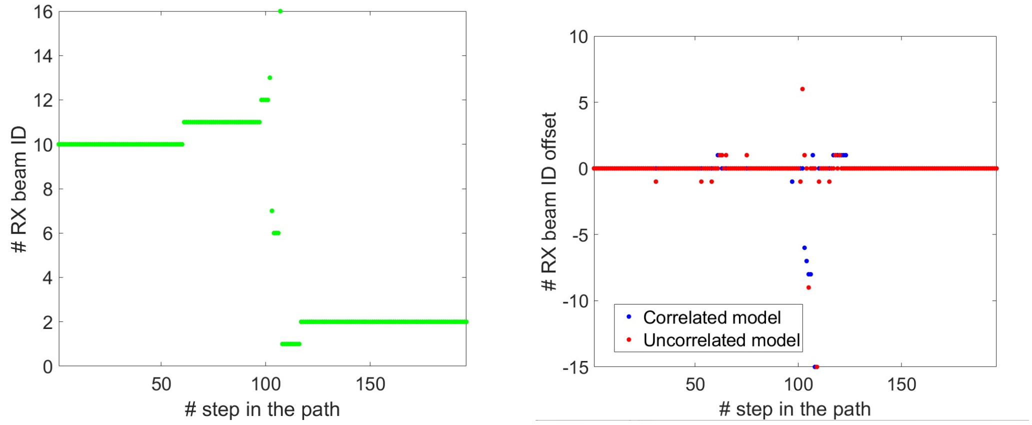

(C) RX best beam ID.

(D) RX beam ID offset.

FIGURE 4.30: The top and bottom graphs in the left column show the best TX and RX beam IDs along path 2, respectively. The top and bottom graphs in the left column show offsets against the best beam IDs of Hong Kong correlated and uncorrelated error model. Specifically, the upper right graph shows the offset for the TX beam ID and the lower right graph shows the offset of the RX beam ID.

realizations have positions that are at most 5m away from the corresponding correct position. Once again, the main difference between the correlated model in Fig.4.29a and the uncorrelated model in Fig.4.29b lies in the fact that the former crosses the green line very few times (only one this case), while the latter crosses it continuously by moving from one side to the other.

Fig.4.30 presents results regarding TX and RX beam IDs along the path for the same realization instances of the error models shown in Fig.4.29a and Fig.4.29b. Specifically, the best TX beam IDs along path 2 are shown in Fig.4.30a and reported again for the sake of completeness. Offsets of TX beam IDs selected by the correlated and uncorrelated error models with respect the best TX beam ID along the path are illustrated respectively in blue and red in Fig.4.30b. It can be seen that correlated and uncorrelated models have relevant TX ID offsets for the same positions as the Frankfurt model applied to the same path, as it can be realized by comparing Fig.4.30b with Fig.4.27b. These positions are the initial positions away from the TX but especially those very close to the TX. One difference from the Frankfurt model can be noted, however, concerning TX correlated offsets for positions close to the TX. In fact, the offsets for the Hong Kong correlated model are positive just after the TX is passed, while in the Frankfurt model they are mainly negative for the same positions. The offset of different sign can be explained by the fact that the realization of the correlated error model for Frankfurt shown in Fig.4.26a is closer to the TX than the corresponding correct positions for positions in front of the TX, while the one for Hong Kong shown in Fig.4.29a is located farther. The RX best beam IDs for the correct path are shown in Fig.4.30c. Correlated and uncorrelated RX beam ID offsets shown in Fig.4.30d presents similar characteristics than the ones for TX beam IDs. Relevant is that with the uncorrelated model offsets are found for positions between 50 and 65 where for the correlated model these are almost absent for the same positions.

The effect of the worsening performance given by Hong Kong correlated and uncorrelated GPS error models applied for path 2 are shown in Fig.4.31 in terms of bit-rate degradation. In particular, Fig.4.31a illustrate the bit-rate performance achieved by the correlated GPS error model, Fig.4.31b the same for the uncorrelated error model. In both the figures, the green line represents the bit-rate along the path in the error-free scenario, it is then the upper bound for the performance. The blue line indicates the average bit-rate along the path for 1000 realizations of the error model. The red line represents the bit-rate achieved by the specific realization displayed in Fig.4.29, and the gray lines indicate the bit-rate reached by other 150 error model realizations. It can be seen that correlated and uncorrelated error models achieve similar average bit-rate for initial positions between 0 and 40, in both scenarios in fact this is close to the optimum in this first part of the path. An average performance equal to the optimum is obtained with both models for positions between 40 and 80. The average bit-rate for uncorrelated error model in Frankfurt shown Fig.4.28b is significantly lower in these positions than the bit-rate achieved by the uncorrelated error model for Hong Kong displayed in Fig.4.31b. This happens simply because the average error generated by the Frankfurt model is higher than in Hong Kong. The correlated model gives a lower average bit-rate than the uncorrelated model for locations very close to the TX. The same is happening with the Frankfurt model, as it can be seen in Fig.4.28. Lastly, for the final positions between 125 and 196, the average bit-rate is almost always the same as the optimal bit-rate for both models.

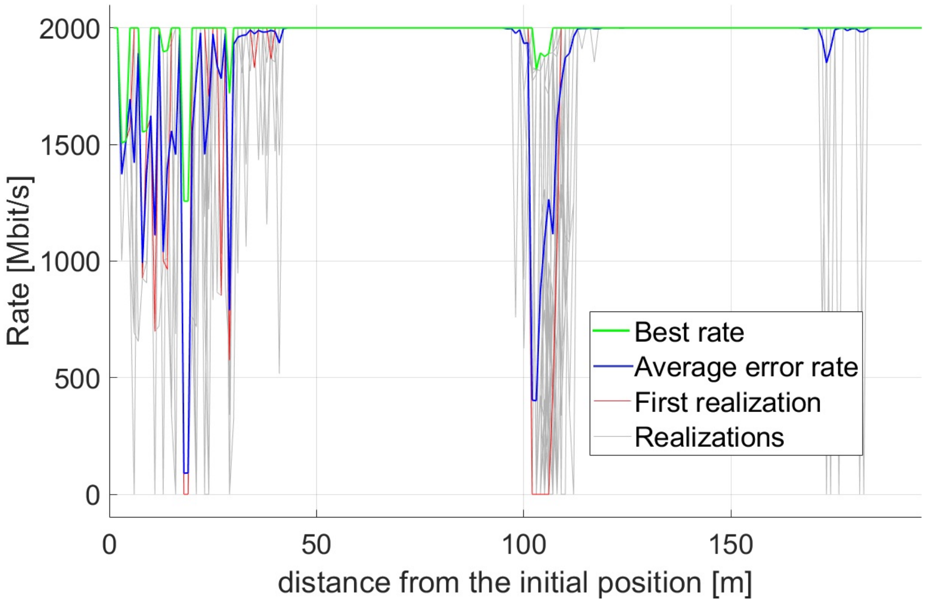

(A) Bit-rate degradation for correlated error model.

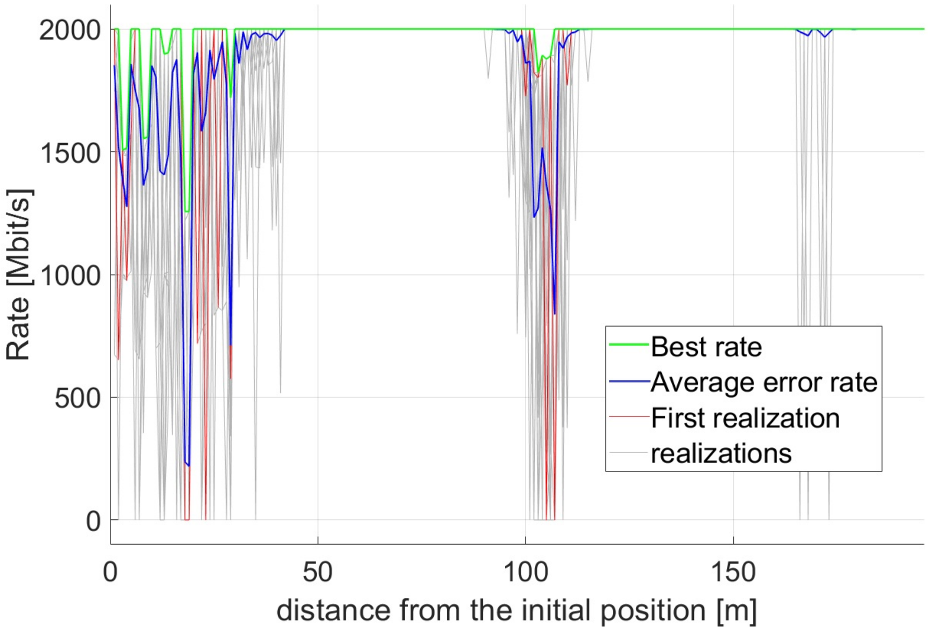

(B) Bit-rate degradation for uncorrelated error model.

FIGURE 4.31: Bit-rate degradation along the path 2 caused by Hong Kong error model. Green line represents the rate bit-rate in the error-free scenario, blue line indicates the average bit-rate over 1000 realizations of the error model applied in the path, red line represents the bit-rate achieved by the specific erroneous realization showed in Fig.4.29, and grey lines indicate the bit-rate reached by other 150 error model realizations.

4.1.2.3 Mobility path 3

The results for Ornstein-Uhlenbeck correlated error model applied to the third mobility path are now analyzed. As it can be seen from Fig.3.7, path 3 is always pretty close to the TX and it experiences a relevant channel variation due sudden change in path direction with a corresponding transition of the connection from LoS to NLoS. It also often walks very close to the buildings considered in the ray-tracing simulation. Moreover, path 3 is the shortest since it crosses 70 positions in the network grid. The latitude and longitude error model parameters selected are those respectively shown in Tab.3.4 and Tab.3.5. The analysis is performed for the 5-minutes walk and for the three different urban scenarios discussed in Sec. 3.2.3: San Francisco, Frankfurt, and Hong Kong. To single-out the effect of the correlation, an uncorrelated Gaussian process is also used for the same path as error model. To make a fair comparison, the variance of the error applied to the Gaussian process is the same as the realization of the Ornstein-Uhlenbeck correlated process. In this approach, the correlated and uncorrelated GPS error models have the same impact in terms of error.

San Francisco error model in path 3 Fig.4.32 shows one error model realization in path 3 for correlated error model in Fig.4.32a, and uncorrelated error model in Fig.4.32b using San Francisco GPS dataset for model tuning. In both the sub figures, the green line indicates the correct path, and the red line indicates the path made incorrect by the GPS error model. In addition, the position of the TX is indicated by the light blue dot. It can be seen from the 4.32a that the correlated model generates the largest errors at sudden changes in path direction. This can be noticed especially at the first left turn. Moreover, some last positions of the correlated error realization overlap with the blue data-free area. Due to the lack of correlation, the realization shown in Fig.4.32b is without a definite pattern.

Fig.4.33 presents results regarding the TX and RX beam IDs along the path for the same realization instances of the error models shown in Fig.4.32a and Fig.4.32b. Specifically, the best TX beam IDs for the correct path are shown in Fig.4.33a. In the same figure it can be seen that the best TX beam IDs assume almost constant offset values until position 30 and then changes discontinuously and remains almost constant again until the end, except for some isolated position in this last section served by a very different beam. The main discontinuity at position 30 occurs at the transition between LoS and NLoS conditions. Offsets of TX beam IDs selected by the correlated and uncorrelated error model with respect to the best beam IDs along the path are illustrated respectively in blue and red in Fig.4.33b. It can be seen that both the correlated and the uncorrelated models assume relevant TX offsets for some last positions in NLoS conditions. The uncorrelated model takes both positive and negative offsets in these last positions, while the correlated model only takes positive offsets. The best RX beam ID along the path shown in the Fig.4.33c has the same characteristics as the best TX beam ID in Fig.4.33a. In fact, it presents a discontinuity for the same position at the transition between LoS and NLoS conditions. The RX beam ID offsets are almost always equal to zero except for some isolated cases both for the correlated and uncorrelated error models.

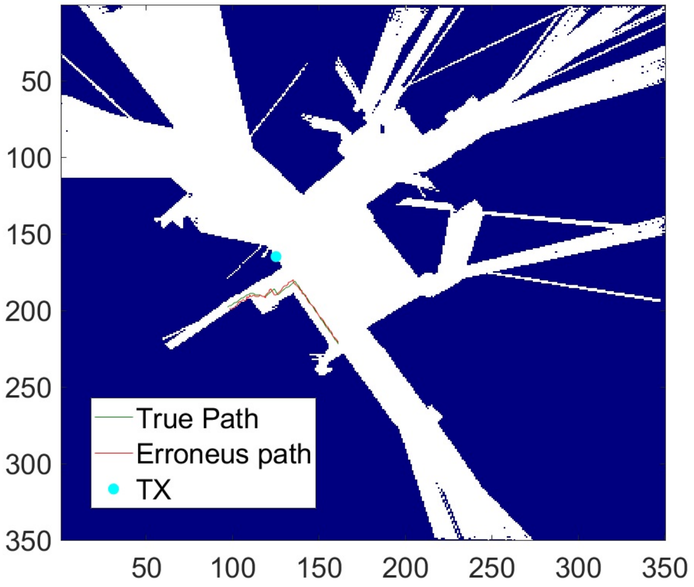

(A) Correlated error model realization instance in the path.

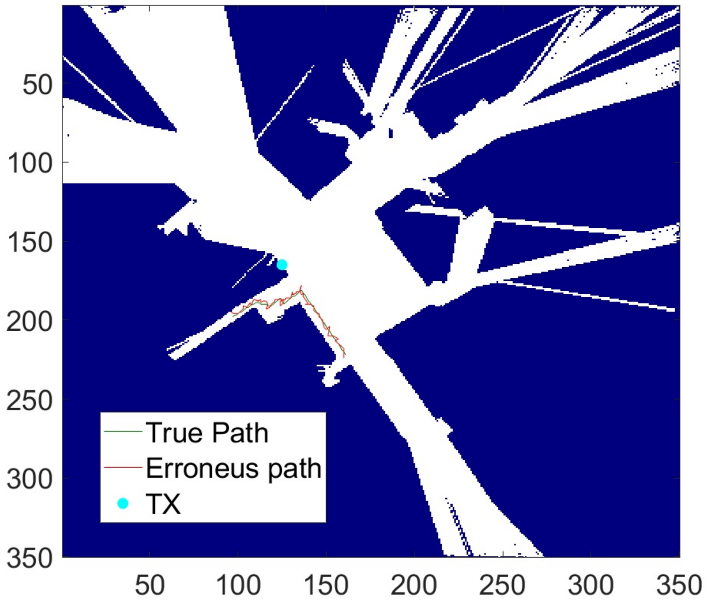

(B) Uncorrelated error model realization instance in the path.

FIGURE 4.32: Error model realization for mobility path 3 with San Francisco error model in the semantic building map. White areas are those where data are available, dark blue areas are areas where data are not available, thus areas occupied by buildings or not reached by the TX signal.

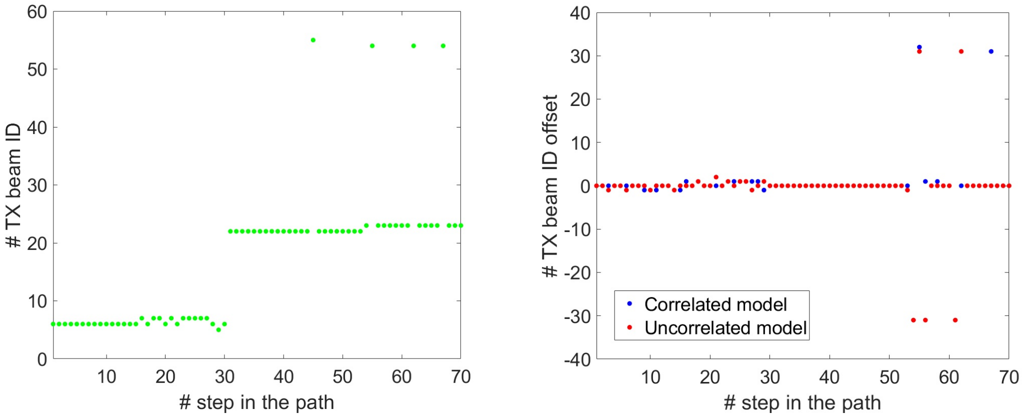

(A) TX best beam ID.

(B) TX beam ID offset.

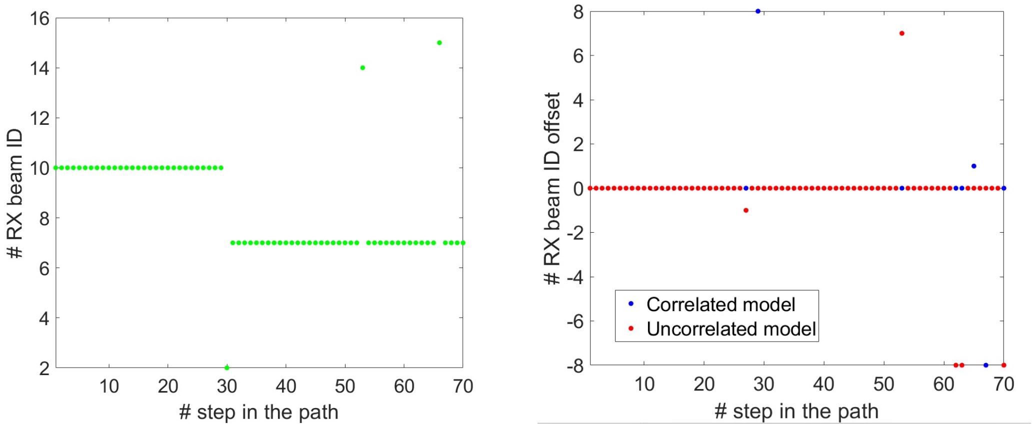

(C) RX best beam ID.

(D) RX beam ID offset.

FIGURE 4.33: The top and bottom graphs in the left column show the best TX and RX beam IDs along path 3, respectively. The top and bottom graphs in the left column show offsets against the best beam IDs of San Francisco correlated and uncorrelated error model. Specifically, the upper right graph shows the offset for the TX beam ID and the lower right graph shows the offset of the RX beam ID.

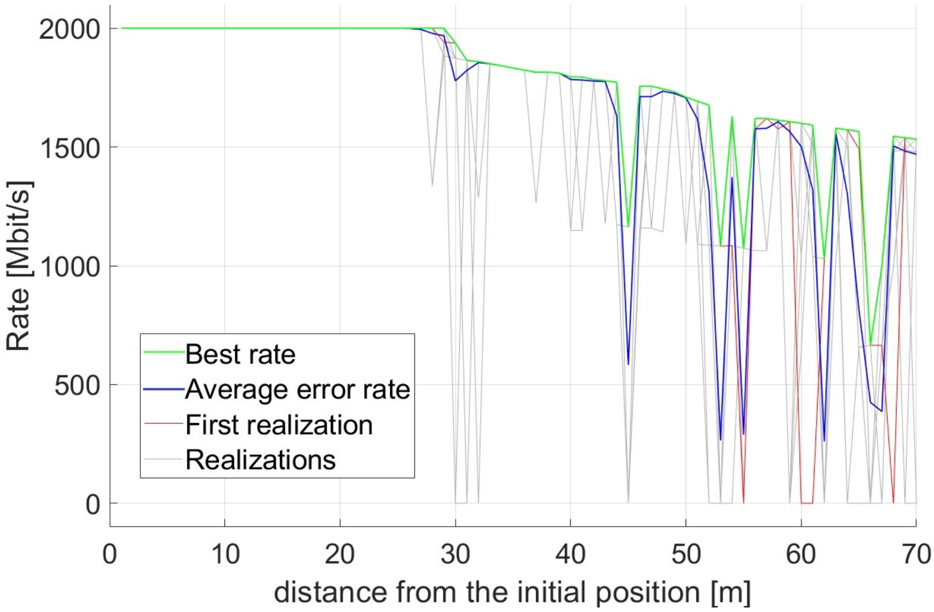

(A) Bit-rate degradation for correlated error model.

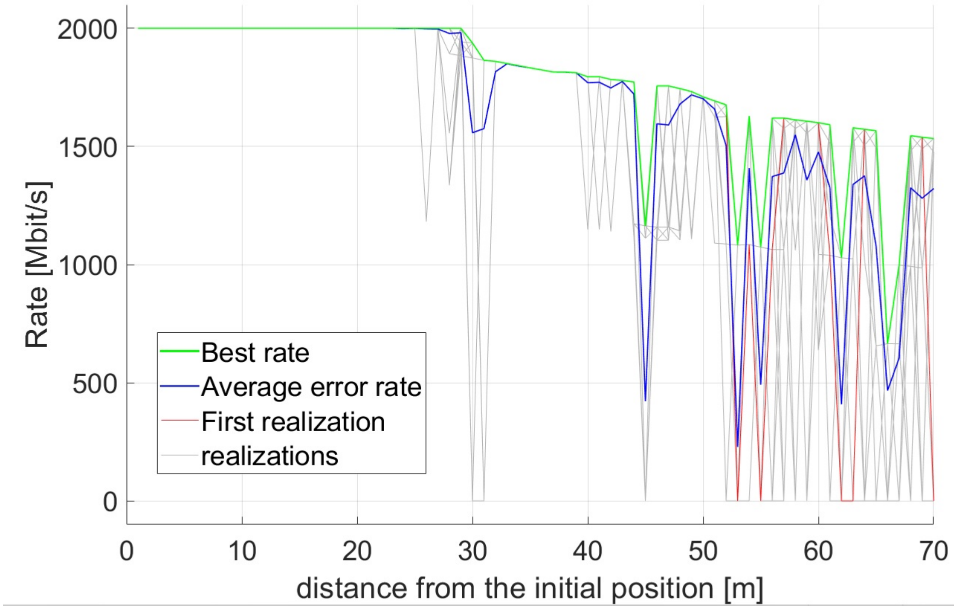

(B) Bit-rate degradation for uncorrelated error model.

FIGURE 4.34: Bit-rate degradation along the path 3 caused by San Francisco error model. Green line represents the rate bit-rate in the error-free scenario, blue line indicates the average bit-rate over 1000 realizations of the error model applied in the path, red line represents the bit-rate achieved by the specific erroneous realization showed in Fig.4.32, and grey lines indicate the bit-rate reached by other 150 error model realizations.

The effect of the worsening performance given by San Francisco correlated and uncorrelated GPS error models applied for path 3 are shown in Fig.4.34 in terms of bit-rate degradation. In particular, Fig.4.34a illustrates the bit-rate performance achieved by the correlated GPS error model, Fig.4.34b the same for the uncorrelated error model. In both the figures, the green line represents the bit-rate along the path in the error-free scenario, it is then the upper bound for the performance. The blue line indicates the average bit-rate along the path for 1000 realizations of the error model. The red line represents the bit-rate achieved by the specific realization displayed in Fig.4.32, and the gray lines indicate the bit-rate reached by other 150 error model realizations. In Fig.4.34a it can be seen that the optimal bit-rate performance is equal to the maximum achievable bit-rate of 2000Mbps up to the first left turn and correspondent transition to NLoS condition. After this event, the best bit-rate along the path gradually decreases as the UE moves away from the TX. The average bit-rate is equal to the best one achievable for the first 30 positions in LoS condition for both the models. In the following positions the correlated model gives on average worse results than the correlated model, this can be noted in particular between positions 46 and 52, and for positions between 56 and 64. This phenomenon is also confirmed by the numerous grey realizations with very low bit-rates for positions between 53 and 70 in Fig.4.34b.

Frankfurt error model in path 3 Fig.4.35 shows one error model realization in path 3 for correlated error model in Fig.4.35a, and uncorrelated error model in Fig.4.35b using Frankfurt GPS dataset for model tuning. In both the sub figures, the green line indicates the correct path, and the red line indicates the path made incorrect by the GPS error model. In addition, the position of the TX is indicated by the light blue dot. It can be seen from Fig.4.35a that the correlated error model deviates significantly from the correct path, even 15 meters far from the correspondent correct position. Moreover the correlated realization overlaps with no-data area from position 51 onward. Also the uncorrelated error realization shown in Fig.4.35 overlaps several times with the no-data area but in a more isolated and distributed manner along the way.

Fig.4.36 presents results regarding TX and RX beam IDs along the path for the same realization instances of the error models shown in Fig.4.35a and Fig.4.35b. Specifically, the best TX beam IDs along path 3 are shown in Fig.4.36a and reported again for the sake of completeness. Offsets of TX beam IDs selected by the correlated and uncorrelated error models with respect the best TX beam ID along the path are illustrated respectively in blue and red in Fig.4.36b. It can be seen from the same figure that the correlated model acquires positive TX offsets slightly different from 0 for positions that are close to the TX, while these are largely negative and almost constant for positions immediately preceding the first left turn. Subsequent to this first turning at the transition into the NLoS condition for position 30, the TX offset of the correlated model remains zero and then takes on values that are first broadly negative and then broadly positive. This large offset discontinuity for the correlated error model is rarer in the LoS condition. This happens because nearby positions in the NLoS condition can also be served by beams having very different IDs due to the complexity of the signal reflections reaching those areas. Lastly, from position 50 onward, the

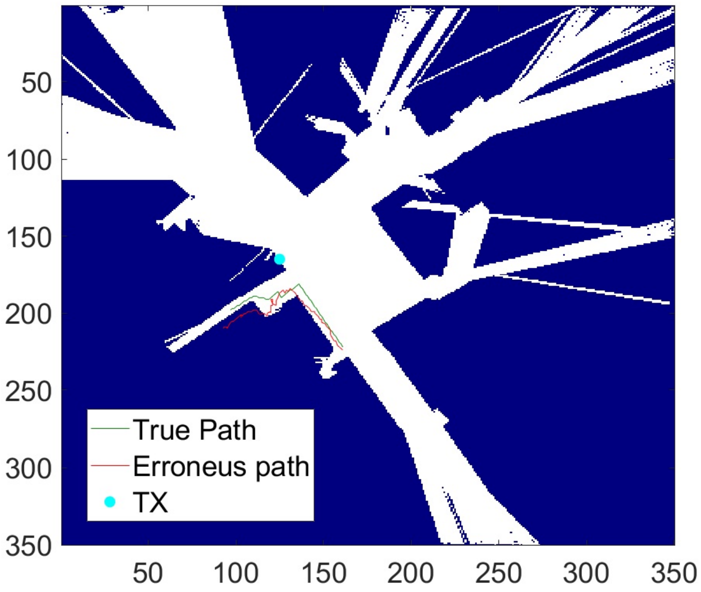

(A) Correlated error model realization instance in the path.

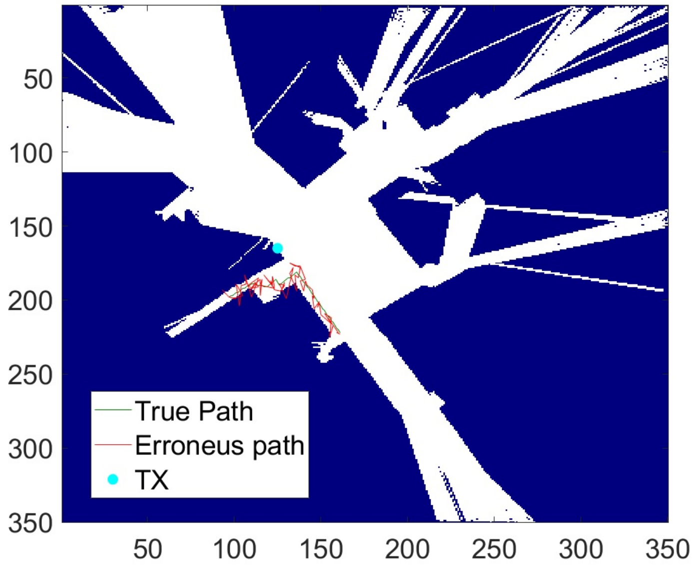

(B) Uncorrelated error model realization instance in the path.

FIGURE 4.35: Error model realization for mobility path 3 with Frankfurt error model in the semantic building map. White areas are those where data are available, dark blue areas are areas where data are not available, thus areas occupied by buildings or not reached by the TX signal.

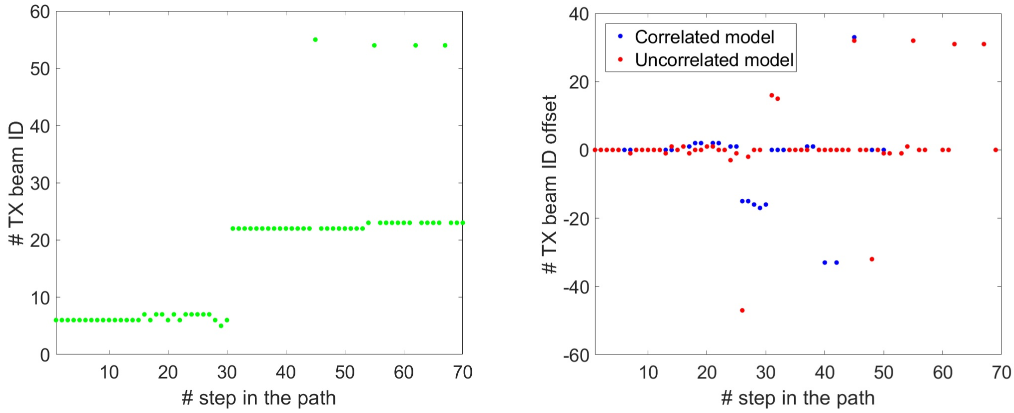

(A) TX best beam ID.

(B) TX beam ID offset.

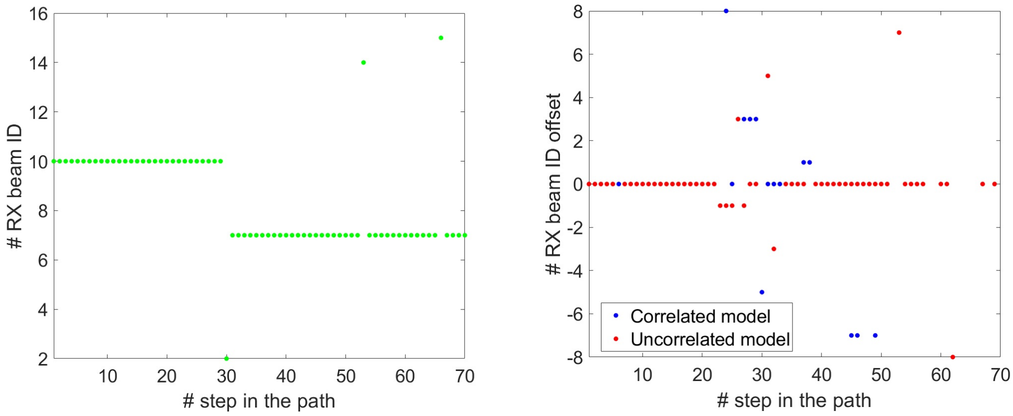

(C) RX best beam ID.

(D) RX beam ID offset.

FIGURE 4.36: The top and bottom graphs in the left column show the best TX and RX beam IDs along path 3, respectively. The top and bottom graphs in the left column show offsets against the best beam IDs of Frankfurt correlated and uncorrelated error model. Specifically, the upper right graph shows the offset for the TX beam ID and the lower right graph shows the offset of the RX beam ID.

correlated model offset could not be calculated because of the permanent overlap of the realization shown in Fig.4.35a with the region without data. The TX offset of the uncorrelated model shown in Fig.4.36b takes non-zero values from the transition to NLoS condition onward, to then take positive and negative values discontinuously. The RX best beam IDs for the correct path are shown in Fig.4.36c. Both the RX offset for the correlated and the uncorrelated model shown in Fig.4.36d start to acquire non-zero values as the UE approaches the TX around position 25 and above. In this case, both models from position 25 onwards take positive and negative offset values without a definite pattern.

The effect of worsening performance given by Frankfurt correlated and uncorrelated error models applied for path 3 are presented in Fig.4.37 in terms of bit-rate degradation. In particular, Fig.4.37a illustrates the bit-rate performance achieved by the correlated GPS error model, Fig.4.37b the same for the uncorrelated model. It can be seen by comparing the average error rates achieved by the two models, that the correlated model performs generally worse. This can be seen in particular between positions 0 and 40, and it is due to the fact that it is more likely for the correlated model to overlap for long stretches with the no-data zone given its proximity to it. On the other hand, the uncorrelated model may enter the no-data area but exit more rapidly. Between position 40 and 45 both models instead provide about the same average bit-rate. These are positions in NLoS condition but far from the data-free area. From position 45 onward the correlated model gives a significantly worse average bit-rate than the uncorrelated one. This is particularly visible from position 54 onward where the correlated model achieves an average bit-rate slightly above 0. The explanation is again related to the proximity to the no-free area, in fact as can be seen in Fig.4.35 the last section of the correct path passes extremely close to a building.

Hong Kong error model in path 3 Fig.4.38 shows one error model realization in path 3 for correlated error model in Fig.4.38a, and uncorrelated error model in Fig.4.38b using Hong Kong GPS dataset for model tuning. It can be seen that the correlated error model generates positions further away from the correct ones at sudden changes in path direction, particularly at the second and third changes in direction. In contrast, the uncorrelated model in Fig.4.38b is not affected by this occurrence.

Fig.4.39 presents results regarding TX and RX beam IDs along the path for the same realization instances of the error models shown in Fig.4.38a and Fig.4.38b. Specifically, the best TX beam IDs along path 3 are shown in Fig.4.39a and reported again for the sake of completeness. Offsets of TX beam IDs selected by the correlated and uncorrelated error models with respect the best TX beam ID along the path are illustrated respectively in blue and red in Fig.4.39b. It can be seen that the correlated model acquires slightly negative offsets between positions 9 and 22, these are positions immediately prior to the transition to the NLoS condition and increasingly close to the TX. For positions immediately following the transition to NLoS condition, the correlated model assumes zero offsets. Then it assumes first very negative offsets from position 47 and then some very positive offsets from position 62. The uncorrelated

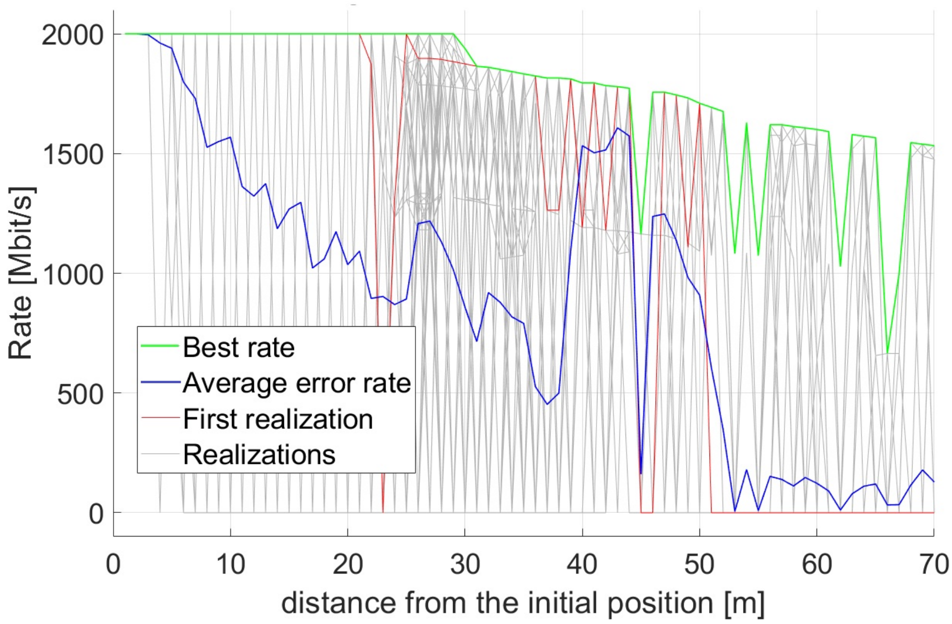

(A) Bit-rate degradation for correlated error model.

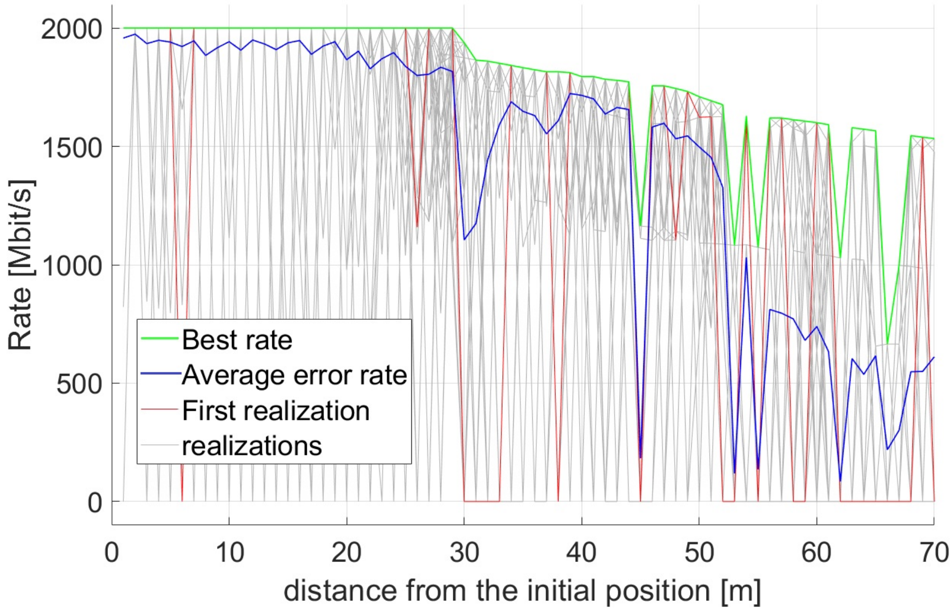

(B) Bit-rate degradation for uncorrelated error model.

FIGURE 4.37: Bit-rate degradation along the path 3 caused by Frankfurt error model. Green line represents the rate bit-rate in the error-free scenario, blue line indicates the average bit-rate over 1000 realizations of the error model applied in the path, red line represents the bit-rate achieved by the specific erroneous realization showed in Fig.4.35, and grey lines indicate the bit-rate reached by other 150 error model realizations.

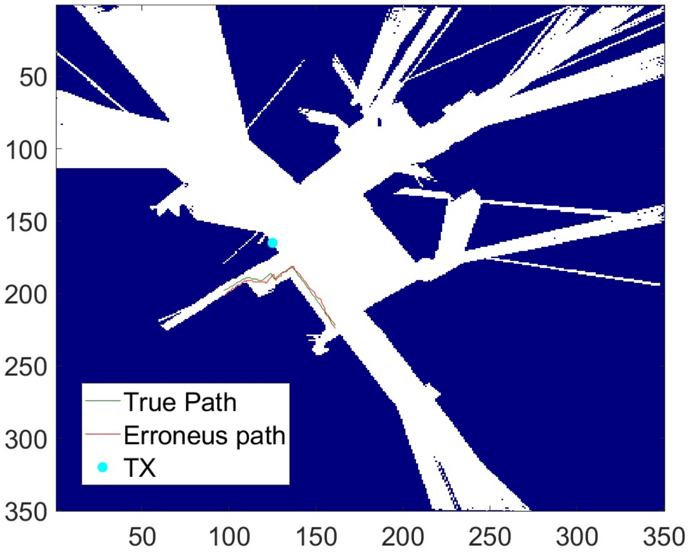

(A) Correlated error model realization instance in the path.

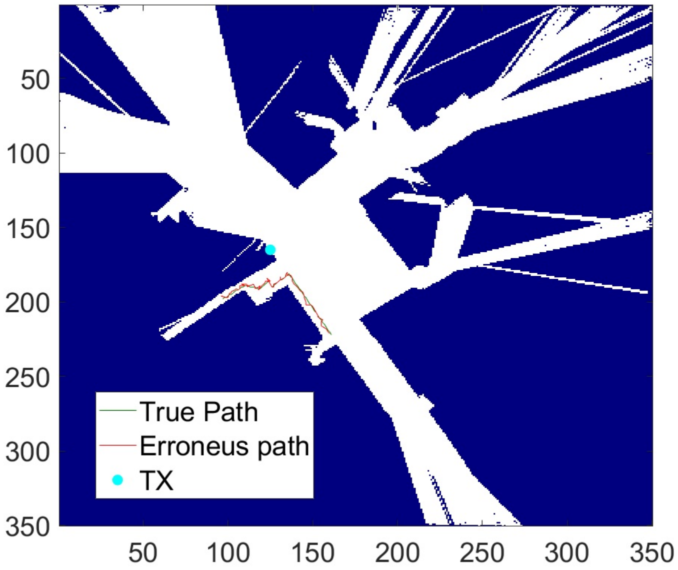

(B) Uncorrelated error model realization instance in the path.

FIGURE 4.38: Error model realization for mobility path 3 with Hong Kong error model in the semantic building map. White areas are those where data are available, dark blue areas are areas where data are not available, thus areas occupied by buildings or not reached by the TX signal.

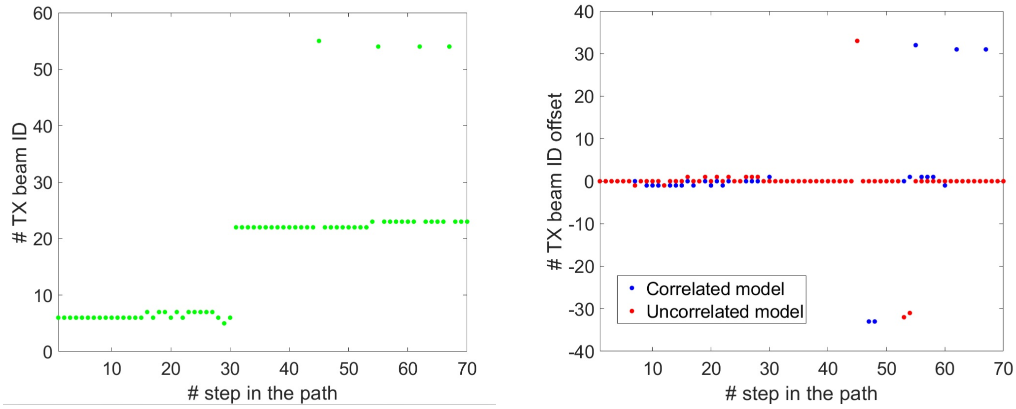

(A) TX best beam ID.

(B) TX beam ID offset.

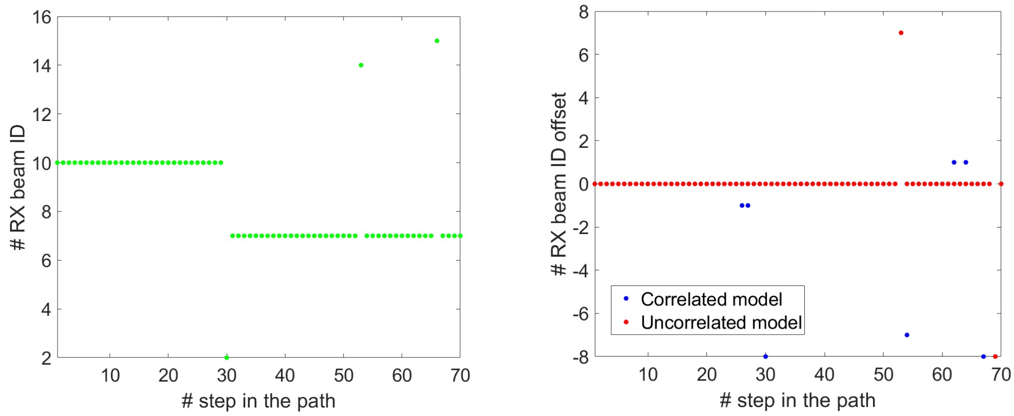

(C) RX best beam ID.

(D) RX beam ID offset.

FIGURE 4.39: The top and bottom graphs in the left column show the best TX and RX beam IDs along path 3, respectively. The top and bottom graphs in the left column show offsets against the best beam IDs of Hong Kong correlated and uncorrelated error model. Specifically, the upper right graph shows the offset for the TX beam ID and the lower right graph shows the offset of the RX beam ID.

model, on the other hand, takes some visibly different values from zero in the TX offset only from position 45 onward. The RX best beam IDs for the correct path are plotted in Fig.4.39c. In Fig.4.39d The RX offset for the uncorrelated model almost never takes values different from 0. The correlated model, on the other hand, takes negative offsets at the first left turn and then both negative and positive offsets at the last positions on the path.

The effect of worsening performance given by Hong Kong correlated and uncorrelated error models applied for path 3 are presented in Fig.4.40 in terms of bit-rate degradation. In particular, Fig.4.40a illustrates the bit-rate performance achieved by the correlated GPS error model, Fig.4.40b the same for uncorrelated model. It can be seen that both the models achieves average bit-rate equal to the best rate up to position 25. At position 30, the average bit-rate provided by the correlated model has a negative peak that touches very low bit-rate values; the peak almost not existing for the uncorrelated model. Around position 30 the first left turn of the path occurs and, as anticipated in the paragraph, the correlated error model has difficulty in tracking these sudden changes in direction. The negative peak presented by the correlated model at position 45 is also much more severe than the one achieved by the uncorrelated model for the same position. Lastly, the correlated model also achieves lower bitrates for the last positions of the path from 62 to the end. This is because of the proximity of those positions with a building and the aforementioned higher likelihood of the correlated model to have long stretches of realization overlapping with those areas.

Overall, the results of the chapter show that the effect of the GPS error model is strictly dependent on the urban density for which it was fitted. The GPS error model leased for the urban context of Frankfurt is the one that generated the most clear results regardless of the path considered. This is because the magnitude of the error in the Frankfurt scenario is enough to recognize an error pattern in the correlated model that distinguishes it from the uncorrelated. In the correlated case, it could be seen that the offset of beam IDs with respect to the best beam IDs for the correct path often have the same sign and are constant for entire portions of the path. This is especially true for the RX offset because the UE's antenna has only 16 beams instead of 64 to cover the circumstance space, so each beam covers a larger sector and is therefore more likely to remain constant for nearby positions. For the uncorrelated model, on the other hand, it is much more difficult to recognize patterns in the beam ID offset plots. Another noticeable result is also that the correlated model is more affected by the proximity of the path to areas of the map where data are not available. This is particularly apparent from the bit-rate degradation plots along the path, and is caused by the fact that it is more likely for the correlated model to have large portions of the realization overlapping with areas without data respect to the uncorrelated one. In practical situations, however, other operations such as extra beam sweeps can be performed to overcome this lack of data. This, however, requires extra resources in terms of energy and delay, so it is out the scope of this work.

The simulation also showed that there are parts of the network map that are more sensitive to error than others. This is the case for positions very close to the TX and it is because the sector covered by one beam ID is very narrow for these position, so

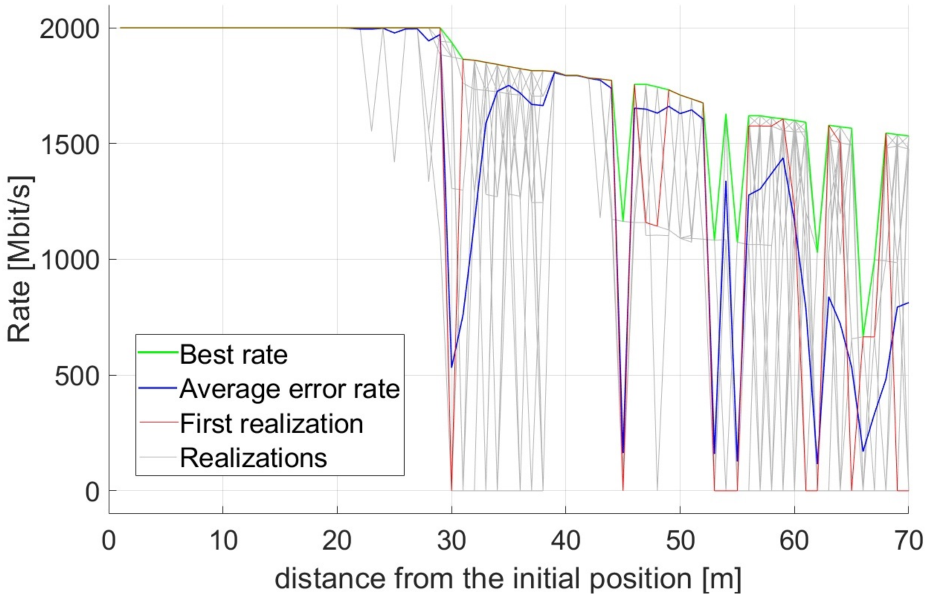

(A) Bit-rate degradation for correlated error model.

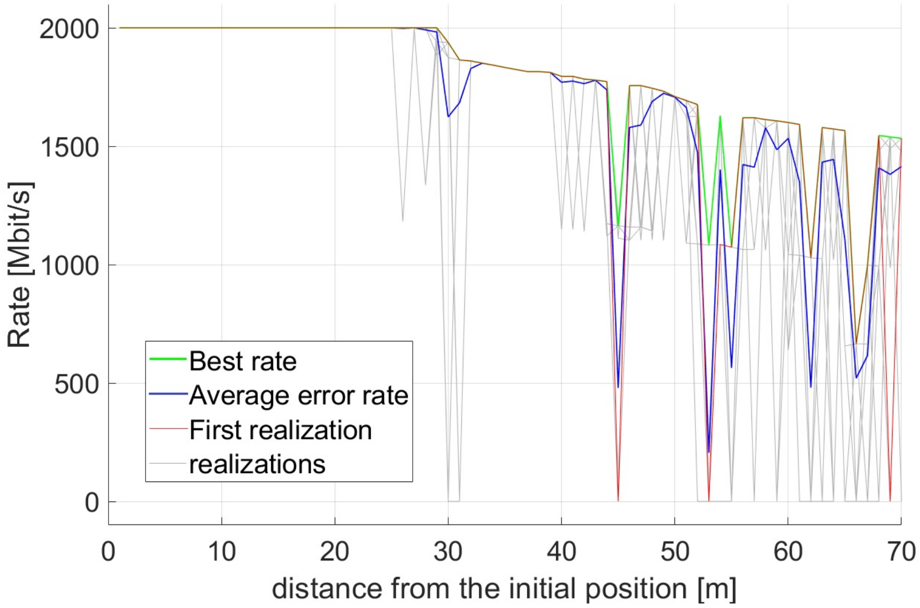

(B) Bit-rate degradation for uncorrelated error model.

FIGURE 4.40: Bit-rate degradation along the path 3 caused by Hong Kong error model. Green line represents the rate bit-rate in the error-free scenario, blue line indicates the average bit-rate over 1000 realizations of the error model applied in the path, red line represents the bit-rate achieved by the specific erroneous realization showed in Fig.4.38, and grey lines indicate the bit-rate reached by other 150 error model realizations.

even a slight inaccuracy about the location can be very damaging. In paths that pass close to the transmitter such as path 2 and path 3 even lighter error models such as the one for San Francisco and Hong Kong provide visible effects at those locations. Other positions in the network map that are particularly sensitive to error are those in the NLoS condition. That is because nearby positions in NLoS condition can also be served by beams having very different IDs due to the complexity of the signal reflections reaching those areas.

5

CONCLUSIONS AND FURTHER WORK

In this thesis, a simulation framework for location-aided beam management in 5G and beyond mm-wave networks was presented. Specifically, the location-related information leveraged in beam management procedures was the GPS positioning provided by the UE prior to data transmission. Furthermore, the degrading effect of GPS error in positioning was included in the simulation through realistic GPS error models. Two GPS error models were proposed: the first specific for the IA procedure in a static scenario, the second specific for the beam-tracking procedure in a dynamic scenario. The one related to the IA phase was referred as a static error model in the work, and it consists of providing an incorrect UE position to the serving BS according to a well-known statistical distribution. On the other hand, the one related to the beam-tracking procedure consisted of providing successive erroneous UE position information according to Ornstein-Uhlenbeck stochastic process, which was considered suitable for modeling GPS error correlation. Both error models were fitted according to datasets of GPS error measurements collected in three areas around the world having three different urban densities: San Francisco Bayshore Freeway, Frankfurt am Main, and Hong Kong city centre. Additionally, an open-source mm-wave ray-tracing tool was used to generate site-specific propagation data based on realistic 3D building footprints. The outcome of the ray-tracing simulation was used to build a REM in which the channel-related information per location is the BPL matrix.

The results for the static scenario showed that the GPS error in the information provided for the IA procedure has a non-negligible impact. A significant fraction of the attempts in the simulation ended in sub-optimal performances or BPL failure events due to erroneous information about the UE location. Even worse results have been found when the GPS error is realistically included in the construction of the REM and not only during the query of this. In both the settings, the largest component of BPL failure events were those due to unavailability of data at certain locations in the map. However, these specific events can be treated with dedicated procedures but leading to additional delays and increased use of network resources. These procedures can be further investigated in future works and may include selection of BPL based on the closest position having available data, or extra beam-sweep procedures.

The results for the dynamic scenario revealed that GPS error has a worsening impact strictly related to the urban characteristics and to the specific position in the network. In this regard, the error model for Frankfurt generated errors of significantly greater magnitude than that for Hong Kong despite the latter's greater overall urban density of the city. This happened because the GPS error measurements used to generate the Frankfurt model, were collected in narrow urban canyons that caused significant reflections and multipath phenomena of the GPS signal. This consideration emphasizes the importance of using error models specific for the neighborhood or street where the beam management operation is simulated. In addition, using a correlated error model is both realistic according to the literature and leads to different results than an uncorrelated error model with the same impact in terms of error magnitude. In fact, the correlated error model generally generated similar errors for successive UE positions in the network map. In future works, GPS error correlation could be exploited in combination with a partial beam sweep. If the RSS was to be below a certain threshold due to the error, a partial beam sweep could be performed to identify a better BPL. The BPL identified in this way could also be the first one tested at the next position given the error spatio-temporal correlation.

In conclusion, the thesis work outlined that the position-related information error needs to be included in the design of information-aided beam-management algorithms in mm-wave networks. However, the error model needs to be highly site-specific and suitable for modeling the particular nature of the error brought by the involved source of the information.

A

ABBREVIATIONS

SNR signal to noise ratio

5G 5th generation

mm-wave millimeter waves

TX transmitter

RX receiver

BPL beam-pair-link

IA initial access

MIMO multiple-input multiple-output

BS base station

UE user equipment

IoT internet of things

CSI channel state information

LoS line of sight

GPS Global Positioning System

LTE Long Term Evolution

RSS received signal strength

C plane control plane

REM radio environment map

NLoS non-line-of-sight

pdf probability density function

cdf cumulative distribution function

5G 5th generation

BIBLIOGRAPHY

[1] F. Al-Ogaili and R. M. Shubair, “Millimeter-wave mobile communications for 5g: Challenges and opportunities,” in *2016 IEEE International Symposium on Antennas and Propagation (APSURSI)*, 2016, pp. 1003–1004.

[2] Z. Zhang, Y. Xiao, Z. Ma, M. Xiao, Z. Ding, X. Lei, G. K. Karagiannidis, and P. Fan, “6g wireless networks: Vision, requirements, architecture, and key technologies,” *IEEE Vehicular Technology Magazine*, vol. 14, no. 3, pp. 28–41, 2019.

[3] M. Giordani, M. Polese, A. Roy, D. Castor, and M. Zorzi, “A tutorial on beam management for 3gpp nr at mmwave frequencies,” *IEEE Communications Surveys and Tutorials*, vol. 21, no. 1, pp. 173–196, 2019.

[4] A. M. Nor, S. Halunga, and O. Fratu, “Survey on positioning information assisted mmwave beamforming training,” *Ad Hoc Networks*, vol. 135, p. 102947, 2022.

[5] A. N. Uwaechia and N. M. Mahyuddin, “A comprehensive survey on millimeter wave communications for fifth-generation wireless networks: Feasibility and challenges,” *IEEE Access*, vol. 8, pp. 62 367–62 414, 2020.

[6] Z. Xiao, T. He, P. Xia, and X.-G. Xia, “Hierarchical codebook design for beamforming training in millimeter-wave communication,” *IEEE Transactions on Wireless Communications*, vol. 15, no. 5, pp. 3380–3392, 2016.

[7] D. E. Berraki, S. M. D. Armour, and A. R. Nix, “Application of compressive sensing in sparse spatial channel recovery for beamforming in mmwave outdoor systems,” in *2014 IEEE Wireless Communications and Networking Conference (WCNC)*, 2014, pp. 887–892.

[8] G. F. Edelmann and C. F. Gaumond, “Beamforming using compressive sensing,” *The Journal of the Acoustical Society of America*, vol. 130, no. 4, pp. EL232–EL237, 09 2011. [Online]. Available: https://doi.org/10.1121/1.3632046

[9] C. R. Berger, Z. Wang, J. Huang, and S. Zhou, “Application of compressive sensing to sparse channel estimation,” *IEEE Communications Magazine*, vol. 48, no. 11, pp. 164–174, 2010.

[10] H. Hassanieh, O. Abari, M. Rodriguez, M. Abdelghany, D. Katabi, and P. Indyk, “Fast millimeter wave beam alignment,” in *Proceedings of the 2018 Conference of the ACM Special Interest Group on Data Communication*, ser. SIGCOMM ’18. New York, NY, USA: Association for Computing Machinery, 2018, pp. 432–445. [Online]. Available: https://doi.org/10.1145/3230543.3230581

[11] A. Zhou, T. Wei, X. Zhang, and H. Ma, “Fastnd: Accelerating directional neighbor discovery for 60-ghz millimeter-wave wireless networks,” *IEEE/ACM Trans. Netw.*, vol. 26, no. 5, pp. 2282–2295, oct 2018. [Online]. Available: https://doi.org/10.1109/TNET.2018.2867044

[12] S. Sur, X. Zhang, P. Ramanathan, and R. Chandra, “Beamspy: Enabling robust 60 ghz links under blockage,” in *13th {USENIX} Symposium on Networked Systems Design and Implementation ({NSDI} 16)*, 2016, pp. 193–206.

[13] A. Ichkov, S. HÃ¤ger, P. MÃ¤hÃ¶nen, and L. Simić', “Comparative evaluation of millimeter-wave beamsteering algorithms using outdoor phased antenna array measurements,” in *2022 19th Annual IEEE International Conference on Sensing, Communication, and Networking (SECON)*, 2022, pp. 497–505.

[14] J. A. del Peral-Rosado, R. Raulefs, J. A. López-Salcedo, and G. Seco-Granados, “Survey of cellular mobile radio localization methods: From 1g to 5g,” *IEEE Communications Surveys & Tutorials*, vol. 20, no. 2, pp. 1124–1148, 2018.

[15] A. Capone, I. Filippini, and V. Sciancalepore, “Context information for fast cell discovery in mm-wave 5g networks,” in *Proceedings of European Wireless 2015; 21th European Wireless Conference*, 2015, pp. 1–6.

[16] J. Talvitie, T. Levanen, M. Koivisto, T. Ihalainen, K. Pajukoski, and M. Valkama, “Beamformed radio link capacity under positioning uncertainty,” *IEEE Transactions on Vehicular Technology*, vol. 69, no. 12, pp. 16 235–16 240, 2020.

[17] R. E. Rezagah, H. Shimodaira, G. K. Tran, K. Sakaguchi, and S. Nanba, “Cell discovery in 5g hetnets using location-based cell selection,” in *2015 IEEE Conference on Standards for Communications and Networking (CSCN)*, 2015, pp. 137–142.

[18] C. Laoudias, A. Moreira, S. Kim, S. Lee, L. Wirola, and C. Fischione, “A survey of enabling technologies for network localization, tracking, and navigation,” *IEEE Communications Surveys & Tutorials*, vol. 20, no. 4, pp. 3607–3644, 2018.

[19] F. LastName, F. LastName2, and F. LastName3, “Where acronyms such as DSL are properly escaped,” in *Proceedings of the 25th IEEE International Conference on Something (ICS)*, City, State, Country, March 2005, pp. 12–15.

[20] J. Morais, A. Behboodi, H. Pezeshki, and A. Alkhateeb, “Position aided beam prediction in the real world: How useful gps locations actually are?” 2022.

[21] Y. Zeng and X. Xu, “Toward environment-aware 6g communications via channel knowledge map,” *IEEE Wireless Communications*, vol. 28, no. 3, pp. 84–91, 2021.

[22] D. Wu, Y. Zeng, S. Jin, and R. Zhang, “Environment-aware hybrid beamforming by leveraging channel knowledge map,” 2022.

[23] A. Ichkov, P. MÃ¤hÃ¶nen, and L. Simić, “Is ray-tracing viable for millimeter-wave networking studies?” in *2020 IEEE 31st Annual International Symposium on Personal, Indoor and Mobile Radio Communications*, 2020, pp. 1–7.

[24] K. Merry and P. Bettinger, "Smartphone gps accuracy study in an urban environment," *PLOS ONE*, vol. 14, no. 7, pp. 1–19, 07 2019. [Online]. Available: https://doi.org/10.1371/journal.pone.0219890

[25] E. Noorani, Y. Savas, A. Koppel, J. Baras, U. Topcu, and B. M. Sadler, "Collaborative beamforming for agents with localization errors," in *2021 55th Asilomar Conference on Signals, Systems, and Computers*, 2021, pp. 204–208.

[26] A. W. Soundy, B. J. Panckhurst, and T. C. Molteno, "Enhanced noise models for gps positioning," in *2015 6th International Conference on Automation, Robotics and Applications (ICARA)*, 2015, pp. 28–33.

[27] R. P., T. W. Brunauer R., and R. S. Van der Spek S., "Why gps makes distances bigger than they are," *International Journal of Geographical Information Science*, 2016.

[28] W. Abbas and M. Zorzi, "Context information based initial cell search for millimeter wave 5g cellular networks," in *EUCNC 2016 - European Conference on Networks and Communications*. United States: Institute of Electrical and Electronics Engineers Inc., Sep. 2016, pp. 111–116, publisher Copyright: © 2016 IEEE.; 2016 European Conference on Networks and Communications, EUCNC 2016 ; Conference date: 27-06-2016 Through 30-06-2016.

[29] V. Va, T. Shimizu, G. Bansal, and R. W. Heath, "Beam design for beam switching based millimeter wave vehicle-to-infrastructure communications," in *2016 IEEE International Conference on Communications (ICC)*, 2016, pp. 1–6.

[30] A. Abdelreheem, E. M. Mohamed, and H. Esmaiel, "Location-based millimeter wave multi-level beamforming using compressive sensing," *IEEE Communications Letters*, vol. 22, no. 1, pp. 185–188, 2018.

[31] L. Simic, J. RiihijÃ¤rvi, A. Venkatesh, and P. Mahoonen, "Demo abstract: An open source toolchain for planning and visualizing highly directional mm-wave cellular networks in the 5g era," in *2017 IEEE Conference on Computer Communications Workshops (INFOCOM WKSHPS)*, 2017, pp. 966–967.

[32] A. F. MOLISCH and F. TUFVESSON, "Propagation channel models for next-generation wireless communications systems," *IEICE Transactions on Communications*, vol. E97.B, no. 10, pp. 2022–2034, 2014.

[33] M. Specht, "Consistency analysis of global positioning system position errors with typical statistical distributions," *The Journal of Navigation*, vol. 74, no. 6, pp. 1201–1218, 2021.

[34] I. Garmin International, "Gps 19x hvs technical specifications," *Garmin International, Inc.*, 2012.

[35] A. W. R. Soundy, B. J. Panckhurst, P. Brown, A. Martin, T. C. A. Molteno, and D. Schumayer, "Comparison of enhanced noise model performance based on analysis of civilian gps data," *Sensors*, vol. 20, no. 21, 2020. [Online]. Available: https://www.mdpi.com/1424-8220/20/21/6050

[36] H. Akaike, “A new look at the statistical model identification,” *IEEE Transactions on Automatic Control*, vol. 19, no. 6, pp. 716–723, 1974.

[37] S. Kuchuk-Iatsenko and Y. Mishura, “Option pricing in the model with stochastic volatility driven by ornstein-uhlenbeck process. simulation,” *Modern Stochastics: Theory and Applications*, vol. 2, no. 4, pp. 355–369, 2015.

[38] F. van Diggelen and M. Khider, “Android raw gnss measurement datasets for precise positioning,” in *Android Raw GNSS Measurement Datasets for Precise Positioning*, Virtual, 2020.

[39] P. Reisdorf, T. Pfeifer, J. Breßler, S. Bauer, P. Weissig, S. Lange, G. Wanielik, and P. Protzel, “The problem of comparable gnss results - an approach for a uniform dataset with low-cost and reference data,” in *The Fifth International Conference on Advances in Vehicular Systems, Technologies and Applications*, M. Ullmann and K. El-Khatib, Eds., vol. 5, nov 2016, p. 8, iSSN: 2327-2058.

[40] L.-T. Hsu, H.-F. N. Feng Huang, Y. Z. Guohao Zhang, X. Bai, and W. Wen, “Hong kong urbannav: An open-source multisensory dataset for benchmarking urban navigation algorithms,” *NAVIGATION: Journal of the Institute of Navigation*, vol. 70, no. 4, 2023. [Online]. Available: https://navi.ion.org/content/70/4/navi.602

[41] A. Ichkov, P. MÃ¤hÃ¶nen, and L. Simić, “Interference-aware user association and beam pair link allocation in mm-wave cellular networks,” in *2023 IEEE Wireless Communications and Networking Conference (WCNC)*, 2023, pp. 1–7.

Eidesstattliche Versicherung

Name, Vorname	Matrikelnummer (freiwillige Angabe)

Ich versichere hiermit an Eides Statt, dass ich die vorliegende Arbeit/Bachelorarbeit/ Masterarbeit* mit dem Titel

selbständig und ohne unzulässige fremde Hilfe erbracht habe. Ich habe keine anderen als die angegebenen Quellen und Hilfsmittel benutzt. Für den Fall, dass die Arbeit zusätzlich auf einem Datenträger eingereicht wird, erkläre ich, dass die schriftliche und die elektronische Form vollständig übereinstimmen. Die Arbeit hat in gleicher oder ähnlicher Form noch keiner Prüfungsbehörde vorgelegen.

Ort, Datum	Unterschrift

*Nichtzutreffendes bitte streichen

Belehrung:

§ 156 StGB: Falsche Versicherung an Eides Statt

Wer vor einer zur Abnahme einer Versicherung an Eides Statt zuständigen Behörde eine solche Versicherung falsch abgibt oder unter Berufung auf eine solche Versicherung falsch aussagt, wird mit Freiheitsstrafe bis zu drei Jahren oder mit Geldstrafe bestraft.

§ 161 StGB: Fahrlässiger Falscheid; fahrlässige falsche Versicherung an Eides Statt

(1) Wenn eine der in den §§ 154 bis 156 bezeichneten Handlungen aus Fahrlässigkeit begangen worden ist, so tritt Freiheitsstrafe bis zu einem Jahr oder Geldstrafe ein.

(2) Straflosigkeit tritt ein, wenn der Täter die falsche Angabe rechtzeitig berichtigt. Die Vorschriften des § 158 Abs. 2 und 3 gelten entsprechend.

Die vorstehende Belehrung habe ich zur Kenntnis genommen:

Ort, Datum	Unterschrift